

REPORT DOCUMENTATION PAGE				Form Approved OMB No. 0704-0188	
Public reporting burden for this collection of information is estimated to average 1 hour per response, including the time for reviewing instructions, searching existing data sources, gathering and maintaining the data needed, and completing and reviewing the collection of information. Send comments regarding this burden estimate or any other aspect of this collection of information, including suggestions for reducing the burden, to Department of Defense, Washington Headquarters Services, Directorate for Information Operations and Reports (0704-0188), 1215 Jefferson Davis Highway, Suite 1204, Arlington, VA 22202-4302. Respondents should be aware that notwithstanding any other provision of law, no person shall be subject to any penalty for failing to comply with a collection of information if it does not display a currently valid OMB control number. PLEASE DO NOT RETURN YOUR FORM TO THE ABOVE ADDRESS.					
1. REPORT DATE (DD-MM-YYYY) 08-07-2003		2. REPORT TYPE Final Report		3. DATES COVERED (From - To) 01-Apr-01 - 05-Aug-03	
4. TITLE AND SUBTITLE Investigating the effect of natural and technogenic atmospheric disturbances of the Northern hemisphere on the electromagnetic environment in the Antarctic			5a. CONTRACT NUMBER STCU Registration No: P-072 5b. GRANT NUMBER 5c. PROGRAM ELEMENT NUMBER 5d. PROJECT NUMBER 5d. TASK NUMBER 5e. WORK UNIT NUMBER 		
6. AUTHOR(S) Professor Yuri Yampolski			8. PERFORMING ORGANIZATION REPORT NUMBER N/A		
7. PERFORMING ORGANIZATION NAME(S) AND ADDRESS(ES) National Academy of Sciences of the Ukraine #4, Chervonopraporna St Kharkov 61002 Ukraine			10. SPONSOR/MONITOR'S ACRONYM(S) 11. SPONSOR/MONITOR'S REPORT NUMBER(S) STCU 01-8003		
9. SPONSORING/MONITORING AGENCY NAME(S) AND ADDRESS(ES) EOARD PSC 802 BOX 14 FPO 09499-0014			12. DISTRIBUTION/AVAILABILITY STATEMENT Approved for public release; distribution is unlimited.		
13. SUPPLEMENTARY NOTES			20040625 100		
14. ABSTRACT This report results from a contract tasking National Academy of Sciences of the Ukraine as follows: The Project is aimed at studying the effect of high-energy natural and/or technogenic processes in the Northern hemisphere in the electromagnetic conditions of the Antarctic region. The observations are to be held at the Ukrainian Antarctic base (UAB) 'Academician Vernadsky' at 65 S, 64 W. The Antarctic is known to be the only continent where industrial production is prohibited and sizable electric power sources and consumers are absent. As a result, the electromagnetic 'climate' in the region is controlled mostly by processes in the lithosphere, atmosphere and magnetosphere. Besides, the Antarctic region is characterized by little, if any thunderstorm activity, that being the principal source of radio interference at low and middle latitudes at frequencies of fractions of one hertz to tens of megahertz. Hence, the natural conditions in the region are favorable for investigating the electromagnetic processes occurring in different parts of the world, such as the global thunderstorm activity, large-scale geomagnetic disturbances, the low frequency radiation from the lithosphere on the earthquake eve, and so forth.					
15. SUBJECT TERMS EOARD, Physics, Electricity & Magnetism					
16. SECURITY CLASSIFICATION OF:			17. LIMITATION OF ABSTRACT UL	18. NUMBER OF PAGES 137	19a. NAME OF RESPONSIBLE PERSON Michael KJ Milligan, Lt Col, USAF
a. REPORT UNCLAS	b. ABSTRACT UNCLAS	c. THIS PAGE UNCLAS			19b. TELEPHONE NUMBER (include area code) +44 (0)20 7514 4260

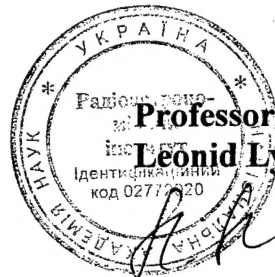
SCIENCE AND TECHNOLOGY CENTER IN UKRAINE

PARTNER PROJECT P-072

**INVESTIGATING THE EFFECT OF NATURAL AND
TECHNOGENIC ATMOSPHERIC DISTURBANCES OF THE
NORTHERN HEMISPHERE ON THE ELECTROMAGNETIC
ENVIRONMENT IN THE ANTARCTIC (P-072)**

Final Report

**Director,
Institute of Radio Astronomy,
National Academy of Sciences
of Ukraine**



**Professor
Leonid Lytvynenko**

Manager, Project P-072

A handwritten signature in black ink, likely belonging to Yuri Yampolski.

**Professor
Yuri Yampolski**

“ 14 ” July, 2003

Kharkiv-2003

TABLE OF CONTENTS

Page №

SECTION 1

INTRODUCTION	4
--------------------	---

SECTION 2

ELECTROMAGNETIC FIELD OBSERVATIONS IN ANTARCTICA	9
--------------------------------------------------------	---

2.1 Measurement of geomagnetic field variations	9
-------------------------------------------------------	---

2.1.1. <i>Instruments</i>	10
---------------------------------	----

2.1.2 <i>Data processing</i>	11
------------------------------------	----

2.1.3 <i>Statistics of geomagnetic pulsations</i>	13
---------------------------------------------------------	----

2.2 Observation of Schumann resonances and measurements at $f = 60$ Hz in Antarctica ...	13
------------------------------------------------------------------------------------------	----

2.2.1 <i>Data taking procedures and equipment</i>	13
---------------------------------------------------------	----

2.2.2 <i>ELF data processing in the range of Schumann resonances</i>	18
----------------------------------------------------------------------------	----

2.2.3 <i>Processing of the data collected at 60 Hz</i>	21
--------------------------------------------------------------	----

2.3 HF observations at Akademik Vernadsky in Antarctica and measurements in the course of the marine expedition	24
-----------------------------------------------------------------------------------------------------------------------	----

2.3.1 <i>HF research equipment</i>	24
------------------------------------------	----

2.3.2 <i>Methodology of measurements</i>	27
------------------------------------------------	----

2.4 HF heating experiment with a ELF modulation	29
-------------------------------------------------------	----

2.4.1 <i>HF detection</i>	29
---------------------------------	----

2.4.2 <i>Results and discussion: Special features</i>	30
-------------------------------------------------------------	----

SECTION 3

ULF / ELF WAVE PROPAGATION THROUGH THE ATMOSPHERE: THEORETICAL MODELS	37
-----------------------------------------------------------------------------	----

3.1 Magnetohydrodynamic (MHD) waves in the ionosphere	37
-------------------------------------------------------------	----

3.1.1 <i>Ultralow frequency (ULF) magnetic field variations</i>	37
-----------------------------------------------------------------------	----

3.1.2 <i>Nonlinear interaction of MHD waves with small-scale irregularities in the ionosphere</i>	41
---------------------------------------------------------------------------------------------------	----

3.2 Magnetic polarization of ELF fields in the gyrotropic Earth-ionosphere cavity	45
-----------------------------------------------------------------------------------------	----

3.2.1 <i>Gyrotropic model of electromagnetic wave propagation in the Schumann resonance range</i>	46
---------------------------------------------------------------------------------------------------------	----

3.2.2 <i>Polarization of Schumann resonances in the gyrotropic Earth-ionosphere cavity</i>	55
--------------------------------------------------------------------------------------------------	----

3.2.3 <i>Polarization structure of the fields at harmonic frequencies of power lines</i>	60
------------------------------------------------------------------------------------------------	----

3.3 A theory of geomagnetic effects of cyclone-produced AGWs	61
3.3.1 <i>Theoretical relations and numerical estimates</i>	62
3.3.2 <i>Generation mechanisms of the dynamo current. Ion drag and modulated conductivity..</i>	66
3.3.3 <i>AGW impact on ionospheric plasma parameters</i>	70
3.3.4 <i>Variations in ionospheric conductivity</i>	74
3.3.5 <i>Generation of magnetic disturbances.....</i>	75
3.3.6 <i>Transfer of disturbances to the conjugate region</i>	77

SECTION 4

RECOVERING THE CHARACTERISTICS OF FIELD SOURCES AND WAVE GUIDING STRUCTURES.....	80
4.1 Recovering the parameters of ULF micropulsations from polarization measurements ..	80
4.1.1 <i>Experimental data</i>	80
4.1.2 <i>Numerical analysis</i>	82
4.2 Recovering parameters of the world thunderstorm activity and of the Earth-ionosphere cavity from the data of ELF monitoring at the Antarctic station Akademik Vernadsky	86
4.3 Recovering sea wave parameters from the data of bistatic HF radio sounding	94
4.3.1 <i>Measured results</i>	94
4.3.2 <i>Theoretical formulation and solution pattern for the scattering problem.....</i>	96
4.3.3 <i>Interpretation of model results and comparison with experiment</i>	98
4.4 Magnetic effect of atmospheric weather disturbances in Antarctica.....	100
4.4.1 <i>Methodology of data processing</i>	101
4.4.2 <i>Results of data processing</i>	106
4.4.3 <i>Conjugate area effects of weather perturbations in Antarctica</i>	106
4.5 Is the spread F related to geomagnetic field disturbances?	109

SECTION 5

CONCLUSIONS.....	114
APPENDIX: Spectral and polarization parameters of the Schumann resonances.....	117
REFERENCES.....	135

INTRODUCTION

The present Report summarizes the results obtained during two years of execution of Project P-072. The Project was aimed at studying the electromagnetic environment of the Antarctic region in a broad range of frequencies between a few thousandths of one hertz and tens of megahertz. Along with the natural radiation sources contributing to the regional electromagnetic climate – such as geomagnetic field variations, global thunderstorm activity, cosmic background, etc., – an important role belongs to technogenic emissions, like signals of broadcasting or service radios in a variety of frequency ranges, radiation from electric power lines or powerful research transmitters, etc. The Project was focused on continuous monitoring of electromagnetic fields at the Ukrainian research station *Akademik Vernadsky* in Antarctica and development of techniques that would enable using these emissions for diagnostic purposes, i.e. for sensing remotely both sources of radiation and propagation media (atmosphere, ionosphere and magnetosphere, and the rough sea surface). For the most part, the results presented earlier in the Annual Progress Report (Year 1, 2002) are not included in this final document. Emphasis is rather made on the latest observational data and their interpretation in the framework of the original theoretical models suggested by the Project participants. A brief summary of the principal results (ranging in frequency from ULF to HF) is given in this Section below.

By June, 2003 the Project participants completed processing the data that were collected at ULF, ELF, VLF and HF during two winter campaigns at *Vernadsky* (2000 – 2001 and 2001 – 2002). At ULF, attention was centered at the quasiperiodic variations of the geomagnetic field related to resonance pulsations Pc3 and Pc4. Polarization properties of the pulsations have been analyzed for the almost conjugate sites in two hemispheres, namely *Akademik Vernadsky* in the South and the MIT Haystack Observatory in the North. Principal statistical regularities have been revealed in the orientation of the horizontal-plane magnetic polarization ellipse, resonance periods for different seasons of the year or times of the day, as well as in the appearance probabilities of the pulsations in dependence on the level of geomagnetic field disturbance. Two characteristic types of diurnal variations of the ellipse orientation have been identified for the first time and given the names of the ‘arch’ and ‘sunflower’ effects. They reflect resonant properties of the magnetospheric channel of wave propagation, behavior of transverse ionospheric conductivities and source location of the hydromagnetic waves in the magnetosphere. Analysis of the noise level throughout the ULF band (0.001 Hz to 1 Hz) that was performed with the super-sensitive magnetometers installed at *Vernadsky* has shown the major noise sources to be of natural rather

than technogenic origin. During the same period physical effects of longer duration were also studied, in particular the appearance of spread F in dependence on the level of disturbance in the geomagnetic field. This research stemmed from the hypothesis of the Project participants concerning the basic physics of the spread F phenomenon, namely that in some cases the effect might be due to a nonlinear exchange of energy between a varying magnetic field and ionospheric turbulence. The ionospheric data used for the analysis were 15-minute digital ionograms from the vertical ionosonde of *Vernadsky*, while the level of magnetic disturbance was characterized by sets of 3-hour K-indices, also obtained at the station. The result of a statistical treatment of these time series is the conditional appearance probability of spread F, calculated as a function of magnitude of the varying magnetic field. The input data for the calculations were two-year records of the two values. As follows from the analysis, a distinct dependence of the appearance probability of spread F upon the level of magnetic disturbance starts from the threshold value $K \geq 3$, which seems to validate the hypothesis of a nonlinear exchange. Further investigations should be aimed at identifying the specific mechanism of this nonlinear interaction, i.e. finding out how large-scale magnetic variations can pump energy into small plasma irregularities. One possible scenario has been analyzed theoretically. An Alfvén wave passing through a non-isothermal plasma of the F-layer is involved in a non-linear energy exchange with slow magnetosonic waves which can produce small scale fluctuations of electron density.

Another effect studied at ULF was the suspected coupling between the atmospheric gravity waves (AGW) excited by powerful atmospheric fronts over the Antarctic Peninsula and quasiperiodic variations of the geomagnetic field. A special algorithm, based on statistical and spectral analyses, was developed to search for a correlation of (AGW produced) atmospheric pressure variations near the surface and simultaneously occurring variations of magnetic field components. The statistical ensemble of data was represented by records of the values taken over the last seven years (5-minute samples of the field components and air pressure). Equal variation periods of the pressure and the magnetic field, of magnitudes characteristic of large-scale wave processes in the upper atmosphere (30 to 90 minutes), have been revealed for quiet magnetic conditions, $K < 4$. Normally, the AGW near the surface is in advance of the magnetic field variation. To interpret these effects, a theoretical model has been developed, permitting estimates of the level of modulation in the currents and conductivities as a result of upward AGW propagation. The behavior of geomagnetic field variations near the conjugate region of *Vernadsky* (Boston Area, Mass., USA) was analyzed for the periods when AGWs were excited in

Antarctica. A high level of correlation has been established between magnetic variations in the two regions during AGW generation by South - hemisphere cyclones.

At ELF, measurements of horizontal-plane magnetic components were organized over a very broad band (0.3 Hz to 300 Hz) for the first time in Antarctica. A preliminary analysis was performed of the fields radiated by lightning discharges of the global thunderstorm activity in 2002 and 2003, and of the technogenic radiation from continental power transmission lines of the Western hemisphere. Polarization analysis of the narrow band emission from power transmission lines (at 60 Hz) suggests that the major sources of radiation at this frequency are located on the North American continent (USA). As a result of spectral analysis application to year-long records of intensity variations of this emission, 12- and 24-hour and 7-day harmonics have been detected in the intensity, reflecting changes in the production and consumption of electric power (the latter periodicity is known as the weekend effect). Seasonal variations also have been revealed. The observations were interpreted within new theoretical models of ELF propagation through the Earth-ionosphere cavity. Improved solutions have been suggested for the direct and inverse problems, taking into account anisotropic effects in the plasma wall of the cavity. A numerical algorithm has been developed for calculating (magnetic) polarization characteristics of ELF signals of both kinds. The algorithm and its underlying theory permit using the data of spectral and polarization measurements in the Schumann range to resolve the three global centers of the thunderstorm activity in the angular domain and study each of them separately. The special quasi-optimal detection algorithm, developed for searching narrow band signals against the background of the natural ELF noise, has permitted observation of artificially excited oscillations in the cavity.

The HF activity was concentrated mainly on the analysis of the ionospheric effects detected with the aid of signals from Latin American broadcasting radios. Besides, special attention was given to trial reception sessions of dedicated signals from HF transmitters of the Russian Antarctic station *Bellingshausen* and Polish *Henryk Arctowski*. Both are separated from *Vernadsky* by shorter distances than 500 km, hence the HF signals propagate in a single-hop mode. This makes the two radio links optimal for recovery of wavelike disturbance parameters in the upper ionosphere. The trial measurements allowed recovering statistical and dynamic model parameters of traveling ionospheric disturbances (TIDs) through the use of the technology earlier developed by the Project participants within a different STCU Project (regular #827) and implemented at the MIT Haystack Observatory and the Center for Atmospheric Research of the University of

Massachusetts, Lowell. These measurements imply the necessity of organizing special purpose research radio links in Antarctica.

The HF program included analysis of spectral parameter variations of the radiation from the powerful heating facility of Tromsø, Norway. The experiment was devised with the special purpose of studying the possibility to detect in Antarctica the nonlinear effects stimulated by HF 'heating' of the Northern upper atmosphere. It was carried out within Project P-072 late in October, 2002. The reference radio link to compare manifestations of the expected effects was Tromsø to Kharkov, Ukraine (2400 km). By analyzing time coincident Doppler spectra from Antarctica and Ukraine it proved possible to reliably identify the situations when the HF signal propagating along the extremely long Tromsø – *Vernadsky* path did so owing to nonlinear excitation of an ionospheric duct. An alternative goal was to study the effects of 'transportation' of the HF power to Antarctica during periods when the solar terminator passed simultaneously over the transmit and receive ends of the link. With account of the fact that more than 6000 broadcasting radios are operative at HF, the majority of these being located in the Northern hemisphere, it is understood that terminator related effects may be responsible for canalized propagation of the HF power and for essential changes in the natural noise background in Antarctica.

Another part of the HF program concerned the bistatic 'radar' employing ionospherically reflected signals that are scattered by a rough sea surface. A multi-parametric theoretical model of this special case of Bragg scattering has been developed, which provides an adequate physical interpretation of the complex scattered spectra observed in experiment. The measurements were carried out in the Atlantic during the marine part of the 2001-2002 Antarctic mission. Comparison of the theory with the experiment has allowed suggesting a new remote sensing technique of recovering sea wave parameters.

The majority of observational data quoted in this Report (except earlier measurements) have been obtained by Project participants of whom three researchers (A. Koloskov, A. Zalizovski and P. Silin) made a year-long wintering campaign 2002-2003 at *Akademik Vernadsky* and other four (Y. Yampolski, S. Kascheev, I. Pikulik and V. Galushko) took part in seasonal works and marine expeditions to Antarctica in 2001, 2002 and 2003. In the course of Project execution exchange of meteorological and magnetic data was started with the US observatories lying close to the conjugate region of *Vernadsky*. Joint US – Ukrainian programs have been coordinated by Dr. Keith M. Groves of AF Research Laboratory. The scientific results of the Project's Year1 were presented and discussed at special workshops in AFRL, the MIT Haystack Observatory and

the University of Massachusetts, Lowell when Dr. Y. Yampolski stayed in the USA in March/April, 2002 as a Window-on-Science visitor. Totally, the Project results have been summarized in five papers (published or submitted to journals) and four conference presentations. Another three papers are being prepared for publication. The Project-related activity has allowed establishing fruitful contacts with the US colleagues involved in electromagnetic research in Antarctica (Prof. Umran S. Inan of Stanford University, Calif.; Prof. Mark J. Engebretson of Augsburg College, Minn.; Dr. Vladimir Papitashvili of NSF; Prof. Mark B. Moldwin and Dr. Eftyhia Zesta of UCLA, Calif.), and initiating new collaborative programs.

2 ELECTROMAGNETIC FIELD OBSERVATIONS IN ANTARCTICA

2.1 Measurement of geomagnetic field variations

Akademik Vernadsky is the place of location of the geomagnetic observatory AIA (Argentinean Islands Archipelago) that has been in continuous operation since late 1950s. The observatory occupies two buildings of which one is a non-magnetic structure accommodating all the field measuring instruments (sensors), while the other is used for auxiliary purposes, in particular for data recording. Note two novel elements in the operation of the observatory through 2002. First, K indices were estimated after two independent methods in parallel. Method 1, the standard technique of AIA, is based on the use of magnetic records from the La Cour magnetometer with a plotting board. Method 2 that was introduced in 2002 uses of digitized data from the LEMI-008 magnetometer, converted to the INTERMAGNET format. Automated estimations have been done in Method 2 using the standard software of the BEL Observatory (Belsk, Poland) [Jankowski and Sucksdorf, 1996].

The other novelty was the introduction of a new technique of absolute measurements, namely that of remainder compensation (Technique B). Until 2002, absolute measurements were performed in a technique that consisted essentially of determining angular characteristics of the fields from zero readings of a single-component sensor in a theodolite (technique A). When using the remainder compensation technique, the theodolite is set to certain fixed positions close to the "zero points" and remanent field values are read from the single-component sensor. This technique has two advantages of conceptual importance. First, the operator is at a considerable distance from the sensor, hence does not introduce errors to the readings associated with his own field. Second, all the measurements allow a precise fixation in time, such that the measured values can be recalculated for a specified time moment without resorting to averaging over the total time of absolute measurements. As a result, the measurements are possible, without loss of accuracy, with arbitrarily high disturbances in the magnetic field.

In March through December, 2002 absolute measurements were performed, on the average, once per three days, each time with the use of both techniques. First the newly introduced method (technique B) was used and then, directly after completion, the measurements were repeated in technique A. The comparative statistical analysis gave strong evidence in favor of the new technique.

2.1.1 Instruments

Throughout 2002, magnetic field variations were monitored with three variometers. The first of these, a La Cour magnetometer [Parkinson, 1983] recorded data on photographic paper. Two fluxgate magnetometers used digital recording. The E.D.A. magnetometer was equipped with a *Geologger* registration system, and the LEMI-008 stored data in its internal memory. The latter instrument is of Ukrainian make, it was designed and manufactured by the Lviv Center of the Space Research Institute, National Academy of Sciences – National Space Agency of Ukraine. The operation principle of the La Cour magnetometer is different from that of fluxgate, which is good in the respect that the ‘high frequency’ interference typical of the fluxgate instruments is not active here.

The LaCour variometer

This is the oldest instrument of the Observatory. Instruments of this kind were the standard equipment of world magnetic observatories in 1950s through early 1970s. The D-variometer is simply a bar magnet suspended on a thin quart filament and rotatable in the horizontal plane. The horizontal variometer is of a similar design, with the exception of the filament which should possess a high elasticity coefficient. The filament is twisted in its upper part in such a way that the magnetization axis of the bar should be perpendicular to the geomagnetic meridian. The Z-magnetometer involves a magnet with a horizontally-oriented axis, while the instrument itself is rotatable around the other horizontal-plane axis [Parkinson, 1983]. The magnetic field variations are registered with an optical system involving mirrors fixed to the magnets, and a set of prisms and lenses to focus the light beam to photographic paper. The instrument was used to estimate three-hour K-indices of magnetic disturbances. While the K-indices were also derived from the LEMI-008 data, the magnitudes calculated after the La Cour measurements remained the basic set through 2002.

The E. D.A. magnetometer and ‘Geologger’ registration system

The instrument is characterized by a resolution about 0.5nT and sampling rate of 20s. The data are used for the analysis of slow magnetic field variations in the problem of troposphere – ionosphere coupling (upward energy transfer via atmospheric gravity waves).

The LEMI-008 magnetometer

For the moment, the LEMI-008 is the most modern and most sensitive (resolution of 0.1 nT) magnetic instrument of the observatory. The sampling rate is 1s. Time-averaged data converted to the INTERMAGNET format are transmitted, via a satellite link, to the data collecting center in Ottawa, Canada, where they are made accessible in the Web in real time. To convert the

LEMI-008 output data to the 1-min INTERMAGNET format, a special program was composed using the Matlab tool (mag-intr. m). Standard software is used to derive 3-hour K-indices of magnetic disturbance from the LEMI data.

Unfortunately, two drawbacks of the instrument have to be mentioned, at least the way they were manifested in 2002. First, writing the data to the internal memory used to be interrupted for the periods of sampling and time correction. This resulted in 'legitimate' losses of data amounting to about one hour per week. The other drawback is the periodic spurious burst in all the components of the measured field, occurring every minute. A burst lasts for 5 to 9 second and can reach as high magnitudes as 1nT. This interference is extremely inconvenient for the analysis of fast magnetic variations, while it has practically no effect on the time-averaged data (one-minute INTERMAGNET format). The data from the LEMI-008 are used in the analysis of ULF variations of the geomagnetic field.

2.1.2 Data processing

The geomagnetic data of 2002 were processed to detect resonance pulsations and estimate their parameters. The LEMI-008 data were used, which represented variations of three geomagnetic field components, i.e. δH_H , δH_D and δH_Z (the frame of reference was selected so as to have the H -axis pointing Northwards along the magnetic meridian; the D -axis was oriented to the East, and the Z -axis vertically down. The data sampling period Δt was 1s).

In 2002, the data processing procedure featured a preparatory stage that permitted suppressing the one-minute interference. To that end, a special compensating algorithm was developed which actually reduced to estimating average parameters of the interference over time intervals about one hour. Then a 'pure' imitation burst was formed and subtracted from the output records.

Sequences of 500s-long records were analyzed, in which two horizontal field components only were of interest (the Z -component showed virtually no pulsation-related variations). Each of the two components was Fourier transformed:

$$S_{H, D, Z}^i(f) = \sum_{k=1}^N \delta H_{H, D, Z}^i(t_k) \exp(-i2\pi f t_k) \Delta t. \quad (2.1.1)$$

After that, narrow-band filtering was made in all the measuring channels. The presence of narrow-band components in the amplitude spectra, $\text{mod}\{S_H^i(f), S_D^i(f), S_Z^i(f)\}$, was evidence for the existence of micropulsations during the time interval i . As a result of the filtering, the frequency F and amplitudes H_{Hm}^i and H_{Dm}^i of the major energy carrying spectral components

were determined. Next, the phase difference between spatial components of the pulsations was estimated as the difference ψ_{HDi}^i in the harmonic of frequency F .

The spectral amplitudes, H_{Hm}^i and H_{Dm}^i , and phase differences ψ_{HDi}^i were used to evaluate parameters of the horizontal plane polarization ellipse. First, the absolute value H_{hm}^i of the horizontal-plane magnetic vector projection was estimated as a function of time at the surface level,

$$H_{hm}^i(t) = \sqrt{H_{Hm}^{i2} \cos^2(2\pi Ft) + H_{Dm}^{i2} \cos^2(2\pi Ft - \psi_{HDm}^i)}, \quad (2.1.2)$$

Then the maximum of $H_{hm}^i(t)$ was found, which occurred at time moment t_m ,

$$t_m = \frac{1}{4\pi F} \arctan \left(\frac{\sin(2\psi_{HDm}^i)}{\frac{H_{Hm}^{i2}}{H_{Dm}^{i2}} + \cos(2\psi_{HDm}^i)} \right), \quad (2.1.3)$$

At this point it was possible to calculate the axis lengths A_i and B_i of the polarization ellipse,

$$A_i = \sqrt{H_{Hm}^{i2} \cos^2(2\pi Ft_m) + H_{Dm}^{i2} \cos^2(2\pi Ft_m - \psi_{HDm}^i)}, \quad (2.1.4)$$

$$B_i = \sqrt{H_{Hm}^{i2} \cos^2(2\pi Ft_m + \pi/2) + H_{Dm}^{i2} \cos^2(2\pi Ft_m - \psi_{HDm}^i + \pi/2)}. \quad (2.1.5)$$

and the orientation angle φ_i of the major axis with respect to the Northward direction,

$$\varphi_i = \begin{cases} \arctan \left(\frac{H_{Dm}^i \cos(2\pi Ft_m - \psi_{HDm}^i)}{H_{Hm}^i \cos(2\pi Ft_m)} \right) & \text{with } A_i > B_i \\ \arctan \left(\frac{H_{Dm}^i \cos(2\pi Ft_m - \psi_{HDm}^i + \pi/2)}{H_{Hm}^i \cos(2\pi Ft_m + \pi/2)} \right) & \text{with } A_i < B_i \end{cases} \quad (2.1.6)$$

The ellipticity coefficient was evaluated as the minor-to-major axis ratio, or

$$K_i = \begin{cases} -\text{sign}(\psi_{HDm}^i) \left(\frac{B_i}{A_i} \right) & \text{with } A_i > B_i, \\ -\text{sign}(\psi_{HDm}^i) \left(\frac{A_i}{B_i} \right) & \text{with } A_i < B_i \end{cases} \quad (2.1.7).$$

Note the coefficient to be a sign dependent magnitude which is positive if the field vector rotates in the counterclockwise direction and negative in the opposite case. Below, we will dwell on the analysis of diurnal and seasonal variations of the polarization parameters φ_i and K_i .

2.1.3 Statistics of geomagnetic pulsations

The data collected over 2002 were subjected to polarization processing (see Subsection 2.1.2) and the results were analyzed for statistical characteristics over time intervals of a month's duration. The data averaged over such periods permit following variations in the polarization parameters occurring through the year. Consider the run of the ellipse orientation angle that was observed in 2002. The day-time variations in June (Fig. 2.1.1 e) and close to the winter solstice (Fig. 2.1.1 d-f) show a nearly linear run. As will be shown below (Sections 3.1 and 4.1), this behavior of the orientation angle is conditioned by the motion of the effective source of hydromagnetic disturbances along the celestial sphere. It is characteristic of low transverse conductivities of the ionospheric plasma and low Q-factors of the magnetospheric (field-line) resonant cavity. Contrary to that, the 'arch-like' variation, rather typical of December (Fig. 2.1.2 b) and the summer solstice period (Fig. 2.1.2 a-c), is associated with reasonably high magnitudes of integrated Pedersen and Hall conductivities and sufficient magnitude of the resonator's Q-factor.

2.2 Observation of Schumann resonances and measurements at $f = 60$ Hz in Antarctica

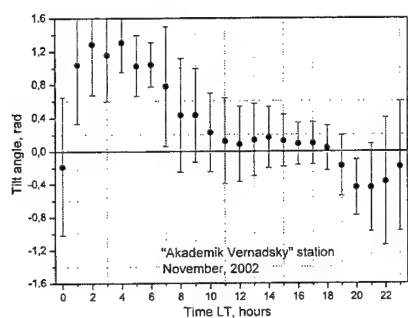
ELF noise observations have been carried on at *Akademik Vernadsky* since 2001. The aim of these experiments is twofold. First, it is to monitor the world thunderstorm activity through studying parameters of the Schumann resonances, which are excited in the Earth-ionosphere cavity by globally distributed lightning discharges. Second, to study the transfer to Antarctica of the electromagnetic energy radiated by electric power systems of industrially developed areas. To that end, a frequency band is monitored in the vicinity of the 60 Hz power line harmonic.

2.2.1 Data taking procedures and equipment

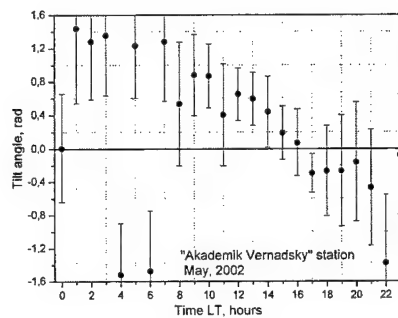
The ELF signals were recorded with the aid of a broad-band magnetometric complex which incorporated two identical induction type magnetic sensors and a computer based registration unit. The sensors permit measuring geomagnetic field variations through the range of 0.03 Hz to 300 Hz. Timing is provided by a GPS receiver. The ELF signals are converted to a digital format in an internal ADC of the computer. The technical specifications of the system are listed in Table 2.2.1.

Summer solstice (November-January)

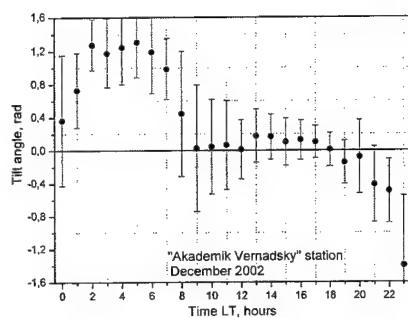
Winter solstice (May-July)



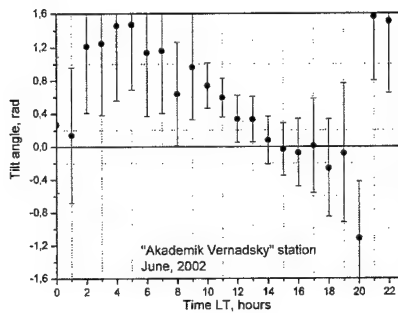
a



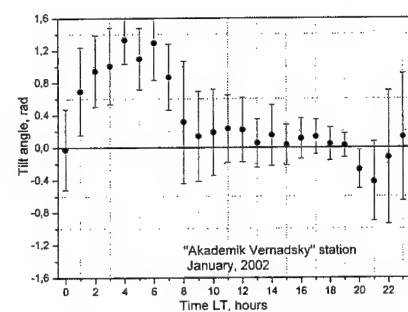
d



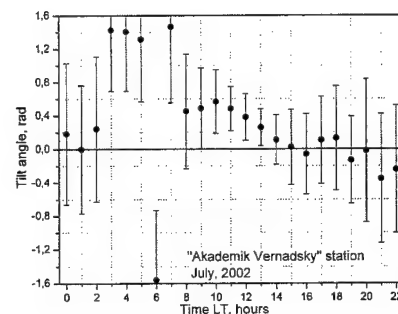
b



e



c



f

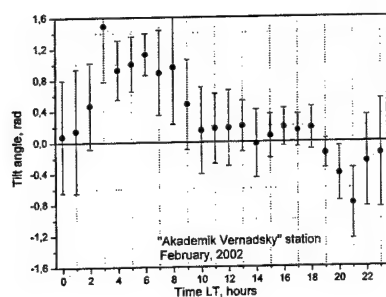
Fig. 2.1.1 Variations in the polarization ellipse orientation through 2002

a-c about the summer solstice (November – January);

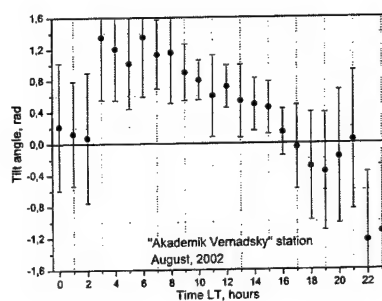
d-f: about the winter solstice (May - July);

Autumn equinox (February-April)

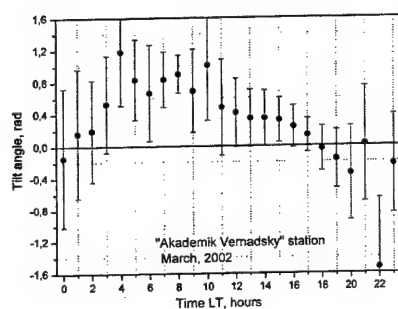
Spring equinox (August-October)



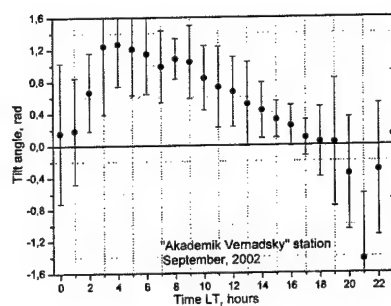
g



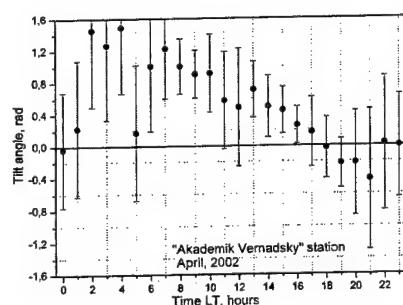
j



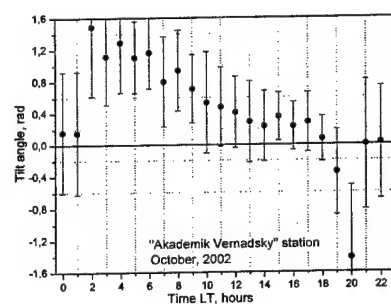
h



k



i



l

Fig. 2.1.1 Variations in the polarization ellipse orientation through 2002

g-i: about the autumn equinox (February - April);

j-l: about the spring equinox (August - October).

Table 2.2.1.

1. Operating frequency range, Hz	0.03÷300
2. Conversion factor ("gain") of the principal channel	
in the subrange 0.03 to 1 Hz, mV/nT·Hz with nonuniformity of the response function, dB	66.7±1
in the subrange 1 to 10 Hz	n/a
in the subrange 10÷300 Hz, mV/nT·Hz with nonuniformity of the response function, dB	200±1
3. Intrinsic noise level	
at 0.1 Hz, pT/Hz	7
at 1 Hz, pT/Hz	0.3
at 10 Hz, pT/Hz	0.03
at 100 Hz, pT/Hz	0.08
at 300 Hz, pT/Hz	0.007

In order to reduce the probable spurious induced signals, the complex was placed some 0.5 km away from the main building. The computer based recording system is in the ELF pavilion. The primary sensors are mounted on metal masts which are cemented in the rock near the pavilion. They are covered with hoods to be protected against atmospheric influences. The sensors are oriented along mutually perpendicular directions within the horizontal plane (one is along the geographic meridian, this is the North-South channel, and other is the East-West channel). The output signals are time series corresponding to two horizontal-plane components of the ELF magnetic field. The signals in each channel are digitized with a sample frequency of 500 Hz and recorded as 24-hour files. (Each record is started at 00:00 UT and ends at 24:00 UT). The recording is done continuously during a week. The records are interrupted for 30 minutes about 24:00 UT every Sunday to load the digital data down on a CD-R.

Shown in Fig. 2.2.1 a is a typical spectrum of the ELF signal from the NS magnetometer (integration time 10 minutes; frequency resolution: 0.12 Hz. The record was taken 14 September, 2002). One can clearly see in the Figure a set of Schumann resonance modes (Fig. 2.2.1 b, frequencies between 0.03 and 48 Hz) and the narrow line at 60 Hz (Fig. 2.2.1 c). During the wintering campaign spectral and polarization parameters were recovered for both effects.

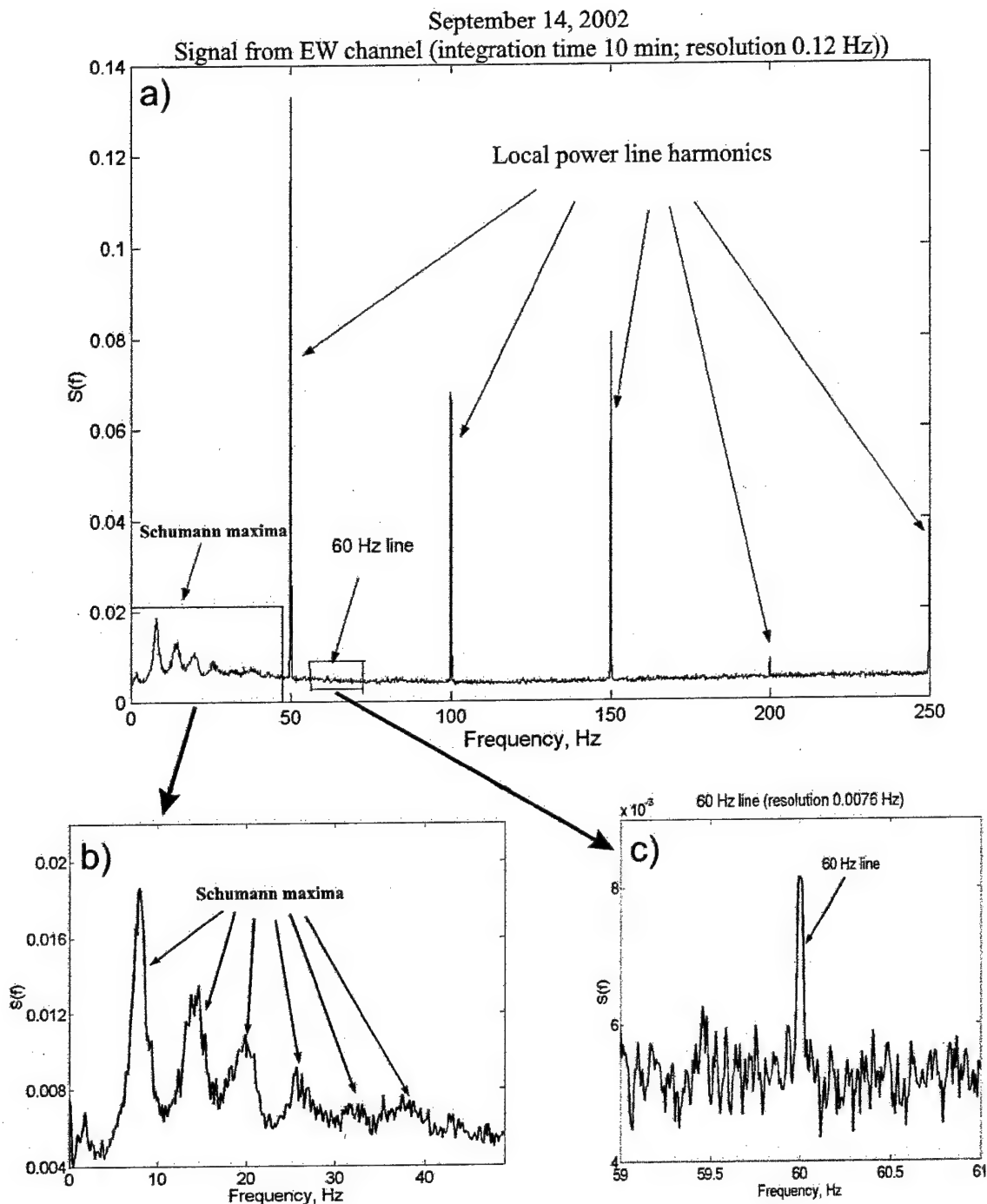


Fig.2.2.1

a) ELF noise spectrum recorded in the NS channel at 20:00 UT 14 September, 2002;

b) the range of Schumann resonances;

c) a band around 60 Hz.

2.2.2 ELF data processing in the range of Schumann resonances

Data processing was done with the aid of Matlab and the program library developed for that product. The procedure involved two stages. During Stage1 a 24-hour realization (in both the NS and EW channels) was broken up in 10-minute intervals and power and cross spectra were calculated for each of these. Series of the spectra were derived with frequency resolutions of 0.12 Hz (to be further used for identifying Schumann resonance frequencies) and 1 Hz (for estimating polarization parameters). The series of high resolution (0.12 Hz) spectra were represented visually in the form of spectrograms (see Fig.2.2.2)

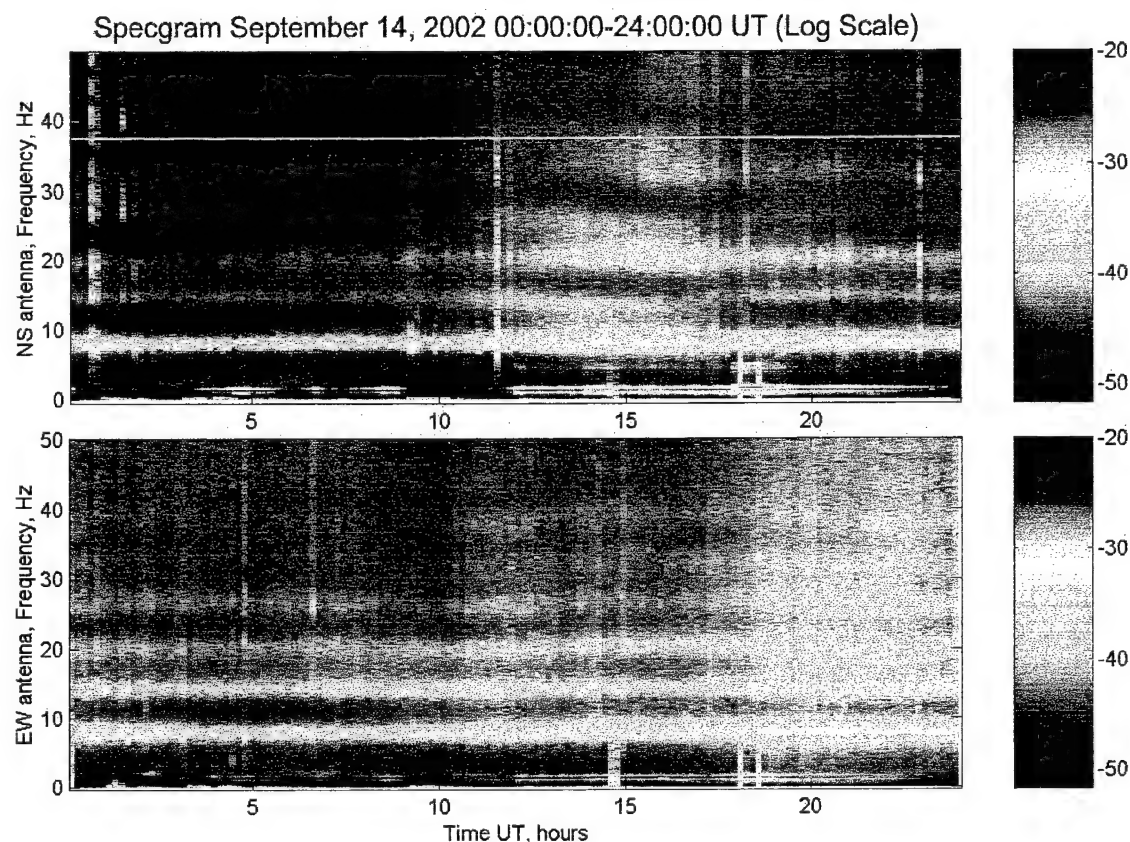


Fig. 2.2.2 ELF signal spectrogram for a 24-hour period (14 September, 2002)

The special features revealed in each 24-hour realization were catalogued, after which all the spectrograms and sets of spectra were archived on a CD-R. At Stage 2 the spectrum sets obtained were used to estimate resonance frequencies and polarization parameters of the Schumann resonances. Time dependences of these parameters (on the 24-hour scale) were determined for three lowest order modes of the Schumann spectrum. The resonance frequencies $F(t)$ were taken as the frequencies of power spectrum peaks.

The data sets with the 1 Hz frequency resolution were used for polarization analysis after the algorithm and equations of the Annual Progress Report, 2002 (Subsection 2.1). The output data were time dependences (UT) of the Stokes parameters $I(t)$, $Q(t)$, $U(t)$ and $V(t)$; orientation angle of the polarization ellipse, $\psi(t)$; ellipticity ratio $r(t)$; polarization ratio $P(t)$, and intensity $I_p(t)$ of the polarized component. Ensemble averaging was applied to derive month averaged diurnal dependences of spectral and polarization parameters of the Schumann resonances. The series of average parameters were archived on a CD-R.

Analysis of the series of spectral and polarization parameters of Schumann resonances has shown the major part of them to be characterized by pronounced diurnal dependences. Averaged diurnal run curves of the polarized component's intensity $I_p(t)$ and orientation angle $\psi(t)$ of the ellipse are given in Fig. 2.2.3 (a and b, respectively) for the first three Schumann modes.

The data relate to October, 2002. The UT-dependences of the polarized component's intensity (modes 1 and 3 of the Schumann spectrum) contain three distinct peaks corresponding to periods of maximum activity of the Asian (about 09:00 UT), African (about 15:00 UT) and American (20:00 UT) thunderstorm centers. By converting UT to local time for each of the centers one can see the maximum activity to occur in the local afternoon. This is in good agreement with the independent data on the time of maximum thunderstorm activity as derived from meteorological statistics [WMO, 1956].

The $I_p(t)$ curve for the second Schumann resonance does not show the peak near 15:00 UT which should have corresponded to the maximum activity of the African thunderstorm center. This is in agreement with the results of numerical simulation according to which the separation between the African center and the observer corresponds to an interference minimum in the field of the second resonance. The contribution of the African center to $I_p(t)$ is insignificant at the frequencies close to the second resonance mode.

Now we discuss the behavior of the polarization ellipse orientation angle presented in Fig. 2.2.3 b. The angle $\psi(t)$ varies in roughly the same way in the first and third resonance modes, showing a 'stepwise' decrease from about $+80^\circ$ to 0 and further on to $\approx -100^\circ$.

Note that, according to the theory of wave propagation in the frequency range of Schumann resonances (see Subsection 2.1 of the Annual Progress Report, 2002), the direction toward the field source is at 90° to the major axis of the polarization ellipse. This permits determining the source direction from knowledge of the $\psi(t)$ dependences. For example, the angular coordinates of the sources detectable from the data of Fig. 2.2.3 b are $+170^\circ$; $+90^\circ$ and -10° , which values

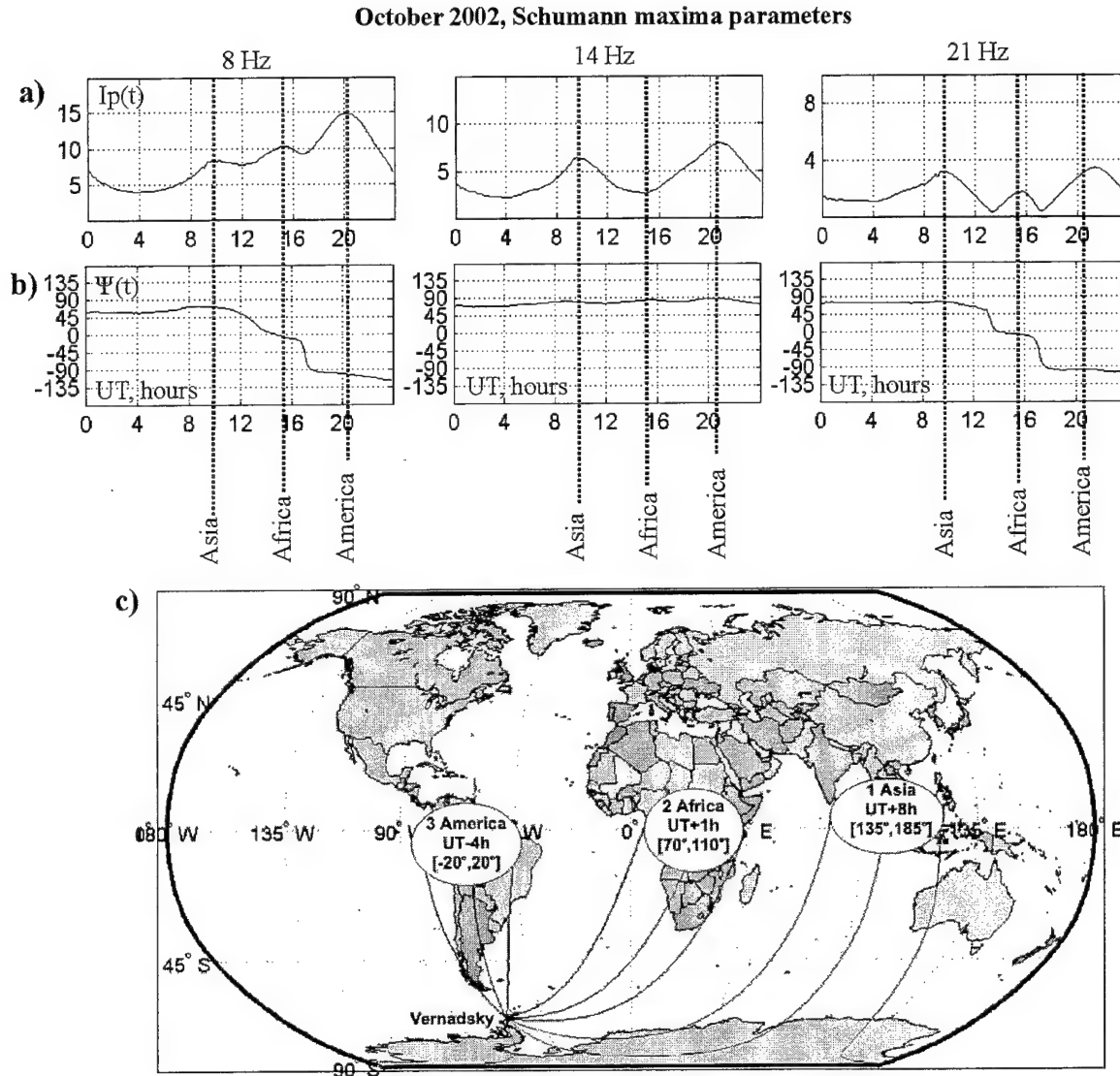


Fig.2.2.3

- a) Diurnal variations of the polarized component's intensity, $I_p(t)$, for three first Schumann resonance modes (October, 2002);
- b) diurnal dependences of the ellipse orientation angle, $\psi(t)$, for three first resonance modes (October, 2002);
- c) map locations of world centers of thunderstorm activity.

correspond to the respective azimuths of the Asian, African and American centers of thunderstorm activity (cf. the map in Fig. 2.2.3 c). In the second resonance mode the African center does not contribute to variations of the ellipse orientation. The American and the Asian centers lying on virtually the same great circle arc, the ellipse orientation of the second Schumann mode changes only very slightly through the 24-hour period, remaining close to 80° .

In order to analyze seasonal dependences of the resonance frequencies and polarization characteristics of the Schumann modes, monthly averages were derived for the diurnal variation in $F(t)$, $I(t)$, $Q(t)$, $U(t)$, $V(t)$, $\psi(t)$, $P(t)$ and $I_p(t)$ over 2001 and 2002. By the time of writing this Final Project Report, we are in possession of the averaged data for the periods of May, 2001 to December, 2001 and March, 2002 to January, 2003 (the corresponding graphic representations are given in Appendix 1). By analyzing the processed data, the Project participants have been able to detect certain regularities in the behavior of polarization parameters of the Schumann resonant fields. As has been found, the direction toward thunderstorm activity centers, as recovered from dependences of the polarization orientation, show a systematic negative shift with respect to true azimuthal angles of the field sources. The magnitude of this shift makes 10 to 15 degrees at 8 Hz and diminishes at greater 'ordinal numbers' of the resonant mode. As shown in Subsection 3.2 hereafter, this shift appears because of gyrotropic properties of the Earth-ionosphere cavity in the geomagnetic field.

Next, consider the ellipticity ratio. The magnitude of $r(t)$ in the first Schumann mode is always positive, independent of the season. The positive sign implies a clockwise rotation of the horizontal-plane magnetic component along the ellipse. In the second mode, $r(t)$ may change its sign near the autumn equinox (specifically, in March through August), while in spring (September-December) it remains positive, like in the first mode. The ellipticity ratio $r(t)$ for the third Schumann mode changes its sign during the 24-hour period throughout the year. These seasonal features of the diurnal dependences pertinent to polarization of the Schumann resonance fields may prove useful for the study of seasonal variations in the activity of world thunderstorm centers.

2.2.3 Processing of the data collected at 60 Hz.

Along with natural sources, the Earth-ionosphere cavity may be excited by powerful technogenic agents. Based on theoretical estimates, it has been suggested that the 50 Hz and 60 Hz radiation from electric power lines of the world industrial regions (USA, Europe and Latin America) is of sufficient amplitudes for being detectable at *Akademik Vernadsky*. The search at 50 Hz did not seem expedient because of the strong interference at this frequency from the local power net and the generator. Therefore, winter campaigns at *Vernadsky* involved frequency domain monitoring in the vicinity of 60 Hz. Spectral analysis has shown presence of a narrow line at 60 Hz (see Fig. 2.1.1 c). The spectral and polarization parameters of this emission were estimated in the same procedure as of the Schumann resonance modes. In view of the much smaller width of the 60 Hz line compared with the Schumann resonance peaks, the sets of spectra were evaluated

with a frequency resolution of 0.0076 Hz. The line proved to be detectable throughout the year. The spectral width and central frequency deviations of the line with respect to 60 Hz remained within a few hundredths of one hertz. Analysis of the spectral and polarization properties allows suggesting the power net of the USA as the most probable source of the radiation considered. The reasons in support of this conclusion are as follows. The estimated azimuthal angle of the radiation source, while varying through the day, always remains within the sector (cone) of angles toward the US territory (see the dot-and-dash) lines in Fig. 2.2.4 a. Also in the Figure is the bearing of the US research station *Palmer* (dotted line; the azimuthal angle is 9° . The separation from *Vernadsky* is 54 km) whose power system operates at 60 Hz. The average bearing of the radiation source under study is different from that of *Palmer* by about 40° , such that the possibility for the radiation to originate at *Palmer* should be excluded.

Both the amplitude and azimuthal angle of arrival of the 60 Hz line demonstrate a pronounced diurnal variation for all seasonal (Fig. 2.2.4 a-b). The spectrum of variations in the line amplitude (estimated for the period of March to October, 2002, see Fig. 2.2.4 c) contains, along with the diurnal, a harmonic with a weekly period. It can be interpreted as an imprint of the regular weekly changes in power consumption, or the so called weekend effect which is known to occur in global-scale power systems.

To make sure the observed line could not be generated at the station itself, a series of experiments was performed where suspected sources of narrow band interference were switched off, however the emission line remained detectable. Besides, the line was observed with the same intensity and same azimuthal angle of arrival in the experiment that was carried out at a remote site on the Antarctic continent. The data taking complex was removed 12 km away from the station.

Thus, it can be stated that a ELF radiation line from the US electric power system has been detected for the first time in Antarctica. Analysis of parameters of the emission line permits a non-contact diagnostics of the level of consumption from the electric power system of the North American continent.

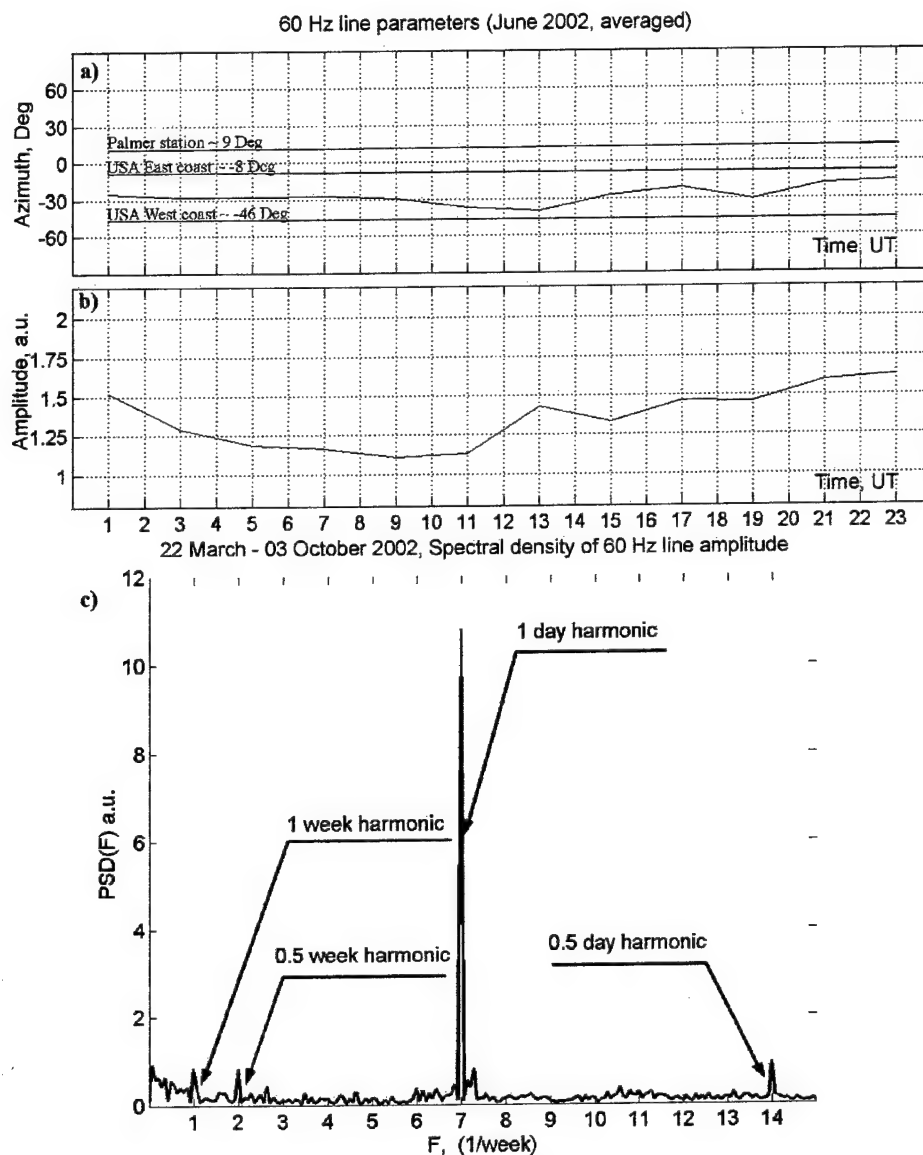


Fig. 2.2.4

- a) Azimuthal angle of the direction toward the source of the 60 Hz radiation (June, 2002):
Average diurnal variation;
- b) Amplitude of the 60 Hz radiation: Average diurnal variation (June, 2002);
- c) Spectrum of amplitude variations of the 60 Hz line (March to October, 2002).

2.3 HF observations at Akademik Vernadsky in Antarctica and measurements in the course of the marine expedition

Non contact monitoring of the dynamic way in which the plasma environment responds to disturbances of various kind is effective with coherent techniques of ionospheric sounding. One of the coherent methods developed at IRA in late 1980s [V.S. Beley, et al., 1991] is the frequency-and-angular sounding of traveling ionospheric disturbances (TIDs). Its distinctive feature is the use of HF broadcasting transmitters as sources of diagnostic radiation, with angles of wave arrival and Doppler frequency shifts of the ionospherically scattered signals playing the part of input data in the algorithms of TID parameters recovery. As has been shown within this Project [Kascheev, et al., 2000], the approach can be useful for radio sounding of the rough sea surface.

2.3.1 HF research equipment

A special triple-channel coherent data taking complex has been developed at IRA to study experimentally the processes responsible for the transfer of near-surface atmospheric disturbances to ionospheric altitudes and the geospace. The system was initially tested during the marine part of the 7-th Antarctic mission and later deployed at *Akademik Vernadsky*. It was used successfully in the 2002/2003 South winter campaign. The structural diagram is given in Fig.2.3.1. It involves the antenna/transmission line system, the triple-channel receiver and a data processing/visualization unit.

The receive antennas have been made as symmetric horizontally oriented dipoles and vertical monopoles, which configuration permits radio reception in both polarizations. The earth surface around the monopoles has been 'metal-clad' with a few radially placed copper wires. To ensure the required mechanical strength, the physical sizes and, accordingly, effective heights of the antennas were selected at the lowest level allowable from the point of detectability of emissions from broadcasting radios of Chile, Argentina and Uruguay. The wooden supports of the antennas are of T-geometry with cross-bass to provide rigidity (see Fig. 2.3.2). The support is 3-m high and the horizontal bar is 3-m long. The bar carries the symmetric dipole, while the monopole is fixed on the vertical mast of the support. The dipole is oriented along the East-West direction, such that the peak of the horizontal-plane reception pattern is along the North – South line. The azimuthal (horizontal-plane) pattern of the monopole is isotropic. The allocation of the antennas at *Vernadsky* is shown schematically in Fig. 2.3.3. The sites denoted as points 0, 1 and 2 in the Figure are placed at rocky natural heights that are free from snow in winter. Since coordinates of these points need to be known to a good accuracy to allow recovering absolute values of the

radio wave's angles of arrival, they were determined with the aid of precision GPS equipment to within 10 cm.

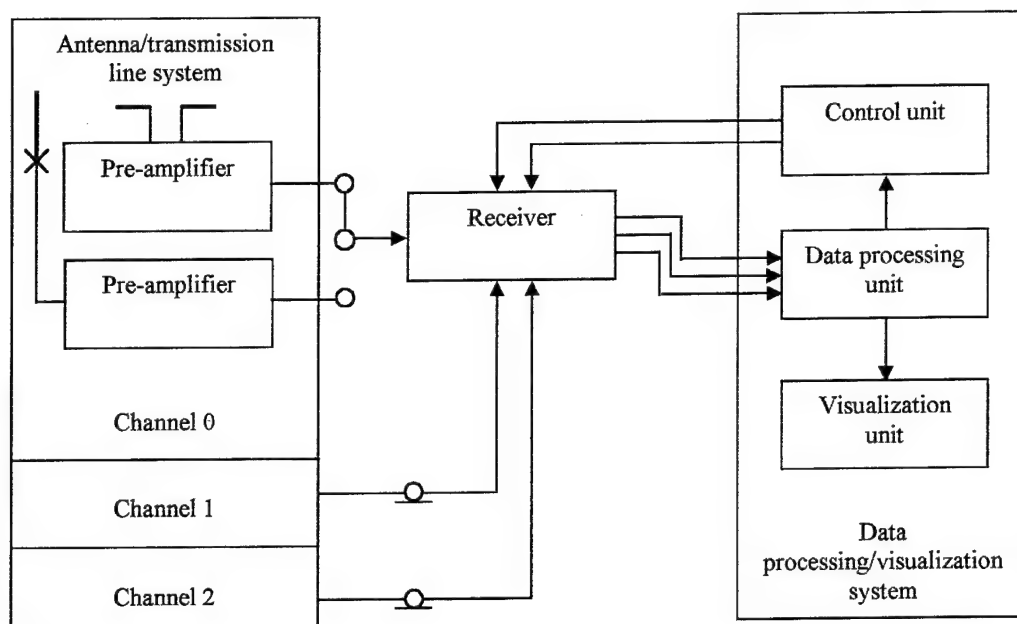


Fig. 2.3.1 Schematic of the data taking complex

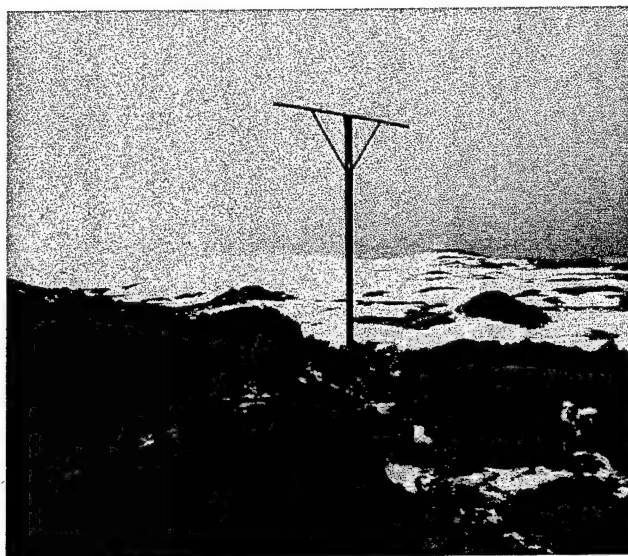


Fig. 2.3.2 HF antenna

The transmission line can be connected by an operator either to the horizontal or to the vertical antenna. Shown in Fig. 2.3.4 is the functional diagram of the triple-channel receiver. Each channel is embodied as a single-conversion receiver characterized by absence of selective circuits at the front and. This simple solution has been possible owing to the use of a double

balanced mixer (built around an analog multiplier with a large dynamic range) at the input, plus the relatively quiet noise environment in Antarctica.

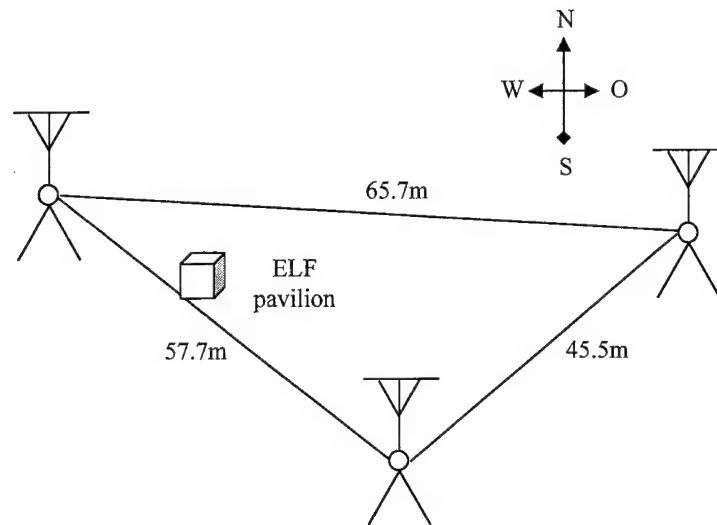


Fig. 2.3.3 Layout of HF receive antennas at *Vernadsky*

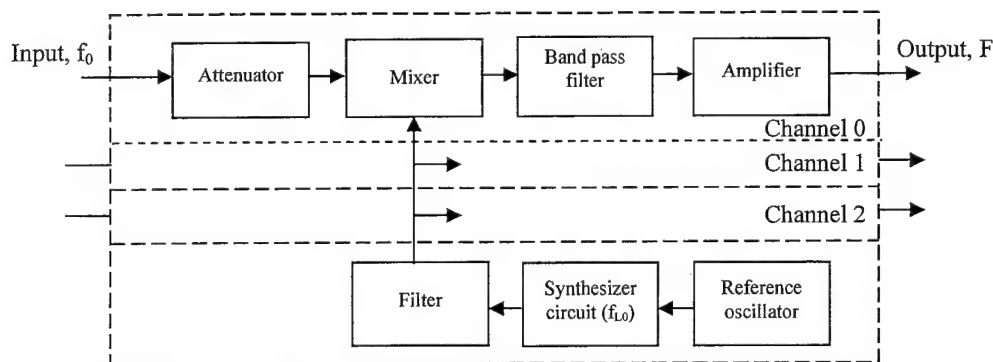


Fig. 2.3.4 Functional diagram of the receiver

The input signal of frequency f_0 is fed to the attenuator and further to the mixer. The other input of the mixer receives the local oscillator voltage which is common to all three receive channels. The LO frequency is close to f_0 . The bandpass filter at the mixer output selects the difference frequency F . The filtered voltage is the down-converted carrier-frequency voltage of the broadcasting radio, cleared of modulation components. It is amplified and fed to the analog-to-digital converter in the data processing/visualization system.

The receiver can be controlled either manually or in a programmed way, with the controllable parameters being frequency setting and level of attenuation at the input.

The basic receiver specifications are listed in the Table below.

Table 2.3.1

Parameter	Magnitude
Threshold sensitivity within the 15 Hz, μV	0.7
Passband width at -3dB level, Hz	15.0
Dynamic range, dB	60
Maximum output voltage across a $R_H = 200\Omega$ load, V	8
Frequency adjustment step, Hz	1.0
Operating range, MHz	1.0 ... 32.0
Scale time of frequency adjustment, ms	50
Phase-difference instability over a three-hour period for an arbitrary pair of receive channels (with VSNR = 40 dB), degrees	± 0.2

The data processing/visualizing system is the end unit of the data taking complex. It is used for controlling the receiver, converting the raw observational data to the digital form and computing (in quasi-real time) the angles of arrival and Doppler frequency shifts of the probing signals. The data processing/visualization system provides for visualization and archiving of the measured results.

Signal processing is performed automatically through a package of dedicated applied software.

2.3.2 Methodology of measurements

The angular-and-frequency sounding technique permits recovering TID parameters from the data measured on single-hop propagation paths. For this reason, the measurements were preceded by selecting a broadcast transmitter that would lie at closer distance from *Vernadsky* than 3500 km and radiate at a frequency sufficiently close to the F-layer MUF of the specific radio path for minimizing the number of propagation hops. Next, the receive antenna polarization was chosen so as to conform to the needs of the experiment. The polarization was to be horizontal when investigating ionospheric disturbances at *Vernadsky* and vertical for studying radio wave scattering by the sea surface during the marine expedition.

The data taking complex was deployed at *Vernadsky* in April, 2002 to monitor ionospheric disturbances, and was operated in that mode continuously till early February, 2003. The principal

source of diagnostic signals was the HF broadcasting station – Radio SGO (Santiago de Chile, $33^{\circ}27'S$; $70^{\circ}41'W$) lying at 3500 km from *Vernadsky*. The operating frequencies were 21500 kHz and 21550 kHz in the daytime, and 15375 kHz at night. In summer, the diagnostic signals normally were detectable 24 hours a day. In winter the night-time frequency of 15375 kHz ceased being detectable, so day-time records alone are available for the winter period. The propagation conditions of 15375 kHz improved by the spring, which permitted returning to the 24-hour cycle of observations.

The length of the Santiago-*Vernadsky* radio link is at the upper limit for single-hop propagation, while closer lying broadcast stations were not found in the air. Therefore, to check the possibility of using alternative sources of radiation, a cycle of test measurements was carried out in 2002-2003, which involved communication rather than broadcasting transmitters at shorter distances from *Vernadsky*. In particular, the transmitters of the Antarctic research stations *Arctowski* (Poland) and *Bellingshausen* (Russia) were tried, both located at King George Island about 450 km from the Ukrainian station. The measurements were conducted for various seasons, different ionospheric conditions and with transmitters of different power. As a result, it has been found out that low power transmitters (about 100 W) can be effective for TID monitoring at short radio links.

Totally, about 3000 hours of records have been obtained with the HF data taking complex over the period of regular ionospheric monitoring in the Antarctic Peninsula area.

The scattering of radio waves by the sea surface was studied during the marine part of the 7-th Antarctic mission, mostly when the ship stayed anchored at sea. Special emphasis was made on selecting such radio links where the signal propagated in a single mode, which permitted minimizing the errors. For this purpose, the received spectrum was monitored continuously through the experiment. At the same time, oceanographic parameters (wind speed and direction, and sea wave heights) were measured by alternative methods. Later on, these data were used in a theoretical model of the scattering process to calculate power spectra of the scattered radio signal. Measured radio spectra were averaged according to a specially developed algorithm and compared with the calculations. Results of the comparison will be presented hereinafter.

The HF data taking complex, developed and manufactured at IRA, has been successfully used in the programs of sounding ionospheric disturbances and studying the radio signals scattered by the rough sea surface. The sources of diagnostic radiation in these programs were broadcasting radios of South America. Such techniques permit increasing the potential of radio methods for the study of energy transfer between the lower and upper atmospheres in Antarctica, and suggest vast experimental material for the development of physical models.

2.4 HF heating experiment with a ELF modulation

The international measuring campaign on ionospheric modification was carried out 26 to 30 October, 2002. The ionosphere was 'heated' with electromagnetic waves from a powerful transmitter in Tromsø, Norway (69.7° N; 19° E) which was active from 2:00 to 8:00 UT on the first four days of the campaign and from 4:00 to 12:00 UT on the last day. The radiation frequency was varied between 4040 kHz and 7953.717 kHz. In most cases the heater radiated a spectrum consisting of two components separated by 19 Hz or 22 Hz. The receiving sites were at the station *Akademik Vernadsky* in Antarctica ($65^{\circ}15'$ S; $64^{\circ}16'$ W) and at the Institute of Radio Astronomy Observatory in Grakovo (Kharkov Region, Ukraine; $49^{\circ}40'$ N; $36^{\circ}50'$ E). The HF signals were sought for in a ≈ 300 Hz band near the fundamental frequency of the powerful transmitter and close to its second- and third-order harmonics. Also, ELF noise was monitored in the vicinity of the difference of the transmitted frequencies. The measurements were aimed at detecting a nonlinear ionospheric response to the powerful HF radiation, which would manifest itself through enrichment of the signal spectrum.

2.4.1 HF detection

In Antarctica, the HF signals were detected with a single-channel coherent receiver. The antenna was a symmetric horizontal dipole whose reception pattern was oriented toward the radiation facility. The output signal at IF2 was fed to an ADC (the passband about IF2 was 300 Hz). The ADC sampling rate was $f_s \approx 700$ Hz. Further on, the signal was processed in a digital form. During the experiment, the receiver was adjusted alternatively to the fundamental frequency and second-order harmonic of the heating transmitter, in order to detect the possible nonlinear response.

In Ukraine the fundamental and the higher-order harmonics were received separately. The fundamental frequency was monitored continuously, using a vertical monopole as the receive antenna. The bandwidth at IF2 was 300 Hz and the digital sampling rate ≈ 682 Hz.

The fundamental frequency was clearly seen both in Antarctica and in Ukraine for nearly 50% of the experimental time.

2.4.2 Results and discussion: Special features

The HF spectra received at the operating frequency of the powerful transmitter often demonstrated fluctuations in Grakovo, Ukraine as well as in Antarctica. The received frequency varied within ≈ 10 Hz, while spectrum widths could change in broad limits from 1 Hz to several tens of hertz. The spectrum width detected in Antarctica on the last day of the measuring campaign reached a value close to 40 Hz at the carrier of 7953.717 kHz (see Fig. 2.5.1), which resulted in a failure to resolve the two radiation frequencies separated by 19 Hz. Comparison of the heater spectrum with that of the ionospherically reflected signal from a reference HF transmitter (Radio RWM of Moscow, Russia – Fig. 2.5.2), which was received in Antarctica during blanks of the heater operation, shows the two spectra to be highly different. Radio RWM radiated pulses with a 10 Hz repetition frequency, and its spectrum practically was not deteriorated along the propagation path. The spectra of the Tromsø transmitter often demonstrated two components observable at the reception sites. It can be seen, for instance, in Fig. 2.5.3 that the spectrum consists of a frequency-stable narrow band component and a ‘floating’ broad-band part. Besides, the broad-band components of the dynamic spectra recorded in Europe and in Antarctica show a reasonably high correlation both in frequencies (Fig. 2.5.3 and 2.5.4) and in amplitudes (Fig. 2.5.5 and 2.5.6). In other words, parameters of the Tromsø signal in Antarctica are drastically different from such of the signal from the mid-latitude Radio RWM which arrived along a similar path, while showing correlation with the heater’s signal in Grakovo that propagated under different conditions. Next, analysis of the data received at *Vernadsky* suggests that reception conditions were better when the heater radiated in O-mode than in the case of X-mode. Variation in the carrier frequency with characteristic periods about 10 s were detected in the signals of the Tromsø transmitter but never in the signals from Radio RWM.

The features noted in the behavior of signals from the ‘heating’ transmitter indicate that essential control over their structure and parameters is not due to the medium on the propagation path but rather to processes occurring directly above the powerful transmitter, i.e. inside the artificial turbulence (AIT) domain. Most probably, the broad-band component in the received spectrum is due to signal scattering from the artificial turbulence stimulated by the same signal.

Consider the geometric layout in greater detail. The Tromsø bearing from *Vernadsky* is 229.1° , while that of Grakovo is 147.6° . The angle between the two directions is 81.5° . Thus, we have obtained a roughly orthogonal reference basis which could be used for estimating plasma drift

motions within the horizontal plane from measurements of the Doppler frequency shifts at spaced observation sites.

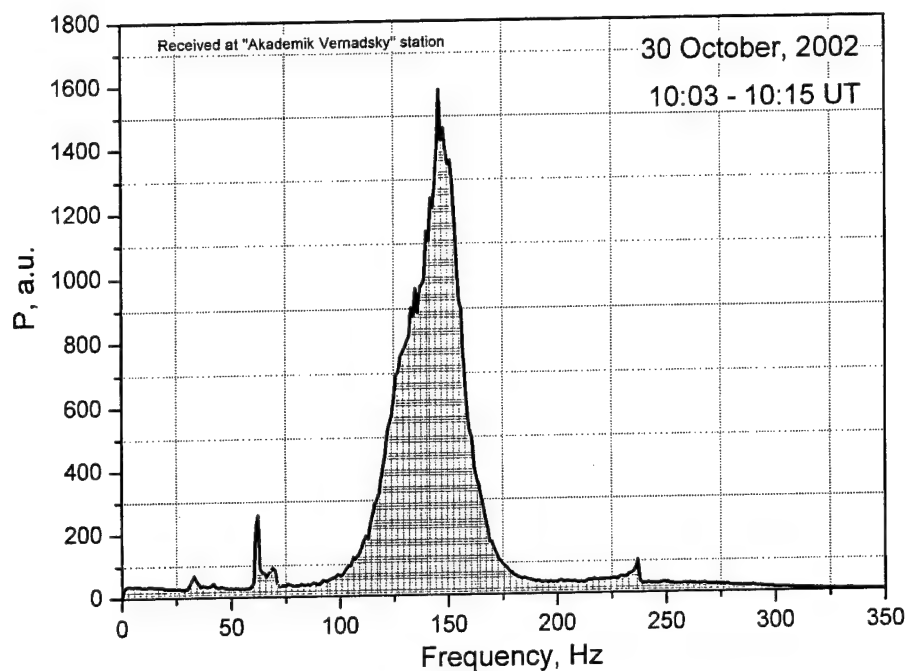


Fig. 2.4.1 Power spectrum of the HF signal from the 'heating' transmitter. The facility radiated at $f_{01} = 7953.717$ kHz and $f_{02} = 7953.698$ kHz October 30, 2002. (The spectrum has been averaged over the period 10:03 to 10:15 UT).

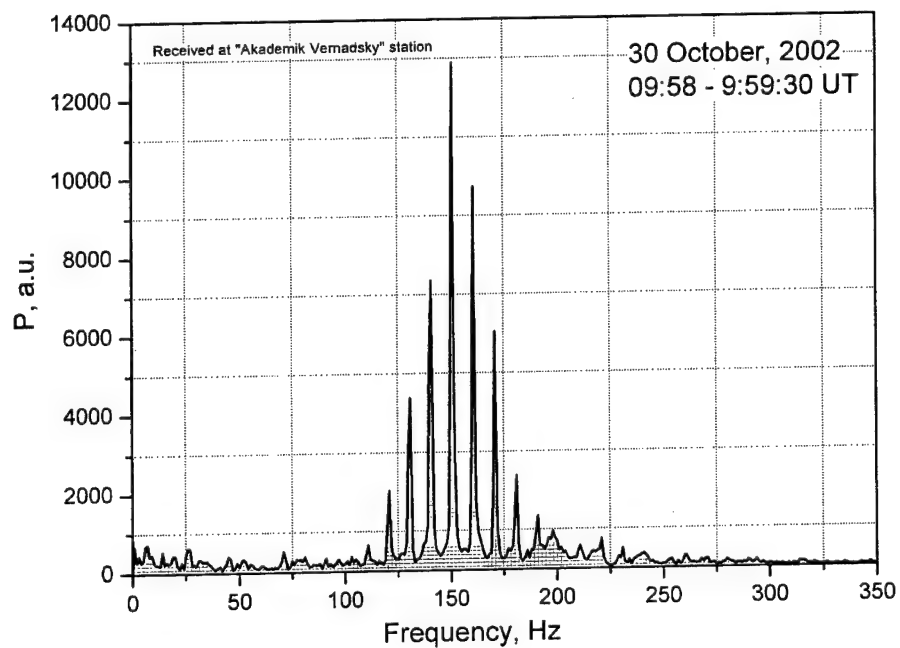


Fig. 2.4.2 Power spectrum of Radio RWM (Moscow, Russia) that radiated pulses with a 10 Hz repetition frequency at $f_0 = 9996$ kHz 30 October, 2002. (The spectrum has been averaged over the period 9:59:30 UT).

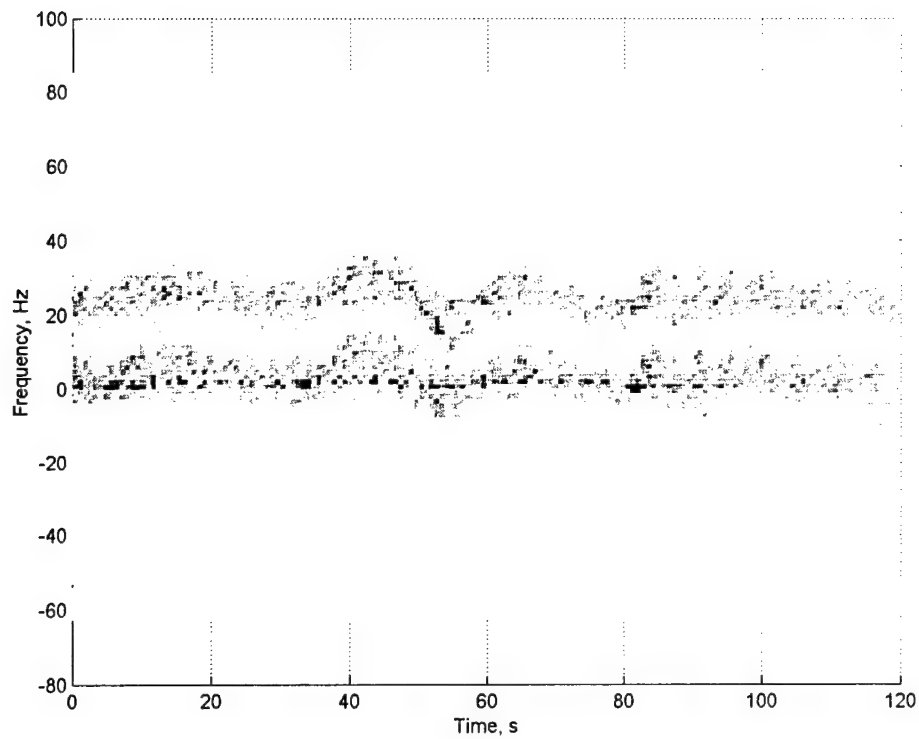


Fig. 2.4.3 Dynamic spectrum of the HF 'heater' signal received at Grakovo, Ukraine 27 October, 2002 (3:49 to 3:51 UT)

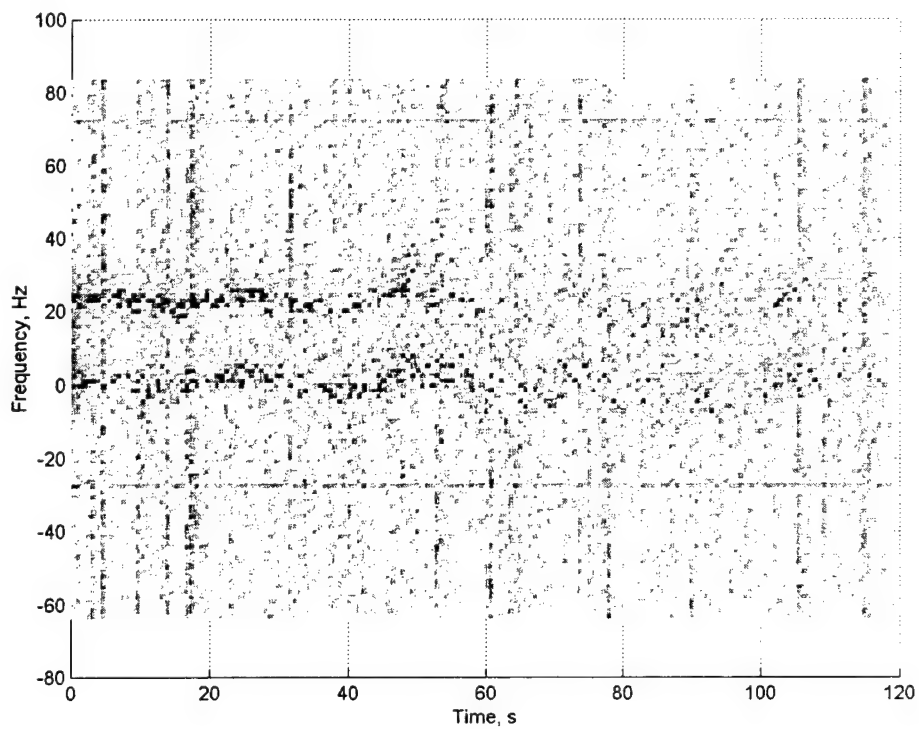


Fig. 2.4.4 Dynamic spectrum of the HF 'heater' signal received in Antarctica 27 October, 2002 (3:49 to 3:51 UT).

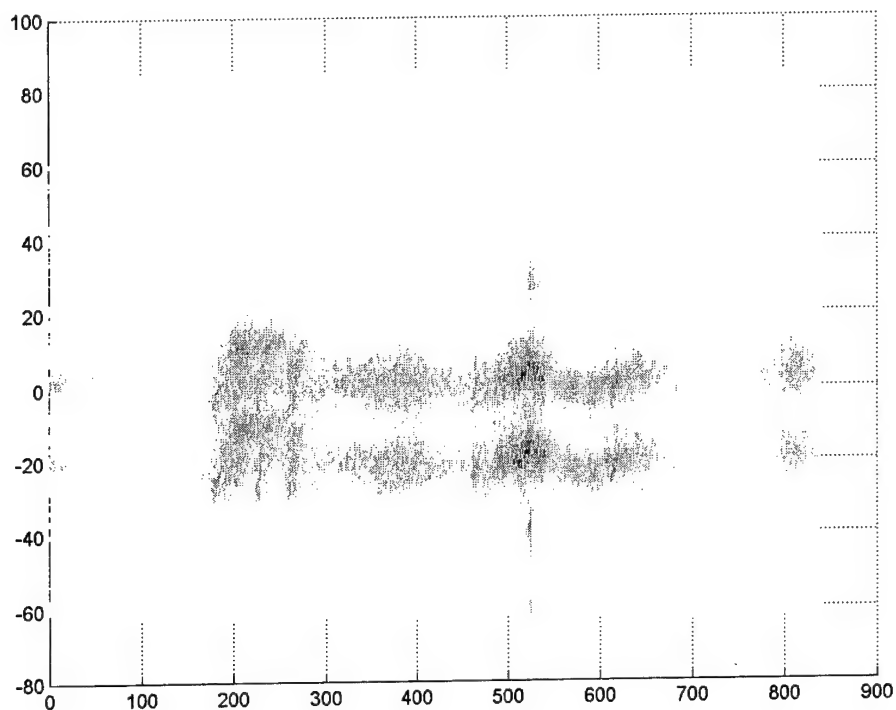


Fig. 2.4.5 Dynamic spectrum of the HF 'heater' signal received at Grakovo, Ukraine
29 October, 2002 (2:01 to 2.15 UT)

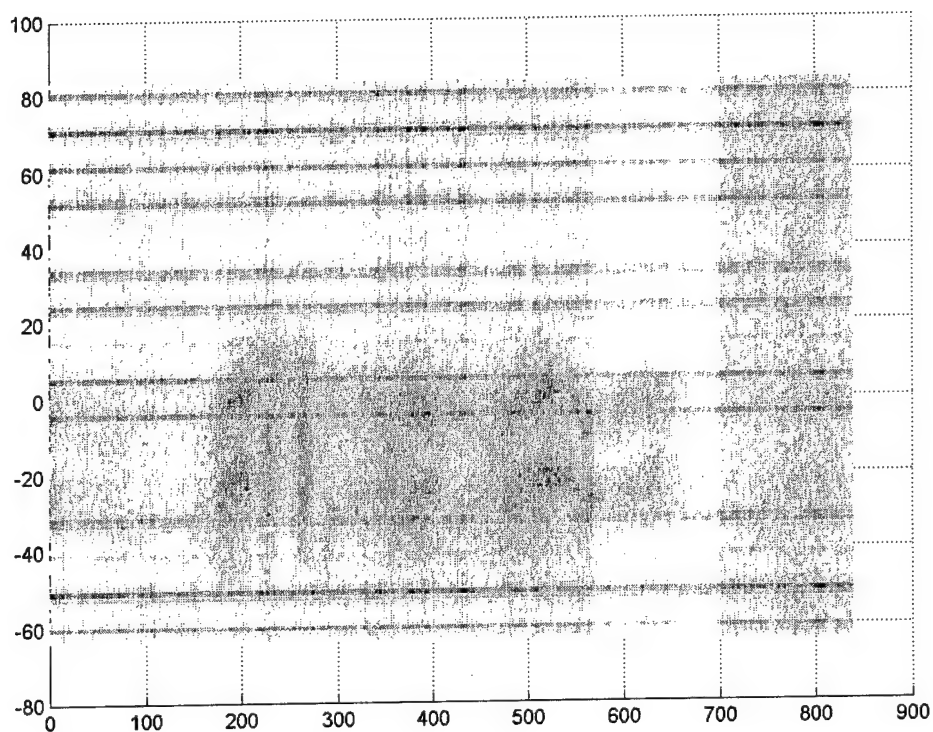


Fig. 2.4.6 Dynamic spectrum of the HF 'heater' signal received in Antarctica
29 October, 2002 (2:01 to 2:15 UT)

The simultaneously occurring variations in the signal frequency of characteristic period ≈ 10 s admittedly arise from plasma motion in the field of hydromagnetic waves propagating through the AIT. Assuming a predominantly horizontal motion of the plasma inside the turbulent volume and horizontal-plane orientation of the scattered wave vectors in the diagnostic radiation, it is possible to suggest estimates for plasma velocities. A 10 Hz Doppler frequency shift with the 5000 kHz carrier suggests an estimate of 600 m/s for the velocity projection on the scatterer-receiver line.

Thus, we have got an original method for investigating the AIT volume with the aid of a 'self-scattered' signal which can be received by standard receive facilities with a simple antenna. By receiving in Antarctica HF signals from a powerful transmitter some 16000 km away, it proves possible to recover parameters of plasma motion in the Northern auroral ionosphere and even recover the spatial structure of that motion if spatial diversity reception is available.

Slow variations in the intensity of the HF signal received in Antarctica are of special interest. During the experiment, there were periods when the solar terminator crossed the receive and the transmit sites simultaneously. As a result, the conditions of radio wave propagation could undergo substantial changes, and hence give rise to variations of the signal intensity at the receive site. The dynamics of the HF signal intensity as received in Antarctica 27 October, 2002 is given in Fig.2.4.7. The peak of intensity about 6:00 UT is indeed associated with passage of the solar terminator across *Vernadsky* ($\approx 2:00$ LT) and the 'heating' transmitter (7:00 LT). The other peak of intensity near 2:30 UT might be associated with passage of the sunset terminator across the receive site alone.

In contrast to the Antarctic station, the receive site at Grakovo, Ukraine reported of detecting the HF signal regularly not only at the fundamental frequency but at the second and third-order harmonics as well. (The total time during which the signal level at the harmonic frequencies exceeded external noise was roughly one half of the reception time at the fundamental frequency). An example is given in Fig. 2.4.8., showing the instantaneous spectrum of the signal received with the receiver tuned to the second harmonic of the heater frequency. The record has been taken with a relatively high signal-to-noise ratio. The spectral peak1 in the figure corresponds to the frequency $2f_1$, peak 2 to $2f_2$, and peak 3 to $f_1 + f_2$, where f_1 and f_2 are the two frequencies radiated by the powerful transmitter. (In the course of this experiment they were separated by 22 Hz). A thorough analysis of the temporal behavior shown by the spectral maxima and laboratory simulation of the spectra has led us to the conclusion that peaks 1 and 2 were intrinsic second-order harmonics of f_1 and f_2 generated in the transmitter, while peak 3, most probably, resulted from nonlinear effects in the ionosphere. Rather similar results were

obtained when the receivers were tuned to the third-order harmonic. The high-amplitude peaks at $3f_1$ and $3f_2$ were generated in the equipment, while the lower peaks at $2f_1 + f_2$ and $f_1 + 2f_2$ resulted from ionospheric nonlinearity.

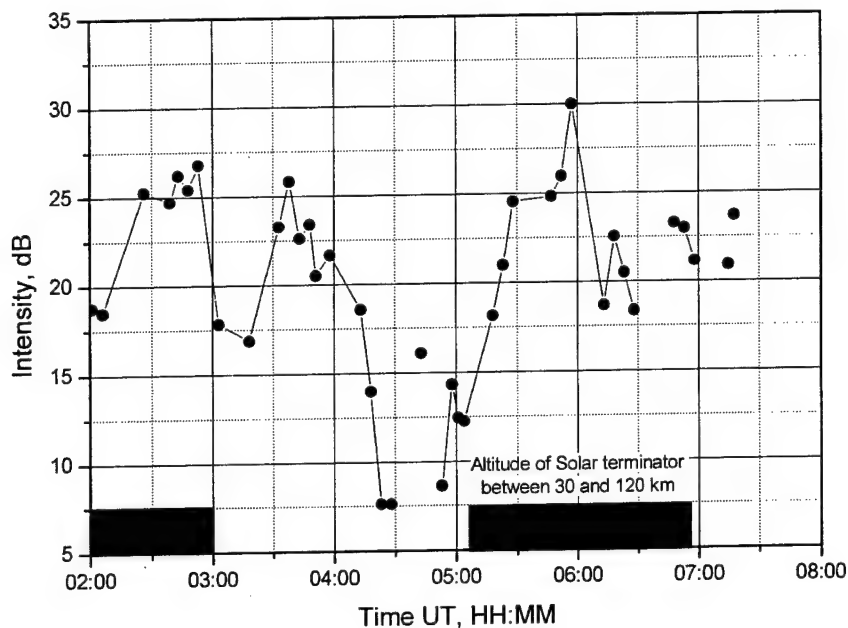


Fig. 2.4.7 Intensity fluctuations of the HF signal received in Antarctica 27 October, 2002.

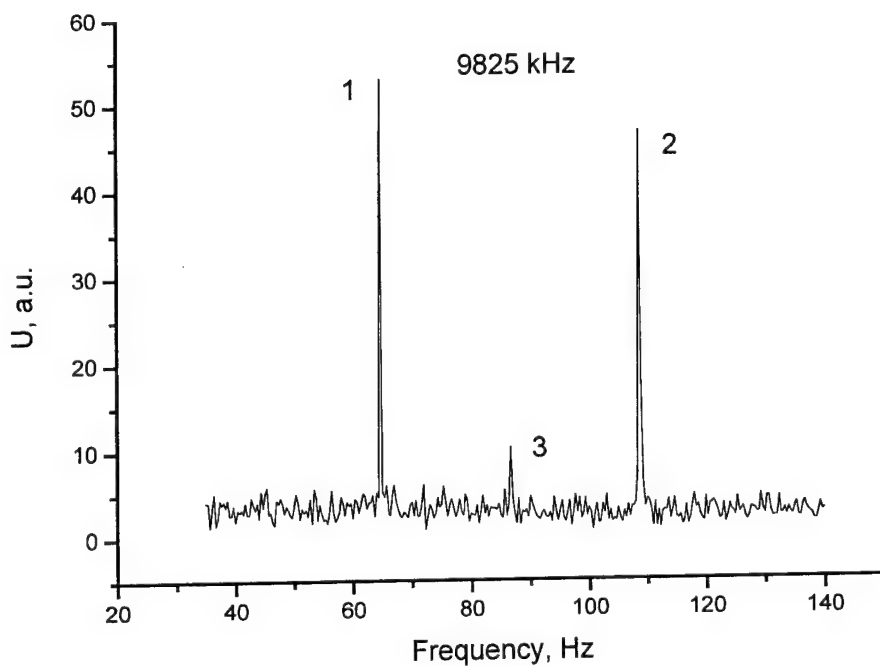


Fig. 2.4.8 The spectrum received 27 October, 2002 at the double frequency of the 'heating' transmitter (observation time 4:15 UT)

The experiment with the heating transmitter permits conclusions as follows. The powerful radio wave from the heater stimulates artificial turbulence in the ionosphere, after which it undergoes substantial alterations itself. By receiving this signal at spatially separated sites it might be possible to solve the inverse problem of evaluating parameters of the turbulence and of the natural wave processes coupled to that. The measurements permitted observing nonlinear effects in the modified region which led to the appearance of higher-order frequency harmonics, initially absent in the radiated spectrum of the transmitter.

In addition, the experiment revealed wave guiding properties of the solar terminator which canalized the radiated HF power to extremely long distances. Owing to the great number of HF transmitters operating in the world (over 6000, according to I.T.U.), the situation where the terminator passes simultaneously through a receive site in Antarctica and a transmitter in the Northern hemisphere may be expected for each season.

3 ULF / ELF WAVE PROPAGATION THROUGH THE ATMOSPHERE: THEORETICAL MODELS

3.1. Magnetohydrodynamic (MHD) waves in the ionosphere

3.1.1 Ultralow frequency (ULF) magnetic field variations

Quasiperiodic magnetic field variations characterized by scale times of seconds to tens of minutes, known as (micro)pulsations are carried through the magnetosphere and ionosphere by hydromagnetic (MHD) waves lying in the frequency range $\omega < \Omega_i$ (Ω_i is the ion gyrofrequency). Wave disturbances of the kind play an important part in the energy exchange between the magnetosphere and ionosphere, influencing essentially the electromagnetic 'climate' at middle and high latitudes. Detectable ground signatures of pulsations, i.e. the magnetic (electric) field components recordable at the surface appear as a result of the hydromagnetic-to-electromagnetic mode conversion which occurs in the localization area of transverse conductivity currents, at the plasma – neutral atmosphere interface.

The theory of MHD wave propagation through the magnetosphere, including the formation of eigenfrequency spectrum and spatial structure of pulsations, has been developed in a great many papers, starting with the fundamental work of Dungey [1954]. The advance was toward allowance for ever more realistic models of the magnetic field structure, coupling of field-line and cavity mode resonances, and for the MHD wave – ionosphere interaction [see, e.g. the review of Pilipenko, 1990].

Discussed in this Section of the Report is the propagation of ULF waves through the magnetosphere – ionosphere – atmosphere system, with emphasis on the spatial and polarizational field structure in the ionosphere and near the Earth surface. Theoretically, this problem can be separated from determination of eigenmodes of the resonant magnetic lines or the magnetospheric cavity as a whole, to be analyzed within a plane stratified model with rectilinear lines of force of the mean geomagnetic field. An important feature of the model is allowance for the finite dip angle of the geomagnetic field with respect to the horizontal plane (ionospheric boundary) as that is the angle to control the reflection and conversion of MHD and electromagnetic fields at the neutral atmosphere – ionized atmosphere interface. The model accounts for the principal physical effects of ULF wave propagation through the ionosphere, like amplitude "screening" and phase rotation, mode conversion at the reflecting boundary, etc. and permits a reasonably full description of the spatial structure of both magnetic and electric field

components of the ULF disturbance within the range of 0 to ~ 400 or 500 km above the Earth surface [Zalizovski et al., 2001].

Let the z axis of a Cartesian frame be oriented vertically down, the x -axis toward geographic North and y toward East (see Fig.3.1.1). The upper half-space, $z < 0$, which is filled with a cold magnetoplasma represents the outer ionosphere and the magnetosphere. The lower half-space involves the neutral atmosphere, $0 < z < h$, and the 'semi-conducting' Earth, $z \geq h$ which is characterized by the complex dielectric constant $\varepsilon_T = i \frac{4\pi\sigma(\omega)}{\omega}$. (Here $\sigma(\omega)$ is the specific conductivity of the ground and ω the circular frequency of the monochromatic wave; $|\varepsilon_T| \gg 1$). The two half-spaces are separated by the anisotropic plane $z = 0$ carrying surface currents of density \vec{j} , i.e. the lower ionosphere with the electric parameters $\sigma_{p,H} = \Sigma_{p,H} \delta(z)$. Here $\delta(z)$ is Dirac's delta function, while $\sigma_{p,H}$ and $\Sigma_{p,H}$ are, respectively, the specific and integrated Pedersen and Hall conductivities. In reality $\sigma_{p,H}$ reach their maximum values in the ionospheric E-region.

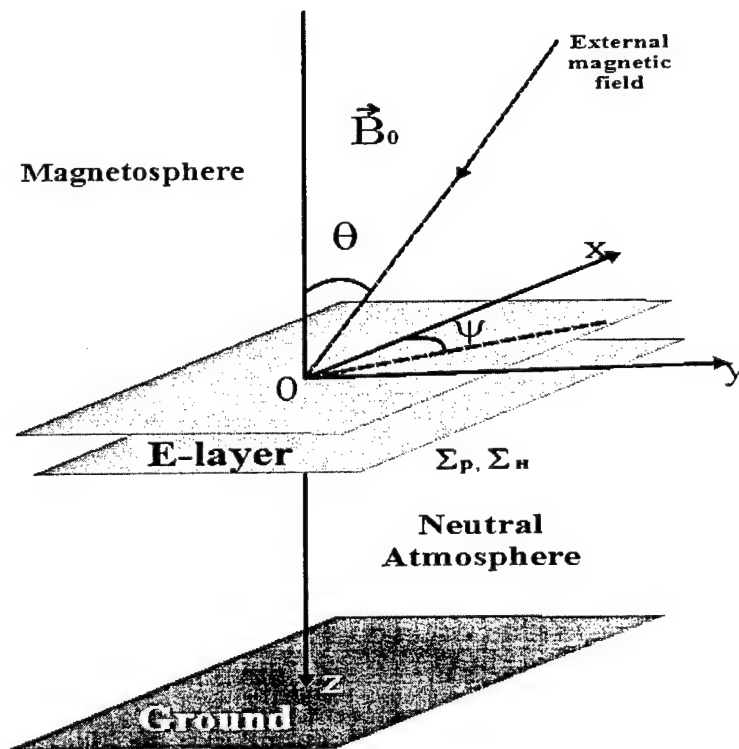


Fig. 3.1.1 Multiple-layered model of the magnetosphere-ionosphere-atmosphere system

As is known [Lyatsky and Maltsev, 1983], the low-frequency ($\omega < \Omega_i$) eigenmodes of the magnetoplasma are the Alfvén and fast magnetoacoustic modes which can be conveniently

described within a frame of reference tied to the mean geomagnetic field \bar{B}_0 . Therefore, we will introduce another rectangular frame, (ξ, η, ζ) , whose ζ -axis will be along the magnetic vector \bar{B}_0 and ξ and η across that. It is rotated with respect to the (x, y, z) frame by the angles θ and ψ , where $\theta = \frac{\pi}{2} - I$; I is the magnetic dip angle and ψ the magnetic declination at the current point of observation. Each of the plane MHD waves of the upper half-space is of form $\exp(\pm i\gamma\zeta + iq\xi + ip\eta)$, where $\gamma = k_A = \frac{\omega}{V_A}$ in the case of Alfvén or $\gamma = (k_A^2 - q^2 - p^2)^{1/2}$ in the case of fast waves; $V_A = \frac{B_0}{\sqrt{4\pi N_i M_i}}$ is the Alfvén velocity, and N_i and M_i are, respectively, the number density and mass of the ion species prevailing at this ionospheric altitude. The electric (magnetic) vector component right above the reflecting surface $z = 0$ is given by the integral over the angular spectrum of the MHD waves arriving from the magnetosphere, i.e. over all values of p and q both for the alfvénic and the compressional (magnetoacoustic) modes,

$$\begin{aligned} \bar{E}(\bar{r}, \omega)|_{z=0} = & \int dq'_1 dp'_1 \left\{ \Phi_1(p'_1, q'_1) \left(\bar{e}_\xi + \bar{e}_\eta \frac{p'_1}{q'_1} \right) \cdot \exp\left(ik_A \zeta + iq'_1 \xi + ip'_1 \eta\right) + \right. \\ & \left. + \int dq'_2 dp'_2 \left\{ \Phi_2(p'_2, q'_2) \left(\bar{e}_\eta - \bar{e}_\xi \frac{p'_2}{q'_2} \right) \cdot \exp\left(i(k_A^2 - q_2'^2 - p_2'^2)^{1/2} \zeta + iq'_2 \xi + ip'_2 \eta\right) \right\} \right. \end{aligned} \quad (3.1.1)$$

In the simpler case it can be written as a sum of two incident waves,

$$\bar{E}(\bar{r}_\perp, z=0) = \bar{e}_\xi A_a \exp(ik_A \zeta + iq_1 \xi + ip_1 \eta) + \bar{e}_\eta A_f \exp\left(i\sqrt{k_A^2 - p_2^2 - q_2^2} \zeta + iq_2 \xi + ip_2 \eta\right) \quad (3.1.2)$$

The total field in the magnetosphere/upper ionosphere involves incident and reflected waves, with each of the incident modes (alfvénic and magnetoacoustic likewise) give rise to two reflected, owing to the anisotropy of the $z = 0$ boundary. The reflection of MHD waves at $z = 0$ and MHD-to-electromagnetic mode conversion at the boundary can be analyzed conveniently for plane wave components that are Fourier-transformed in the horizontal plane (x, y) . It is the horizontal-plane wave vector components that should remain conserved in the reflection/transmission process. The magnitudes, $k_x = m$ and $k_y = n$, are related to p and q through.

$$\begin{aligned} m &= \gamma \sin \theta \cos \psi + q \cos \theta \cos \psi - p \sin \psi \\ n &= \gamma \sin \theta \sin \psi + q \cos \theta \sin \psi + p \cos \psi, \end{aligned} \quad (3.1.3)$$

which equations permit deriving transformation rules for the reflected p and q . For example, if the incident wave is an Alfvén mode with the transverse wavenumbers p_I and q_I , then equations (3.1.3), plus the MHD dispersion laws yield

$$q_{11} = q_I + 2k_A \tan \theta \quad (3.1.4)$$

for the reflected Alfvén wave and

$$q_{12} = q_I \cos^2 \theta + k_A \sin \theta \cos \theta \left[1 + \left(1 - q_I^2 / k_A^2 - \frac{p_I^2}{k_A^2 \cos \theta} - 2 \frac{q_I}{k_A} \tan \theta \right)^{1/2} \right] \quad (3.1.5)$$

for the reflected magnetoacoustic wave. At this stage, our further analysis of the direct problem of ULF wave propagation through the geospace and lower atmosphere reduces to matching the solutions obtained for the wave field components and their derivatives at the interfaces separating the three media involved, i.e. at the lower ionospheric edge, $z = 0$, and at the Earth's surface, $z = h$. The boundary conditions to be met at the interfaces demand continuity of the tangential electric components both at $z = 0$ and $z = h$, and a jump-like discontinuity of the magnetic tangential components at the current-carrying sheet of the ionosphere, viz.

$$E_{x,y}(z = +0) = E_{x,y}(z = -0), \quad (3.1.6)$$

$$E_{x,y}(z = h + 0) = E_{x,y}(z = h - 0), \quad (3.1.7)$$

and

$$\begin{aligned} \frac{c}{4\pi} \Delta H_x &= \lim_{L \rightarrow 0} \int_{-L/2}^{L/2} j_y dz = \Sigma_p [E_y(0) \cdot (1 + \tan^2 \theta \sin^2 \psi) + E_x(0) \tan^2 \theta \sin \psi \cos \psi] + \\ &\quad + \Sigma_H E_x(0) / \cos \theta \\ \frac{c}{4\pi} \Delta H_y &= \lim_{L \rightarrow 0} \int_{-L/2}^{L/2} j_x dz = \Sigma_p [E_x(0) \cdot (1 + \tan^2 \theta \sin^2 \psi) + E_y(0) \tan^2 \theta \sin \psi \cos \psi] + \\ &\quad + \Sigma_H E_y(0) / \cos \theta \end{aligned} \quad (3.1.8)$$

Having written an explicit form of these equations with account of the incident angular spectrum (3.1.1) and of reflection laws like (3.1.4-3.1.5), we will be in a position to determine all the unknown constants in the field components at the Earth surface and in the upper ionosphere. In particular, the horizontal-plane magnetic components of the spatial harmonic (m, n) at the surface will be

$$H_x(x, y; z = h) = -\frac{e^{imx+iny}}{k_0 \nu} [mnB_x + (n^2 + \nu^2)B_y],$$

$$H_y(x, y; z = h) = \frac{e^{imx+iny}}{k_0 \nu} [(m^2 + \nu^2)B_x + mnB_y]$$
(3.1.9)

$$\text{with } \begin{aligned} B_x &= C_x(m, n)e^{i\chi h} + G_x(m, n)e^{-i\chi h}, \\ B_y &= C_y(m, n)e^{i\chi h} + G_y(m, n)e^{-i\chi h} \end{aligned}$$
(3.1.10)

$k_0 = \frac{\omega}{c}$; $\chi = (k_0^2 - m^2 - n^2)^{1/2}$ and $\nu = (k_0^2 \varepsilon_T - m^2 - n^2)^{1/2}$. $C_{x,y}$ and $G_{x,y}$ are just the constant

values to be expressed in terms of the incident amplitudes A_a, A_f and the respective wavenumbers (p, q) . Equations (3.1.2) to (3.1.10) provide the solution to the direct problem of wave propagation for a ULF disturbance arriving from the magnetosphere, in the sense that they permit calculating the spatial structure and polarization of the ULF field at an arbitrary observation point between 0 and 500 km above the Earth, proceeding from certain assumptions like (3.1.2) on the incident spatial spectrum. This solution will be used in Subsection 4.1 for interpreting the results of polarization measurements at ULF in Antarctica.

3.1.2 Nonlinear interaction of MHD waves with small-scale irregularities in the ionosphere

The presence in the ionosphere of electron density irregularities that can be regarded as sets of wavelike disturbances has been traditionally associated with nonlinear processes of energy exchange between wave modes of different spatial scales [Trakhtengertz and Feldstein, 1982; Gelberg, 1987]. In this Project a nonlinear interaction of MHD waves with small scale plasma irregularities in the ionosphere has been investigated. The shear Alfvén mode propagating through a plasma does not alter the density distribution of charged particles, however it can get involved in an interaction with ‘compressional’ modes of some kind which are capable of producing density variations. These would be modulated in the case by variation laws of the Alfvén wave parameters. A wave – wave interaction of any kind is only possible if the frequencies and wave vectors of the participating modes are matched so as to provide a spatial and temporal wave synchronism. In the case of lowest-order (quadratic in the wave amplitudes) nonlinear interaction the synchronism conditions are

$$\begin{aligned} \omega_1 &= \omega + \omega_2 \\ \vec{k}_1 &= \vec{k} + \vec{k}_2 \end{aligned}$$
(3.1.11)

which equations can be met by MHD modes belonging to either of the three spectral branches, namely the alfvénic (a), fast (f) and slow (s) magnetoacoustic [Aleksin and Khodusov, 1970;

1971; 1973]. In principle, we could be interested in analyzing the processes like $a_1 \leftrightarrow a + s_2$, $a_1 \leftrightarrow f + s_2$ or $a_1 \leftrightarrow s + s_2$. The former one, involving two transverse (shear Alfvén) waves and one longitudinal, or compressional mode, was considered earlier in the Annual Progress Report on this Project [Project P-072, 2002]. Meanwhile, by combining the synchronism conditions (3.1.11) with respective dispersion laws of the a , f and s modes, one can easily see that the nonlinear processes generating 'secondary' Alfvén or secondary fast modes cannot produce an essential difference of the wave frequency from that of the 'primary' Alfvén wave. On the other hand, the $a_1 \leftrightarrow s + s_2$ process, roughly speaking, represents frequency division of the primary wave in a 2:1 proportion, i.e. $\omega_1^a \approx 2\omega^s$. This situation seems to be conformant to the effects that were observed in a series of experiments on diagnosing natural and artificial turbulent structures in the ionosphere, synchronized with observations of Pc3-Pc4 geomagnetic pulsations [Ponomarenko et al, 2000; Yampolski, 1989]. With this in mind, we will consider the nonlinear interaction of an Alfvén wave with two slow magnetoacoustic waves in the F -region, on the assumption of a sufficiently strong thermal non-equilibrium there, $T_e \gg T_i$ ($T_{e,i}$ are respective kinetic temperatures of the electron and ion plasma components). Under these conditions the slow magnetoacoustic is a weakly damped wave. The interaction domain will be represented by a plane plasma layer parallel to the Earth surface and described in a Cartesian frame. To simplify the analysis, the tilt of the geomagnetic field vector will be neglected, such that the field direction and the local vertical will be along the z -axis. A powerful alfvénic wave, a_1 , generates a longitudinal wave (slow magnetic sound) in the plasma, which may give rise to density variations δn . An expression for δn can be derived from magnetic hydrodynamics equations combined with the Maxwell equations. The second-order variation in the plasma density reads as

$$\begin{aligned} \frac{\delta n^{(2)}(\omega, \vec{k})}{n_0} = & \frac{V_a^2}{B_0^2} \frac{1}{\omega^2 - V_s^2 k^2} \times \\ & \left\{ \int d\lambda \left(\vec{k} \cdot [\vec{H}_2, [\vec{k}_1, \vec{H}_1]] \right) + \int d\lambda \frac{V_a^2}{\omega_1 \omega_2} \left(\vec{k}_2 \cdot [\vec{h}_0, [\vec{k}_1, \vec{H}_1]] (\vec{k} \cdot [\vec{h}_0, [\vec{k}_2, \vec{H}_2]]) + \right. \right. \\ & \left. \left. + \int d\lambda \frac{V_a^2 V_s^2 (\vec{k} \vec{k}_2)}{\omega_1 \omega_2 (\omega_2^2 - V_s^2 k^2)} \left(\vec{k}_2 \cdot [\vec{h}_0, [\vec{k}_1, \vec{H}_1]] (\vec{k}_2 \cdot [\vec{h}_0, [\vec{k}_2, \vec{H}_2]]) \right) \right\}. \end{aligned} \quad (3.1.12)$$

The notation used in (3.1.12) is $d\lambda = d\vec{k}_1 d\vec{k}_2 d\omega_1 d\omega_2 \delta(\vec{k} - \vec{k}_1 + \vec{k}_2) \delta(\omega - \omega_1 + \omega_2)$; n_0 denotes

the equilibrium number density of charged particles; $V_s = \left(\gamma \frac{P}{n_0} \right)^{1/2}$ is the sound velocity in the

plasma; $V_a = \frac{B_0}{(4\pi m_i n_0)^{1/2}}$ the Alfvén velocity; B_0 the geomagnetic field magnitude at the observation point; \bar{H}_1 and \bar{H}_2 are Fourier components of the wave related magnetic field in the Alfvén and the magnetoacoustic wave, respectively (generally, $\bar{H}_i = \bar{H}(\omega_i, \vec{k}_i)$), and finally $\vec{h}_0 = \frac{\vec{B}_0}{B_0}$ is the unit vector along the geomagnetic field line. In the case of a low-pressure plasma ($\beta = \frac{8\pi P}{B_0^2} \ll 1$) dispersion laws of the modes considered take the form (with account of transverse dispersion of the magnetic sound) [Orayevsky, 1984]

$$\omega^a = |k_{\parallel}^a| V_a, \quad \omega^s = |k_{\parallel}^s| V_s \left(1 - \frac{k_{\perp}^2 V_s^2}{2 \Omega_i^2} \right). \quad (3.1.13)$$

Here k_{\parallel}^a and k_{\parallel}^s are field-aligned components of the wave vectors involved; k_{\perp} the transverse wave vector of the slow sound wave; $\Omega_i = \frac{eB_0}{m_i c}$ the ion gyrofrequency, and e the elemental charge. Assuming for simplicity a single Alfvén wave incident on the layer, i.e. $\bar{H}_1 = \bar{H}_1^0 \delta(\omega_1 - \omega_1^0) \delta(\vec{k}_1 - \vec{k}_1^0)$ we can find from (3.1.11) and (3.1.13) a tight connection between the incident frequency and wave vector on the one hand, and the respective parameters of the slow sound on the other. The field-aligned component k_{\parallel} of the magnetoacoustic wave vector becomes

$$k_{\parallel} = \frac{V_a k_{\parallel}^0}{2V_s} \left(1 - \frac{k_{\perp}^2 V_s^2}{2 \Omega_i^2} \right)^{-1}. \quad (3.1.14)$$

Actually, there will be two waves of this kind, whose wave vectors k_{\parallel} will point to nearly opposite directions. The respective frequencies are almost equal as well, and at the same time close to half the primary wave's frequency, $\omega \approx \omega_2 \approx \omega_1 / 2$. They will form a quasistatic array of plasma density variations, characterized by a fairly small period across the magnetic field. The cross-field scale size of the plasma fluctuations can be estimated from the magnitude of k_{\perp} at which the dispersion law of the sound waves becomes markedly different from the linear, viz.

$$k_{\perp} = \frac{\sqrt{\Omega_i^2 - k_{\parallel}^2 V_s^2}}{V_s}. \quad \text{The numerical values of } L_{\perp} \approx 2\pi k_{\perp}^{-1} \text{ in the } F\text{-region may vary, depending}$$

on the electron temperature, between 5 and 30 m. If the primary wave is powerful enough to allow neglecting the back action of other waves on its complex amplitude A_1^0 , then the set of

nonlinear equations governing the slow-varying Fourier amplitudes of the sound waves s and s_2 is

$$\begin{cases} \frac{\partial A_2(t)}{\partial t} - \gamma_s A_2(t) = -\alpha_s A_1^0 A^*(t) \\ \frac{\partial A(t)}{\partial t} - \gamma_s A(t) = -\alpha_s A_1^0 A_2^*(t) \end{cases} \quad (3.1.15)$$

The A_1^0 , A and A_2 here are the so called true amplitudes of the coupled waves which are related to their electric components as $\vec{E}(t)\vec{e}(k)e^{-|\gamma_s|t} = A(t)$ and $\vec{E}_2(t)\vec{e}(k_2)e^{-|\gamma_s|t} = A_2(t)$, with γ_s denoting the linear damping rate ($\gamma_s < 0$); $\vec{e}(\vec{k})$ and $\vec{e}(\vec{k}_2)$ being polarization vectors of the two slow magnetoacoustic modes, and α_s representing a coupling coefficient which is proportional to the matrix element S_{ijm} of the nonlinear Ohm law,

$$j_i(\omega, \vec{k}) = \sigma_{ij} E_j(\omega, \vec{k}) + \int S_{ijm} E_j(k') E_m(k - k') d\lambda + \dots \quad (3.1.16)$$

For the wave vectors like (3.1.14) that correspond to the former experimental conditions [Ponomarenko et al., 2000; Yampolski, 1989], α_s can be brought to the simple form

$$\alpha_s \approx \frac{c^2 m_i k_\perp \omega}{2B_0^2 e \cos^2 \theta_s} \left\{ \sin \delta - 2 \sin(\delta + \varphi) \operatorname{ctg} \varphi \frac{k_\parallel}{k_\perp} \right\}, \quad (3.1.17)$$

where φ denotes the angle made by the planes of \vec{k}_1^0 and \vec{k}_2 ; δ is the angle between the planes of \vec{k}_1^0 and \vec{k} , and θ_s is the angle between \vec{k} and the external magnetic field vector \vec{B}_0 . Note that $\frac{k_\parallel}{k_\perp} \ll 1$. We will seek a solution to (3.1.15) in the form corresponding to development of an instability, i.e. growth of the magnetosonic wave's amplitude at the expense of energy transfer from the primary Alfvén wave,

$$A(t) = A_s^0 \exp(\gamma_d t), \quad (3.1.18)$$

with $\gamma_d = \gamma_s \pm |\alpha_s| A_1^0 > 0$. The physical conditions for the instability can be determined from comparing α_s and γ_s . The linear damping rate of the slow magnetic sound is known to be [Mikhailovsky, 1976]

$$\gamma_s \approx - \left(\frac{\pi m_e}{8 m_i} \right)^{1/2} \frac{\omega_s^2}{|k_\parallel| V_{Te}}, \quad (3.1.19)$$

hence the condition for the instability is

$$E_1^0 \geq \left(\frac{\pi}{8}\right)^{1/2} \frac{2B_0^2 e m_e \cos^2 \theta_s}{c^2 m_i^2 k_{\perp} \sin \delta}. \quad (3.1.20)$$

Characteristic values of F -region MHD amplitudes (as given by the plasma drift velocities estimated through Doppler frequency shifts of diagnostic radar signals, [Sutcliffe and Poole, 1989; Sinitin et al., 1999]) are $E_1^0 \approx 400 \div 500 \mu \text{ V/m}$, or $\delta V = 8 \div 9.5 \text{ m/s}$. The right-hand side of (3.1.20), or the instability threshold can be estimated (with ionospheric plasma parameters for $h \approx 200 \div 500 \text{ km}$ and $\Omega_i \approx 2 \cdot 10^2 \text{ s}^{-1}$) as $E_{1thr}^0 \geq 8 \cdot 10^{-6} \text{ V/m}$ and $\delta V^{thr} \geq 1 \text{ m/s}$. We are now able to derive an estimate for the scale time of instability development. Setting in (3.17 to 3.20) $E_1^0 \sim 10^{-5} \text{ V/m}$; $k_{\perp} \sim 10^{-1} \text{ m}^{-1}$; $\sin \delta \sim 10^{-1}$, and $\cos^2 \theta_s \sim 10^{-4}$, we find $\alpha_s A_1^0 \sim 3 \cdot 10^{-2} \text{ s}^{-1}$. This is a

rate of development with which density fluctuations $\frac{\delta n^{(2)}}{n_0}$ may increase from the standard thermal level of $\sim 1\%$ to nearly 10% over 2 seconds. Hence, the nonlinear interaction between Alfvén waves and slow magnetosonic waves is capable of providing an efficient transfer of energy from large-scale MHD disturbances to the short-wave part of the spectrum and can be regarded as a probable mechanism of ionospheric turbulence generation in the high latitude ionosphere. This mechanism will be analyzed further in connection with the special, magnetic field dependent spread F effect observed at *Akademik Vernadsky* in 1996 through 2002 and discussed in Subsection 4.5 of this Report.

3.2 Magnetic polarization of ELF fields in the gyrotropic Earth-ionosphere cavity

A part of the Project Workplan related to theoretical analysis of the excitation, propagation and polarization of the ELF electromagnetic emissions of natural and technogenic origin existing in the Earth-ionosphere cavity. The investigation was aimed at developing a reliable theoretical model to support remote monitoring from *Akademik Vernadsky* of sources of the ELF radiation mentioned and properties of its propagation channel.

As is well known (see, e.g. Bliokh et al, 1982), the major natural source of ELF radiation is the global thunderstorm activity whose intense centers are located in equatorial areas of South-East Asia, Africa and South America. While thunderstorms are practically absent on the Antarctic continent, resonance properties of the Earth-ionosphere cavity provide for penetration there of the electromagnetic fields produced by remote lightning discharges from thousands of kilometers away. The level of electromagnetic fields is rather high at frequencies close to 8 Hz and higher-order harmonics. As for the anthropogenic ELF emissions arriving to Antarctica from other

regions of the globe, its probable sources are associated with the electric power lines of other continents operating at 50 Hz or 60 Hz. While external fields at 50 Hz or $(50 \times n)$ Hz are poorly distinguishable from the local emissions at *Vernadsky* generated by its power supply system, the fact of detecting harmonics of 60 Hz cannot be ascribed to anything else except emission from power lines of the American continent.

Some of the theoretical results have been presented in the Annual Progress Report (Year 1, 2002). In particular, the first Report concentrated on the excitation and propagation of individual spectral components of the ELF field, and formation of the observed polarization structure as a result of simultaneous activity of several incoherent sources of radiation. The calculations were done, based on an isotropic model of the Earth-ionosphere cavity, hence without account of geomagnetic field-controlled effects. Meanwhile, estimates show the East-West non-reciprocity of ELF wave propagation to have a potentially strong effect on the field polarization at an observation point. It is mainly for this reason that theoretical efforts were concentrated in 2003 on the study of geomagnetic field effects at ELF and development of a polarization model with allowance for ionospheric gyrotropy.

3.2.1 Gyrotropic model of electromagnetic wave propagation in the Schumann resonance range

Consider a geocentric spherical reference frame with the polar axis (Z) oriented toward geographic North (see Fig. 3.2.1). An observation point at the Earth's surface (at $r = a$) will be described by the angular coordinates $\{\theta; \varphi\}$. The world centers of thunderstorm activity lying in the equatorial belt will be considered to be compact (actually, point-sized) owing to their small extent compared with the wavelength Λ of the electromagnetic waves of interest. The center coordinates are $\{\theta_j = \pi/2; \varphi_j\}$ with $j = 1, 2, \dots, N$. The Earth will be assumed a perfectly conducting sphere while the sharp ionospheric boundary at $r = b$ a highly conducting gyrotropic surface whose electric properties are described by the tensorial surface impedance

$$\hat{Z} = \begin{vmatrix} Z_{\theta\theta} & Z_{\theta\varphi} \\ Z_{\varphi\theta} & Z_{\varphi\varphi} \end{vmatrix} \quad (3.2.1)$$

$$\tilde{P}_n^m(x) = \sqrt{\frac{(2n+1)(n-m)!}{2(n+m)!}} P_n^m(x), \quad (3.2.4)$$

and

$$P_n^m(0) = (-1)^{(n+m)/2} \sqrt{\frac{2}{\pi}} \frac{(n+m-1)!!}{(n+m)!} \delta_1(n+m); \quad (3.2.5)$$

with $\delta_1(k) = \begin{cases} 1, k = 2l \\ 0, k = 2l+1 \end{cases}$. Each term of the series (3.2.2) or (3.2.3) describes (at $m \neq 0$) a wave

which is standing along the θ coordinate and traveling along φ (either from West to East with $m < 0$, or from East to West with $m > 0$). Such waves are elliptically polarized at each point on the Earth's surface. The $m = 0$ waves are standing along both coordinates and the polarization is linear.

Further analysis will be done within the simple and convenient model of a d.c. geomagnetic field $\vec{H}^{(0)}$, known as "two halves of a hedgehog" [Bliokh et al, 1982]. In that model, the vector $\vec{H}^{(0)}$ is characterized by a single (radial) component whose magnitude is independent of the angular coordinates θ and φ , $|H_r^{(0)}| = \text{const}$, while the sign undergoes an abrupt change at the equator, $\text{sign} H_r^{(0)} = -\text{sign}(\cos\theta)$. Within this model $R_{nm}(\omega)$ takes the form [Bliokh et al, 1982; Nickolaenko et al, 2002]

$$R_{nm}(\omega) = R_{n0}(\omega) + \Delta R_{nm}(\omega), \quad (3.2.6)$$

$$R_{n0}(\omega) = \omega_n^2 - \omega^2 + \frac{i\omega c}{h} z_1, \quad (3.2.7)$$

and

$$\Delta R_{nm}(\omega) = \frac{2\omega c}{h} z_2 m \Pi_{nm} \delta_1(n+m), \quad (3.2.8)$$

with

$$\Pi_{nm} = \frac{2n+1}{2n(n+1)} \frac{(n+m-1)!!}{(n+m)!} \frac{(n-m-1)!!}{(n-m)!} = \Pi_{n|m|}. \quad (3.2.9)$$

Here

$$\omega_n = \frac{c}{a} \sqrt{n(n+1)} \quad (3.2.10)$$

is the n -th resonance frequency of a perfectly conducting Schumann cavity (i.e. $\sigma_{i,g} = \infty$),

$$z_0 = \sqrt{\frac{i\omega v_{eff}}{\omega_0^2}}, \quad z_1 = \frac{z_0}{\sqrt{2}} \sqrt{1 + \sqrt{1 + \rho^2}} \quad \text{and} \quad z_2 = \frac{z_0}{\sqrt{2}} \frac{\rho}{\sqrt{1 + \sqrt{1 + \rho^2}}} \quad (3.2.11)$$

are, respectively, the surface impedance of an isotropic ionosphere and the diagonal and off-diagonal matrix elements of the gyrotropic ionosphere impedance; $\rho = \omega_r / v_{eff}$ is the gyrotropic parameter; ω_r - the radial component of the electron gyrofrequency, and v_{eff} the effective collision frequency of electrons.

It is in this model that Nickolaenko et al, [2002] analyzed numerically the diurnal run of the ellipticity ratio at ELF in the Earth-ionosphere cavity. Spatial and temporal variations of thunderstorm intensity were derived from the motion of a single equatorial center making one full revolution around the Earth in 24 hours. The approach adopted in the present Project Report is different. Making use of the small parameters present in the problem, we attempted constructing a simplified analytical model for the polarization structure formation of the ELF noise excited by an arbitrary number of uncorrelated thunderstorm centers. Traditionally, one small parameter in the Schumann resonance theory is the isotropic surface impedance [Bliokh et al., 1980], whose magnitude is estimated as $|z_0| \sim 0.01$. The gyrotropic model involves another impedance related parameter, namely the ratio of diagonal to off-diagonal matrix elements. Within the “two halves of a hedgehog” model of the magnetic field the value takes the form

$$\gamma \equiv \frac{z_2}{z_1} = \frac{\rho}{1 + \sqrt{1 + \rho^2}}. \quad (3.2.12)$$

Quite evidently, the isotropic ($\rho = 0$) case corresponds to $\gamma = 0$, while the extremely high anisotropy ($\rho \rightarrow \infty$) to $\gamma = 1$. The magnitude is $\gamma < 1$ in all intermediate cases, and hence can be used as an expansion parameter for constructing some approximate solutions (for example, the reasonably realistic case $\rho \leq 1$ corresponds to $\gamma \leq 0.41$). Now we turn to analyzing equations (3.2.2) and (3.2.3) for the magnetic components of the ELF wave fields. As is known [Bliokh et al, 1980], each term n in the series assumes its maximum value at a frequency close to the corresponding Schumann resonance $\omega^{(n)}$, which latter is determined by the minimum of $|R_{n0}(\omega)|$. The m -dependence of the resonance condition appears from the effect of resonance splitting in the gyrotropic cavity [Bliokh et al, 1980]. However, the difference between $\omega^{(nm)}$ and $\omega^{(n)}$ is rather small and the cavity's Q -factor quite low, such that the splitting cannot be detected in measured spectra. For this reason the Schumann resonances are generally understood

as the cavity eigenfrequencies at $m = 0$, i.e. $\omega^{(n)}$. Linear expansions of (3.2.7) and (3.2.11) in the small impedance $|z_0|$ yield

$$\omega^{(n)} \approx \omega_n - \Omega, \quad (3.2.13)$$

and

$$\Omega = \frac{c|z_0|}{4h} = \frac{c|z_0|}{4h} \sqrt{1 + \sqrt{1 + \rho^2}}. \quad (3.2.14)$$

Substituting (3.2.12)-(3.2.14) into (3.2.7) and (3.2.8) we obtain the easily tractable formulas

$$R_{n0}(\omega) = (\omega^{(n)} - \omega)(\omega^{(n)} + \omega + 2\Omega) + 2i\omega\Omega, \quad (3.2.15)$$

and

$$\Delta R_{nm}(\omega) = 4\omega\Omega\beta(1+i)m\Pi_{nm}\delta_1(n+m), \quad (3.2.16)$$

where the estimate $m\Pi_{nm} < 1$ remains valid for all n and m (cf.3.2.9)).

To understand the behavior of $H_{j\theta}^g(\omega)$ and $H_{j\varphi}^g(\omega)$ at an arbitrary resonant frequency $\omega^{(p)}$, let us bring the field components to the form

$$H_{j\theta}^g(\omega^{(p)}) = \tilde{M}_j(\omega^{(p)}) e^{i\alpha x} \sum_{n=1}^{\infty} h_{j\theta}^{g(n)}(\omega^{(p)}), \quad (3.2.17)$$

$$H_{j\varphi}^g(\omega^{(p)}) = \tilde{M}_j(\omega^{(p)}) e^{i\alpha x} \sum_{n=1}^{\infty} h_{j\varphi}^{g(n)}(\omega^{(p)}). \quad (3.2.18)$$

The series terms,

$$h_{j\theta}^{g(n)}(\omega^{(p)}) \equiv \frac{c^2}{2\pi\alpha^3 h \sin \theta} \frac{d}{d\varphi} \sum_{m=-n}^n \frac{1}{R_{nm}(\omega^{(p)})} \tilde{P}_n^m(\cos \theta) \tilde{P}_n^m(0) e^{im(\varphi - \varphi_j)}, \quad (3.2.19)$$

$$h_{j\varphi}^{g(n)}(\omega^{(p)}) \equiv -\frac{c^2}{2\pi\alpha^3 h} \frac{d}{d\theta} \sum_{m=-n}^n \frac{1}{R_{nm}(\omega^{(p)})} \tilde{P}_n^m(\cos \theta) \tilde{P}_n^m(0) e^{im(\varphi - \varphi_j)}, \quad (3.2.20)$$

have the meaning of complex amplitudes of the resonance modes n which are excited in the cavity by the current moment \tilde{M}_j of unit intensity, $\tilde{M}_j = 1$. They show a sharply different behavior with $n = p$ and $n \neq p$. In the resonant case $n = p$, equations (3.2.15) and (3.2.16) become

$$R_{p0}(\omega^{(p)}) = 2i\omega^{(p)}\omega\Omega, \quad (3.2.21)$$

$$\Delta R_{pm}(\omega^{(p)}) = 4\omega^{(p)}\Omega\beta(1+i)m\Pi_{pm}\delta_1(p+m), \quad (3.2.22)$$

such that the “frequency response” functions $[R_{pm}(\omega)]^{-1}$ can be written (to terms linear in γ) as

$$\frac{1}{R_{pm}(\omega^{(p)})} \approx -i \frac{1 - m\Delta\varphi_{pm}}{2\omega^{(p)}\Omega} \exp\{im\Delta\varphi_{pm}\}, \quad (3.2.23)$$

and

$$\Delta\varphi_{pm} \equiv 2\gamma\Pi_{pm}\delta_1(p+m). \quad (3.2.24)$$

Note that the presence of $\delta_1(p+m)$ in (3.2.24) does not impose additional limitations on the solution because of equatorial location of the thunderstorm centers. The Earth-ionosphere cavity can be excited only in those modes which correspond to $\delta_1(p+m)=1$ (see (3.2.5)). Now the mode amplitudes (3.2.19-3.2.20) can be re-written as

$$h_{j\theta}^{g(p)}(\omega^{(p)}) \equiv \frac{-ic^2}{4\pi\alpha^3 h\omega^{(p)}\Omega \sin\theta} \frac{d}{d\varphi} \sum_{m=-p}^p \left(1 + i\Delta\varphi_{pm} \frac{d}{d\varphi}\right) \tilde{P}_p^m(\cos\theta) \tilde{P}_p^m(0) e^{im[\varphi - (\varphi_j - \Delta\varphi_{pm})]}, \quad (3.2.25)$$

$$h_{j\varphi}^{g(p)}(\omega^{(p)}) \equiv \frac{ic^2}{4\pi\alpha^3 h\omega^{(p)}\Omega} \frac{d}{d\theta} \sum_{m=-p}^p \left(1 + i\Delta\varphi_{pm} \frac{d}{d\varphi}\right) \tilde{P}_p^m(\cos\theta) \tilde{P}_p^m(0) e^{im[\varphi - (\varphi_j - \Delta\varphi_{pm})]}. \quad (3.2.26)$$

The effect of gyrotropy is to bring a small imaginary correction into the amplitude factor and a phase shift which is perceived as a longitudinal westwardly displacement of the radiation source, independent of its position relative to the point of observation. To be able to make further simplifications, let us analyze the dependences of $\Delta\varphi_{pm}$ on the values assumed by p and m . Since $\Pi_{pm} = \Pi_{p|m|}$ (see 3.2.9), only absolute magnitudes of m will be considered. The formulas below are specific values of $\Delta\varphi$ for $p=1,2,3,4$ and 5 and such $|m|$'s which are permitted by the condition (3.2.5), viz.

$$\begin{array}{lll} 1) \ p=1 \rightarrow |m|=1 & 2) \ p=2 \rightarrow |m|=2 & 3) \ p=3 \rightarrow |m|=1,3 \\ \Delta\varphi_{11} = 0,75\gamma; & \Delta\varphi_{22} = 0,31\gamma; & \Delta\varphi_{31} = 0,11\gamma; \ \Delta\varphi_{33} = 0,18\gamma; \end{array}$$

$$\begin{array}{ll} 4) \ p=4 \rightarrow |m|=2,4 & 5) \ p=5 \rightarrow |m|=1,3,5 \\ \Delta\varphi_{42} = 0,07\gamma; \ \Delta\varphi_{44} = 0,12\gamma; & \Delta\varphi_{51} = 0,04\gamma; \ \Delta\varphi_{53} = 0,05\gamma; \ \Delta\varphi_{55} = 0,09\gamma. \end{array}$$

As is easy to see, the phase shift $\Delta\varphi_{pm}$ is greatest for the two first resonances, $\omega^{(1)}$ and $\omega^{(2)}$, and decreases for higher orders p of the Schumann resonance. Starting with $p=3$, the estimate is valid $(\Delta\varphi_{pm}/\Delta\varphi_{11})_{p \geq 3} \leq (\Delta\varphi_{pp}/\Delta\varphi_{11})_{p \geq 3} \leq 0,18 \ll 1$. This gives us the right to use an additional simplification by the substitution

$$\Delta\varphi_{pm} \rightarrow \Delta\varphi^{(p)} \equiv (\max \Delta\varphi_{pm} - \min \Delta\varphi_{pm})/2. \quad (3.2.27)$$

Apparently, this does not affect the numerical accuracy at $\omega = \omega^{(1)}$ and $\omega = \omega^{(2)}$ where gyrotropic effects are strongest. Whereas at higher order harmonics $\omega^{(p)}$ where these effects are only slightly manifested, the approximation provides a qualitative description. By employing the substitution (3.2.27), we are able to factor $\Delta\varphi^{(p)}$ out from the m -sums in (3.2.25) and (3.2.26), and hence to apply the familiar addition theorem for the Legendre functions [Erdelyi, 1953]:

$$P_p(\cos \vartheta_j) = \sum_{m=-p}^p \frac{(p-m)!}{(p+m)!} P_p^m(\cos \theta) P_p^m(\cos \theta_j) e^{im(\varphi - \varphi_j)}. \quad (3.2.28)$$

Here ϑ_j is the angular separation between $\{\theta_j; \varphi_j\}$ and $\{\theta; \varphi\}$ along the spherical surface (see Fig.3.2.1) which is given by

$$\cos \vartheta_j = \cos \theta \cos \theta_j + \sin \theta \sin \theta_j \cos(\varphi - \varphi_j). \quad (3.2.29)$$

The summation can be brought to the form

$$h_{j\theta}^{g(p)}(\omega^{(p)}) \equiv \frac{-ic^2(p+1/2)}{4\pi a^3 h \omega^{(p)} \Omega \sin \theta} \frac{\partial}{\partial \varphi} \left\{ P_p(\cos \hat{\vartheta}_j^{(p)}) + i \Delta\varphi^{(p)} \frac{\partial}{\partial \varphi} P_p(\cos \vartheta_j) \right\}, \quad (3.2.30)$$

$$h_{j\varphi}^{g(p)}(\omega^{(p)}) \equiv \frac{ic^2(p+1/2)}{4\pi a^3 h \omega^{(p)} \Omega} \frac{\partial}{\partial \theta} \left\{ P_p(\cos \hat{\vartheta}_j^{(p)}) + i \Delta\varphi^{(p)} \frac{\partial}{\partial \varphi} P_p(\cos \vartheta_j) \right\}, \quad (3.2.31)$$

with $\hat{\vartheta}_j^{(p)}$ having the meaning of an 'apparent' angular separation in the gyrotropic cavity which differs from ϑ_j in the respect that the longitude φ_j of the radiating center has been replaced by $\hat{\varphi}_j^{(p)} \equiv \varphi_j - \Delta\varphi^{(p)}$. As for other terms of the equations involving $\Delta\varphi^{(p)}$ as a factor, the difference between $\hat{\vartheta}_j^{(p)}$ and ϑ_j results there in corrections of order $\sim [\Delta\varphi^{(p)}]^2 \sim \gamma^2$, and hence is not taken into account.

Now we turn to analyzing field components of frequency $\omega^{(p)}$ in the non-resonant case $n \neq p$. According to (3.2.15) and (3.2.16), the correction term $\Delta R_{nm}(\omega^{(p)})$ is a small value of second order in γ and $\Omega/\omega^{(n,p)} \sim |z_0|$ with respect to $\Delta R_{nm}(\omega^{(p)})$. Within the linear approximation that we have adopted it should be neglected. Then the frequency response function $[R_{nm}(\omega^{(p)})]^{-1} \approx [R_{n0}(\omega^{(p)})]^{-1}$ can be factored out of the summation sign in (3.2.19) and (3.2.20), while the respective series will be summed according to (3.2.28). The result is

$$h_{j\theta}^{g(n)}(\omega^{(p)}) \equiv \frac{c^2(n+1/2)}{2\pi\alpha^3 h(\omega^{(n)2} - \omega^{(p)2})} \frac{1}{\sin\theta} \frac{d}{d\varphi} P_n(\cos\vartheta_j), \quad (3.2.32)$$

$$h_{j\varphi}^{g(n)}(\omega^{(p)}) \equiv -\frac{c^2(n+1/2)}{2\pi\alpha^3 h(\omega^{(n)2} - \omega^{(p)2})} \frac{d}{d\theta} P_n(\cos\vartheta_j). \quad (3.2.33)$$

At this point we are able to construct full equations for the magnetic field components by performing summation over n of all the terms in the zonal harmonic series, both resonant and non-resonant,

$$h_{j\theta}^g(\omega^{(p)}) \equiv \sum_{n=1}^{\infty} h_{j\theta}^{g(n)}(\omega^{(p)}) = \frac{c^2(p+1/2)}{4\pi\alpha^3 h\omega^{(p)}\Omega \sin\theta} \left\{ -i \frac{\partial}{\partial\varphi} P_p(\cos\hat{\vartheta}_j^{(p)}) + \right. \\ \left. + \Delta\varphi^{(p)} \frac{\partial^2}{\partial\varphi^2} P_p(\cos\vartheta_j) + 2 \sum_{n \neq p} \frac{(n+1/2)}{(p+1/2)} \frac{\omega^{(p)}\Omega}{(\omega^{(n)2} - \omega^{(p)2})} \frac{d}{d\varphi} P_n(\cos\vartheta_j) \right\}, \quad (3.2.34)$$

$$h_{j\varphi}^g(\omega^{(p)}) \equiv \sum_{n=1}^{\infty} h_{j\varphi}^{g(n)}(\omega^{(p)}) = \frac{c^2(p+1/2)}{4\pi\alpha^3 h\omega^{(p)}\Omega} \left\{ i \frac{\partial}{\partial\theta} P_p(\cos\hat{\vartheta}_j^{(p)}) + \right. \\ \left. - \Delta\varphi^{(p)} \frac{\partial^2}{\partial\theta\partial\varphi} P_p(\cos\vartheta_j) - 2 \sum_{n \neq p} \frac{(n+1/2)}{(p+1/2)} \frac{\omega^{(p)}\Omega}{(\omega^{(n)2} - \omega^{(p)2})} \frac{d}{d\theta} P_n(\cos\vartheta_j) \right\}. \quad (3.2.35)$$

The limiting transition to the ionospheric case, $\rho = 0$, implies $\Delta\varphi^{(p)} = 0$ and $\hat{\vartheta}_j^{(p)} = \vartheta_j$. With this in mind, it is easy to see that the resonance term $n = p$ of the zonal harmonic series for an arbitrary Schumann frequency $\omega^{(p)}$ is purely imaginary in the isotropic case, while non-resonance terms $n \neq p$ are real magnitudes of first order of smallness in $\Omega/\omega^{(n,p)} \sim |z_0|$ compared with the resonance term. The field polarization is linear for all values of n .

Within the first-order approximation in γ and $|z_0|$ the d.c. geomagnetic field cannot alter the form of non-resonance terms in the series, just bringing forth replacement of the isotropic impedance z_0 by the z_1 component of the matrix impedance. As for the resonance term, the effect of gyrotropy there manifests itself through the apparent shift of source center coordinates in isotropic formulas and appearance of a correction term shifted in phase by $\pi/2$. Owing to the latter correction, the resonant field term becomes elliptically polarized. Making account of these changes, (3.2.34 – 3.2.35) can be brought to the form

$$h_{j\theta}^g(\omega^{(p)}) = i \left[\text{Im} h_j^i(\omega^{(p)}, \hat{\vartheta}_j^p, z_1) \sin \hat{\alpha}_j^{(p)} \right] + \\ + \left\{ \left[\text{Re} h_j^i(\omega^{(p)}, \vartheta_j, z_1) \sin \alpha_j \right] - \Delta\varphi^{(p)} \frac{\partial}{\partial\varphi} \left[\text{Im} h_j^i(\omega^{(p)}, \vartheta_j, z_1) \sin \alpha_j \right] \right\}, \quad (3.2.36)$$

$$h_{j\varphi}^s(\omega^{(p)}) = i \left[\text{Im} h_j^i(\omega^{(p)}, \hat{\vartheta}_j^{(p)}, z_1) \cos \hat{\alpha}_j^{(p)} \right] + \\ + \left\{ \left[\text{Re} h_j^i(\omega^{(p)}, \vartheta_j, z_1) \cos \alpha_j \right] - \Delta \varphi^{(p)} \frac{\partial}{\partial \varphi} \left[\text{Im} h_j^i(\omega^{(p)}, \vartheta_j, z_1) \cos \alpha_j \right] \right\}, \quad (3.2.37)$$

where $h_j^i(\omega^{(p)}, \vartheta_j, z_1)$ denotes the complex amplitude of the horizontal magnetic field component at the angular distance ϑ_j from the source in an isotropic cavity with an ionospheric impedance z_1 ; $-\pi/2 \leq \alpha_j \leq \pi/2$ is the direction toward the source of radiation, which is counted from geographic North (positive angles are counted in the clockwise direction) – see Fig.3.2.1);

$$\text{Im} h_j^i(\omega^{(p)}, \vartheta_j, z_1) = \frac{c^2(p+1/2)}{4\pi a^3 h \omega^{(p)} \Omega} \frac{\partial}{\partial \vartheta_j} P_p(\cos \vartheta_j), \quad (3.2.38)$$

$$|\text{Re} h_j^i(\omega^{(p)}, \vartheta_j, z_1) / \text{Im} h_j^i(\omega^{(p)}, \vartheta_j, z_1)| \sim |z_0| \ll 1;$$

with

$$\sin \alpha_j = -\frac{\sin(\varphi - \varphi_j)}{\sin \vartheta_j}, \quad \cos \alpha_j = -\frac{\cos \theta \cos(\varphi - \varphi_j)}{\sin \vartheta_j}, \quad (3.2.39)$$

$$\cos \vartheta_j = \sin \theta \cos(\varphi - \varphi_j),$$

Equation (3.2.38) depends on z_1 via $\Omega = c|z_1|/(4h)$. The ‘apparent’ direction angles, $\hat{\alpha}_j^{(p)} \equiv \alpha_j + \Delta \alpha_j^{(p)}$, and angular distances, $\hat{\vartheta}_j^{(p)} \equiv \vartheta_j + \Delta \vartheta_j^{(p)}$ are given by the same equations (3.2.39) where the source center longitude φ_j must be replaced by the ‘shifted’ magnitude $\hat{\varphi}_j^{(p)}$. The formation of “apparent” distances and directions in the gyrotropic cavity is illustrated by Fig.3.2.2, a and 3.2.2, b (the a) figure corresponds to a Southern hemisphere location of the observation site, ($\cos \theta < 0$), while in b) the observer is in the Northern hemisphere, ($\cos \theta > 0$)).

The formulas (3.2.36) and (3.2.39) presented allow expressing the ELF fields of the gyrotropic Earth-ionosphere cavity (at Schumann resonance frequencies) via the corresponding fields of the isotropic cavity. The representation is valid within the first order in the parameters γ and $|z_0|$. The physical properties and computation methodology of the isotropic cavity fields are well known [cf. Bloikh et al., 1980].

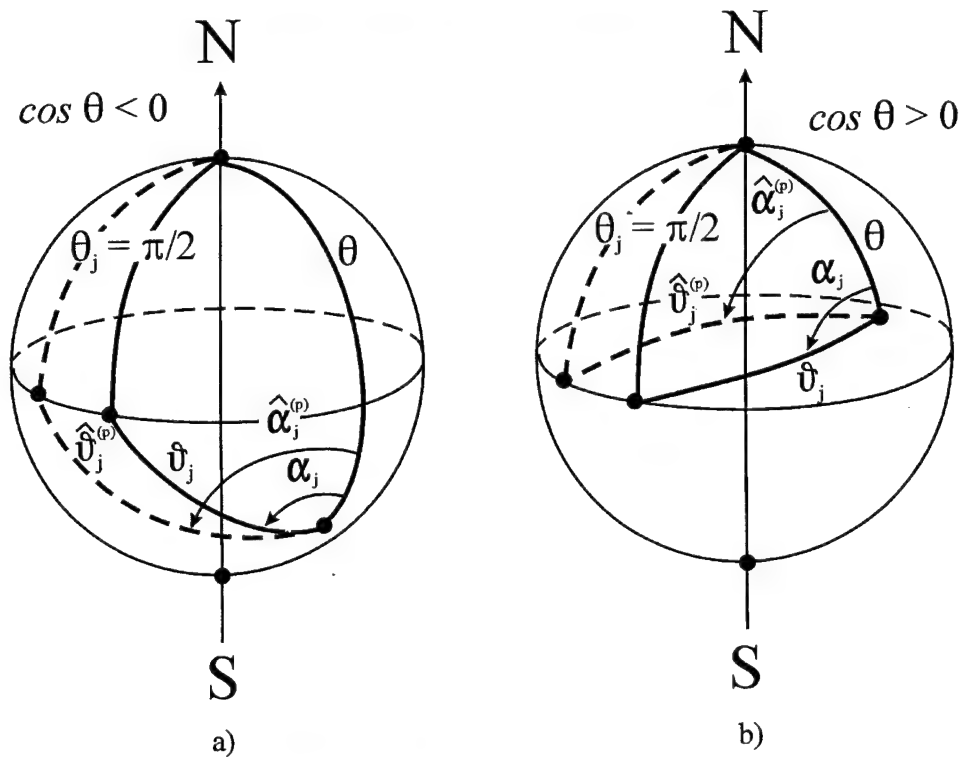


Fig. 3.2.2 Formation of 'apparent' direction angles and distances in the gyrotropic Earth-ionosphere cavity: a) $\cos \theta < 0$, Southern hemisphere ;
b) $\cos \theta > 0$, Northern hemisphere.

3.2.2 Polarization of Schumann resonances in the gyrotropic Earth-ionosphere cavity

As shown in the Annual Progress Report, [Project P-072, 2002], the ELF electromagnetic fields excited in the Earth-ionosphere cavity by individual thunderstorm centers are mutually incoherent. Hence, polarization properties of the net field can be analyzed conveniently in terms of the Stokes parameters. A Stokes parameter relating to the total field from a few centers is an incoherent sum of the like parameters for each of the centers. The isotropic cavity model was used in the Annual Report to analyze formulation of the resultant polarization from an arbitrary set of linearly polarized partial radiating centers. We will consider here the modifications arising from the gyrotropy of the Earth-ionosphere cavity.

a) *Polarization properties of ELF fields from an isolated thunderstorm center.* Following the Annual Report [Project P-072, 2002], let us introduce a local Cartesian frame with the X -axis pointing toward the geographic North, Y toward the East and Z vertically down. The orthogonal magnetic components of the ELF field in this frame and in the geocentric polar spherical system above are related as

$$H_{jx} = -H_{j\theta}, \text{ and } H_{jy} = H_{j\varphi}. \quad (3.2.40)$$

As follows from (3.2.17), (3.2.18) and (3.2.36 to 3.2.40), Stokes parameters of the radiation from an isolated thunderstorm center j in the gyrotropic cavity obey the relations (to first order in γ and $|z_0|$)

$$\begin{aligned} I_j^g(\omega^{(p)}) &\equiv \langle |H_{jx}^g(\omega^{(p)})|^2 \rangle + \langle |H_{jy}^g(\omega^{(p)})|^2 \rangle \approx \\ &\approx \langle |\tilde{M}_j(\omega^{(p)})|^2 \rangle |h_j^i(\omega^{(p)}, \hat{\mathcal{G}}_j^{(p)}, z_1)|^2, \end{aligned} \quad (3.2.41)$$

$$\begin{aligned} Q_j^g(\omega^{(p)}) &\equiv \langle |H_{jx}^g(\omega^{(p)})|^2 \rangle - \langle |H_{jy}^g(\omega^{(p)})|^2 \rangle \approx \\ &\approx -\langle |\tilde{M}_j(\omega^{(p)})|^2 \rangle |h_j^i(\omega^{(p)}, \hat{\mathcal{G}}_j^{(p)}, z_1)|^2 \cos(2\hat{\alpha}_j^{(p)}) = \\ &= \langle |\tilde{M}_j(\omega^{(p)})|^2 \rangle |h_j^i(\omega^{(p)}, \hat{\mathcal{G}}_j^{(p)}, z_1)|^2 \cos(2\hat{\beta}_j^{(p)}), \end{aligned} \quad (3.2.42)$$

$$\begin{aligned} U_j^g(\omega^{(p)}) &= 2 \operatorname{Re} \langle H_{jx}^g(\omega^{(p)}) H_{jy}^{g*}(\omega^{(p)}) \rangle \approx \\ &\approx -\langle |\tilde{M}_j(\omega^{(p)})|^2 \rangle |h_j^i(\omega^{(p)}, \hat{\mathcal{G}}_j^{(p)}, z_1)|^2 \sin(2\hat{\alpha}_j^{(p)}) = \\ &= \langle |\tilde{M}_j(\omega^{(p)})|^2 \rangle |h_j^i(\omega^{(p)}, \hat{\mathcal{G}}_j^{(p)}, z_1)|^2 \sin(2\hat{\beta}_j^{(p)}), \end{aligned} \quad (3.2.43)$$

$$\begin{aligned} V_j^g(\omega^{(p)}) &= 2 \operatorname{Im} \langle H_{jx}^g(\omega^{(p)}) H_{jy}^{g*}(\omega^{(p)}) \rangle = \\ &= -2\Delta\varphi^{(p)} \langle |\tilde{M}_j(\omega^{(p)})|^2 \rangle \frac{\cos\theta}{\sin^2 \mathcal{G}_j} |h_j^i(\omega^{(p)}, \mathcal{G}_j, z_1)|^2. \end{aligned} \quad (3.2.44)$$

Here $\hat{\beta}_j^{(p)} \equiv \hat{\alpha}_j^{(p)} - (\pi/2) \operatorname{sign}(\hat{\alpha}_j^{(p)})$ is the angle between the X -axis and the ‘apparent’ direction $\hat{\alpha}_j^{(p)}$ (see Fig.3.2.3); $\hat{\beta}_j^{(p)}$ lies between $\pm \pi/2$, i.e. $-\pi/2 \leq \hat{\beta}_j^{(p)} \leq \pi/2$, with positive values counted in the clockwise direction; the angular brackets $\langle \dots \rangle$ denote statistical averaging. The ‘apparent’ direction toward the thunderstorm center and its normal are shown with dashed lines.

It has been taken into account in (3.2.41) to (3.2.42) that the equation holds $|h_j^i(\omega^{(p)}, \mathcal{G}_j, z_1)|^2 \approx [\operatorname{Im} h_j^i(\omega^{(p)}, \mathcal{G}_j, z_1)]^2$ in the linear approximation with respect to $|z_0|$. Positive values of $V_j^g(\omega^{(p)})$ in (3.2.44) correspond to such phase differences $(\delta_x - \delta_y) > 0$ of the orthogonal magnetic field components which lead to a clockwise rotation of the vector \vec{H}_j^g in the horizontal plane with the factor $\exp(i\omega t)$ that has been selected.

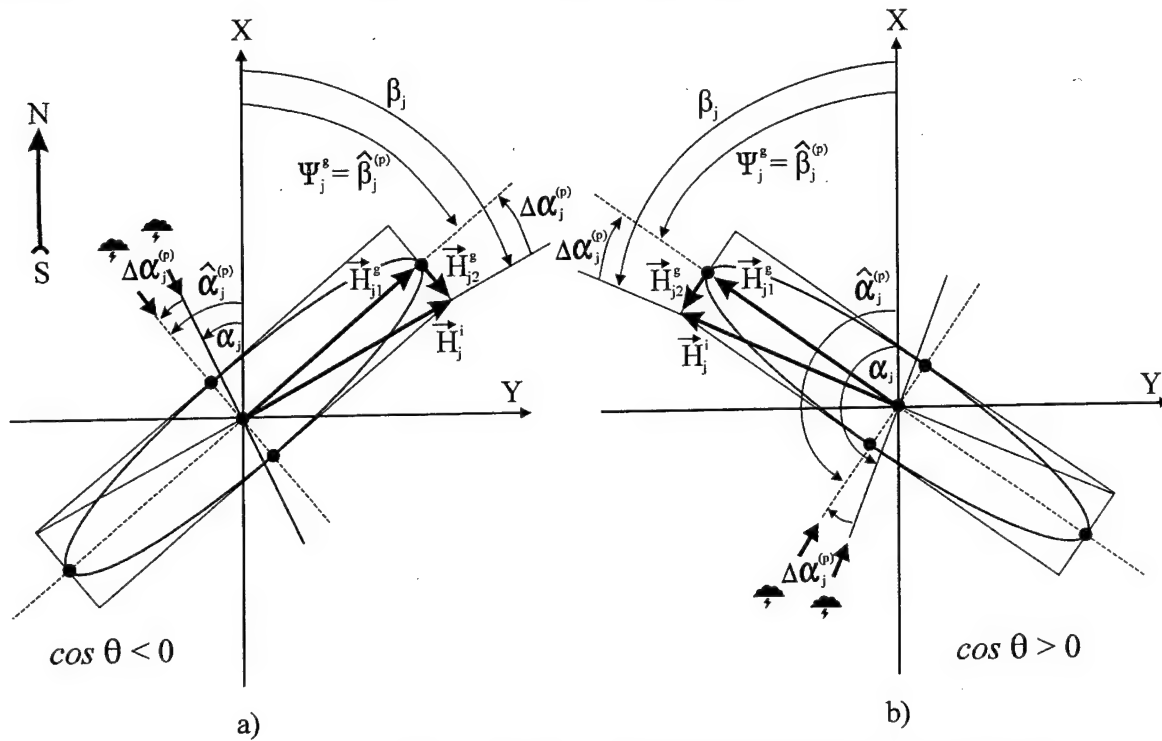


Fig.3.2.3. Formation of elliptic polarization in the gyrotropic Earth-ionosphere cavity:

- a) Southern hemisphere ($\cos \theta < 0$);
- b) Northern hemisphere ($\cos \theta > 0$).

Comparing the Stokes parameters I_j^g, Q_j^g and U_j^g that have been found with their isotropic analogs, I_j^i, Q_j^i , and U_j^i , given in the Annual Project Report [Project P-072, 2002], one can see the corresponding values to coincide upon substitution $\alpha_j \Leftrightarrow \hat{\alpha}_j^{(p)}$ and $\vartheta_j \Leftrightarrow \hat{\vartheta}_j^{(p)}$. As for the Stokes parameter V_j^g , its difference from the zero value of the isotropic case, $V_j^i = 0$, is evidence for the elliptic character of ELF polarization in the gyrotropic cavity.

The polarization characteristics of ELF fields from a single thunderstorm center can be written, after (3.2.41) to (3.2.44), as

- 1) r_j^g , the ellipticity ratio

$$r_j^g(\omega^{(p)}) \equiv \frac{V_j^g}{\sqrt{(Q_j^g)^2 + (U_j^g)^2 + (V_j^g)^2} + \sqrt{(Q_j^g)^2 + (U_j^g)^2}} \approx \frac{V_j^g}{2\sqrt{(Q_j^g)^2 + (U_j^g)^2}} = -\Delta\varphi^{(p)} \frac{\cos \theta}{\sin^2 \vartheta_j} \approx -\Delta\alpha_j^{(p)}; \quad (3.2.45)$$

- 2) $\Psi_j^g(\omega^{(p)})$, the orientation angle

$$\cos[2\Psi_j^g(\omega^{(p)})] \equiv \frac{Q_j^g}{\sqrt{(Q_j^g)^2 + (U_j^g)^2}} \approx \cos[2\hat{\beta}_j^{(p)}]$$

or

$$\Psi_j^g(\omega^{(p)}) \approx \hat{\beta}_j^{(p)} = \beta_j + \Delta\alpha_j^{(p)}, \quad (3.2.46)$$

where $\beta_j \equiv \alpha_j - (\pi/2)\text{sign}(\alpha_j)$ is the orientation angle of the linearly polarized magnetic field vector \vec{H}_j^i of the isotropic cavity (see Fig.3.2.3);

3) $P_j^g(\omega^{(p)})$, degree of polarization:

$$P_j^g(\omega^{(p)}) \equiv \frac{I_j^{g(pol)}}{I_j^g} \equiv \frac{\sqrt{(Q_j^g)^2 + (U_j^g)^2 + (V_j^g)^2}}{I_j^g} \approx \frac{\sqrt{(Q_j^g)^2 + (U_j^g)^2}}{I_j^g} = 1, \quad (3.2.47)$$

where $I_j^{g(pol)} \equiv \sqrt{(Q_j^g)^2 + (U_j^g)^2 + (V_j^g)^2}$ is the intensity of the polarized component. Equations (3.2.45) to (3.2.47) imply that the radiation of each individual center of thunderstorm activity at every Schumann resonance frequency $\omega^{(p)}$ is fully polarized. Within the selected model of the geomagnetic field it is characterized by the same sense of \vec{H}_j^g rotation in the horizontal plane (specifically, $r_j^g > 0$, or clockwise rotation should be observed in the Southern hemisphere, and $r_j^g < 0$, or counter-clockwise rotation in the Northern hemisphere). Numerical values of the ellipticity ratio and shift of the ellipse orientation angle, $\Delta\alpha_j^{(p)}$, from the β_j direction are maximal at the frequency $\omega^{(1)}$ of the first Schumann resonance and decrease monotonously as the resonance order p increases.

The analysis presented permits formulating a rather simple geometric model for the formation of the ELF polarization structure in the gyrotropic cavity. The basic ideas are as follows.

1. The geomagnetic field in the Earth-ionosphere cavity brings forth changes in the amplitude and phase structure of the ELF fields at resonance frequencies $\omega^{(p)}$ (compared with the isotropic case) which can be taken in to account within equations of the isotropic model by a westward shift of all the world thunderstorm centers (sources of radiation) by the same angle $\Delta\varphi^{(p)}$. The shift is maximal for $p=1$ and diminishes quite rapidly as the number is increased. The effect is sensed by an observer at an arbitrary point on the globe as a change of the angle of arrival for the radiation coming from center j , $\Delta\alpha_j^{(p)} \approx \Delta\varphi^{(p)}(\cos\theta/\sin^2\vartheta_j)$. Rather naturally, it may be given the name of *ELF refraction in the gyrotropic Earth-ionosphere cavity*. In

contrast to the phase shift $\Delta\varphi^{(p)}$, the 'refraction angle' $\Delta\alpha_j^{(p)}$, is essentially dependent on the observation point latitude, θ , and its separation ϑ_j from the thunderstorm center j . In particular, $\Delta\alpha_j^{(p)}$ changes sign when the observer crosses the equator, being positive in the Northern hemisphere and negative in the South.

2. Because of the 'refraction' described, a linearly polarized resonance field of the isotropic cavity becomes elliptically polarized in the gyrotropic resonator. The 'isotropic' field vector \vec{H}_j^i lying at the angle β_j to the X -axis breaks down into two orthogonal 'gyrotropic' vectors (see Fig. 3.2.3) of which \vec{H}_{j1}^g is in phase with \vec{H}_j^i , while \vec{H}_{j2}^g lags behind by $\pi/2$. The two vectors are oriented, respectively, across and along the 'apparent' direction $\hat{\alpha}_j^{(p)}$ of wave arrival. The absolute magnitudes of these vectors determine the major and minor semiaxis lengths of the polarization ellipse, while their spatial orientation controls the orientation angle $\beta_j^g = \hat{\beta}_j^{(p)}$ of the major axis and the sense of rotation of the \vec{H}_j^g vector end at the upper point of the ellipse. The formation of the clockwise (counter-clockwise) elliptic polarization in the Southern (Northern) hemisphere is shown in Fig. 3.2.3, a (b).

b) *Polarization characteristics of the Schumann resonance field excited by the global thunderstorms.* As noted heretofore, the Stokes parameters of the fields from all available centers of thunderstorm activity can be expressed as incoherent sums of respective Stokes parameters for the contributions from each of the centers. This behavior was analyzed for the isotropic Earth-ionosphere cavity in the Annual Progress Report [Project P-072, 2002]. The 'gyrotropic' degree of polarization, P^g , and orientation angle β_j^g of the polarization ellipse can be obtained from the 'isotropic' formulas of [P-072, 2002] by replacing $\hat{\beta}_j^{(p)}$ for β_j , viz.

$$P^g(\omega^{(p)}, t) = \frac{\sqrt{\sum_{j,k} \langle |\tilde{M}_j(t)|^2 \rangle \langle |\tilde{M}_k(t)|^2 \rangle \hat{h}_j^i(\omega^{(p)})^2 \hat{h}_k^i(\omega^{(p)})^2 \cos[2(\hat{\beta}_j^{(p)} - \hat{\beta}_k^{(p)})]}}{\sum_j \langle |\tilde{M}_j(t)|^2 \rangle \hat{h}_j^i(\omega^{(p)})^2}, \quad (3.2.48)$$

$$\begin{aligned} |\Psi^g(\omega^{(p)}, t)| &= \\ &= \frac{1}{2} \arccos \left\{ \frac{\sum_j \langle |\tilde{M}_j(t)|^2 \rangle \hat{h}_j^i(\omega^{(p)})^2 \cos(2\hat{\beta}_j^{(p)})}{\sqrt{\sum_{j,k} \langle |\tilde{M}_j(t)|^2 \rangle \langle |\tilde{M}_k(t)|^2 \rangle \hat{h}_j^i(\omega^{(p)})^2 \hat{h}_k^i(\omega^{(p)})^2 \cos[2(\hat{\beta}_j^{(p)} - \hat{\beta}_k^{(p)})]}} \right\}, \end{aligned} \quad (3.2.49)$$

with

$$\text{sign}[\Psi^g(\omega^{(p)}, t)] = \text{sign}\left\{\sum_j \left\langle |\tilde{M}_j(t)|^2 \right\rangle \left| \hat{h}_j'(\omega^{(p)}) \right|^2 \sin(2\hat{\beta}_j^{(p)}) \right\}. \quad (3.2.50)$$

Use has been made of the approximate equation $\left\langle |\tilde{M}_j| \right\rangle^2 \approx \text{const}(\omega)$ (see [P-072, 2002]) and the abbreviation $\left| \hat{h}_j'(\omega^{(p)}) \right|^2 \equiv \left| h_j'(\omega^{(p)}, \hat{\vartheta}_j^p, z_1) \right|^2$. The isotropic cavity field at a resonant frequency $\omega^{(p)}$ is evaluated from

$$\left| h_j'(\omega^{(p)}, \vartheta_j, z_1) \right|^2 \approx \left[\frac{c^2(p+1/2)\sin \vartheta_j}{4\pi\alpha^3 h \omega^{(p)} \Omega} P_p'(\cos \vartheta_j) \right]^2, \text{ where } P_p'(x) \equiv \frac{dP(x)}{dx} \quad (3.2.51)$$

The argument t denotes a parametric dependence on universal time.

What regards the ellipticity ratio r^g , (which is equal to zero in the isotropic model), it can be expressed as

$$\begin{aligned} r^g(\omega^{(p)}, t) &\approx \frac{\sum_j V_j^g}{2 \sqrt{(\sum_j Q_j^g)^2 + (\sum_j U_j^g)^2}} = \\ &= \frac{-\Delta\varphi^{(p)} \cos \theta \sum_j \left\langle |\tilde{M}_j(t)|^2 \right\rangle \left| \hat{h}_j'(\omega^{(p)}) \right|^2 / \sin^2 \vartheta_j}{\sqrt{\sum_{j,k} \left\langle |\tilde{M}_j(t)|^2 \right\rangle \left\langle |\tilde{M}_k(t)|^2 \right\rangle \left| \hat{h}_j'(\omega^{(p)}) \right|^2 \left| \hat{h}_k'(\omega^{(p)}) \right|^2 \cos[2(\hat{\beta}_j^{(p)} - \hat{\beta}_k^{(p)})]}}. \end{aligned} \quad (3.2.52)$$

3.2.3 Polarization structure of the fields at harmonic frequencies of power lines

The operating frequencies $f=50$ Hz and 60 Hz of electric power lines fall into the range of higher-order Schumann resonances $8 \leq n \leq 10$. It follows from the above given analysis that ellipticity ratios of the ELF fields excited in the gyrotropic cavity at resonance frequencies of numbers as high as these are vanishingly small, such that the fields can be regarded as linearly polarized to a very good accuracy. This means that the results obtained in the Annual Progress Report [P-072, 2002] with regard to the polarization structure of the ELF fields emitted by power lines in the isotropic cavity remain fully valid for the gyrotropic case as well. Briefly, they can be summarized as follows.

1. The potential sources of the ELF fields detectable at harmonic frequencies of electric power lines are major industrial centers of the economically developed countries. For the harmonics of $f=60$ Hz, three such centers can be indicated, namely

- South-Western region of the USA;
- North-Eastern US – Southern Canada
- South Eastern Brazil.

2. Owing to the small extent of the radiating centers compared with the radiation wavelength, all of the centers may be regarded as point-size formations emitting linearly polarized electromagnetic fields whose magnetic vectors are oriented along the normal to the propagation path.

3. In view of the relatively high degree of coherence of the ELF fields emitted by electric power lines and the considerable separation of the radiating centers, the result of simultaneous action of a few centers should be an elliptically polarized field at an arbitrary observation point on the Earth surface. The polarization parameters are determined by relative positions of the observation point and each of the contributing radiation centers.

4. By measuring polarization parameters of the ELF fields excited by remote industrial regions at harmonic frequencies of power transmission lines, it proves possible to identify directions toward these sources of radiation and (with the knowledge of electric parameters of the waveguiding channel) estimate ratios of their current moments. In case the radiation conditions are known, model parameters of the propagation channel can be determined.

3.3 A theory of geomagnetic effects of cyclone-produced AGWs

It was noted in the Annual Progress Report [Project P-072, 2002] that simultaneous variations in the atmospheric pressure and magnetic field often demonstrate a high degree of correlation. A phenomenological model was developed to explain the probable physical mechanism. Actually, the packet of waveforms making the AGW that accompanied passage of a weather front over the observation point was, after some delay, reproduced in geomagnetic variations. It was also noticed that the magnetic variations can be mapped, without noticeable distortions of waveform or amplitude, to the conjugate region in the Northern hemisphere. Finally, correlation analysis of the baric pressure measurements and those of magnetic variations has shown the magnetic field effect to arise with a delay which can be interpreted as the time of AGW propagation to ionospheric altitudes. Thus, it has proven possible to identify a hypothetic chain of processes admittedly responsible for the observed effects, namely: 1 – upward propagation of a tropospherically generated AGW; 2 – modulation of ionospheric conductivity; 3 – generation of dynamo currents, and 4 – ionospheric current closure through the conjugate ionosphere (see Fig. 3.3.1)

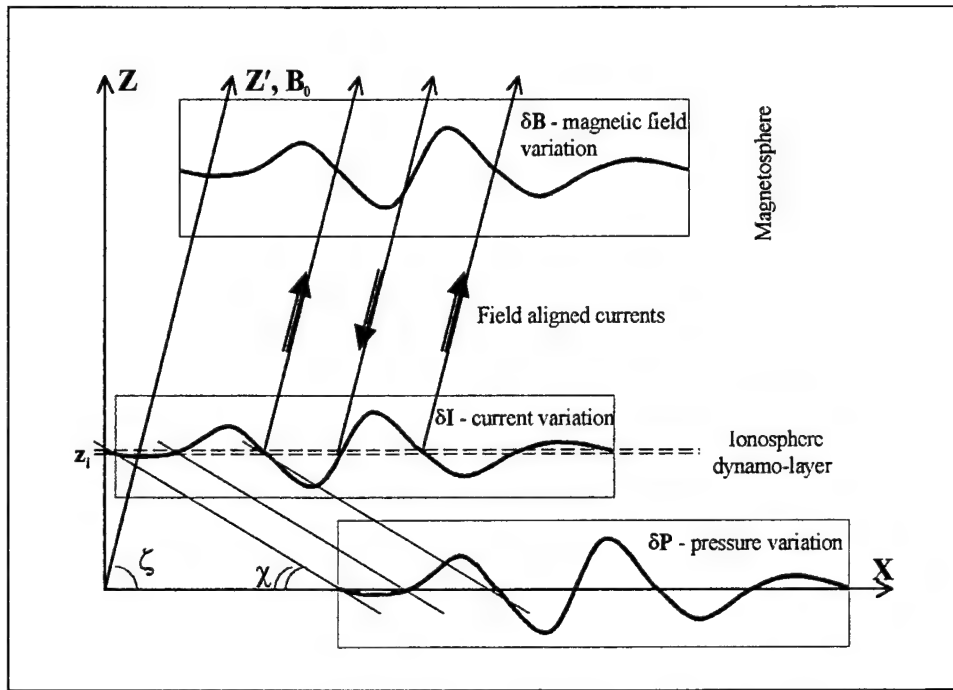


Fig. 3.3.1 The conjectural chain of interactions: AGW → ionospheric dynamo current → geomagnetic disturbance

The physics of large-scale AGW excitation by an atmospheric front is a problem of independent interest which is not discussed within this Project. We will only note that the plausibility of this source of internal waves in the atmosphere is often stated in the literature on atmosphere dynamics, however no rigorous theoretical model has been developed yet. Some evidence in support of the synoptic nature of AGWs was given by [Rice and Sharp, 1977] who analyzed direct measurements of wavelike disturbances at 140 to 200 km on board Atmospheric Explorer-C. The statistical analysis carried out by those writers revealed a correlation of AGWs with atmospheric weather structures, however not with K_p indices or magnetospheric processes.

3.3.1 Theoretical relations and numerical estimates

Atmospheric gravity waves have been discussed in a great number of papers (to consult just a few reviews, see [Hines, 1960; Hines, 1974, Francis, 1975; Gossard and Hooke, 1978; Briunelli and Namgaladze, 1988; Hocke and Schlegel, 1996; Williams, 1996]) whose results can be used in this Report.

Consider a Cartesian frame with the Z-axis (OZ) directed vertically upward and OX lying within the plane of the AGW wave vector, i.e. $\vec{k} = \{k_x, 0, k_z\}$. Under some conditions which will be

specified below, the monochromatic AGW can be represented as a non-uniform plane wave [Briunelli and Namgaladze, 1988]:

$$\frac{\delta N}{N(z)} = \frac{u}{U} = \frac{w}{W} = A(z) \exp\{i(\omega t - k_x x - k_z z)\}, \quad A(z) = \frac{\delta N}{N} \Big|_{z=0} \exp\left\{\frac{z}{2H}\right\}, \quad (3.3.1)$$

where δN is the density variation of the neutral atmosphere; u and w are, respectively, the horizontal and the vertical velocity components of the atmospheric particles; $N(z) \equiv N_0 \exp\{-z/H\}$ is the barometric distribution formula with (H denoting the scale height; $U = U(\omega, \vec{k})$, $W = W(\omega, \vec{k})$ are the coefficients to determine the vertical-to-horizontal ratio of particle velocities in the AGW (i.e., polarization constants). The exponential growth $\sim \exp\{+z/2H\}$ of the AGW amplitude results from the condition that the wave-transported energy flux should remain constant.

The frequency, ω , and wave vector \vec{k} of (3.3.1) are related by the dispersion law whose low-frequency branch ($\omega < \omega_g \equiv \sqrt{\gamma-1}g/c_s$) representing the internal gravity mode takes the form

$$\omega = c_g \frac{k \cos \theta}{\sqrt{1 + (2kH)^2}}, \quad (3.3.2)$$

where ω_g is the Brunt-Väisälä frequency; $c_g = 2[\sqrt{\gamma-1}/\gamma]c_s$, with c_s denoting the sound velocity; $\gamma = c_p/c_v$ is the adiabatic coefficient, and θ the wave vector inclination angle relative to the horizontal plane. Characteristic numerical magnitudes of these basic parameters are given in Table 3.3.1. In the gravity wave, the relation holds $|U/W| \gg 1$ [Briunelli and Namgaladze, 1988], such that the particle motions occur practically in the horizontal plane. The AGW group velocity depends both on the magnitude and direction of \vec{k} , viz.

$$V_{gx} = \frac{\partial \omega}{\partial k_x} = c_g \frac{1 + \kappa^2 \sin^2 \theta}{(1 + \kappa^2)^{3/2}}, \quad V_{gz} = \frac{\partial \omega}{\partial k_z} = -c_g \frac{\kappa^2 \sin \theta \cos \theta}{(1 + \kappa^2)^{3/2}}, \quad (3.3.3)$$

where a dimensionless wavenumber has been introduced as $\kappa \equiv 2H \cdot k$. The vertical component of the group velocity reaches its maximum value at $\kappa = \sqrt{2}$, $\theta = \pi/4$ (in other words, in the range of wavelengths $\lambda = 4\pi H / \sqrt{2}$ close to ≈ 70 km), with $V_{gz \max} \approx 0.2c_g \sim 60$ m/s.

Table. 3.3.1

Atmospheric parameters influencing AGW propagation
(the magnitudes listed in the Table correspond to near surface values for normal atmospheric conditions,
and to values averaged over the range of altitudes $0 < z < 130$ км).

Sound velocity c_s	Scale height, H	$\gamma = c_p/c_v$ for bi-atomic gas (N_2)	Horizontal velocity, c_g	Brunt-Väisälä frequency, ω_g , and period, T
Normal cond.: 340 m/s averaged: 300 m/s	8 km 7 km	7/5=1.4	307 m/s 270 m/s	$\omega_g = 0.01 \text{ s}^{-1}$, $T=10 \text{ min}$ $\omega_g = 0.011 \text{ s}^{-1}$, $T=9 \text{ min}$

The dispersion curves calculated after (3.3.2) for a variety of propagation directions, θ , are shown in Fig. 3.3.2.

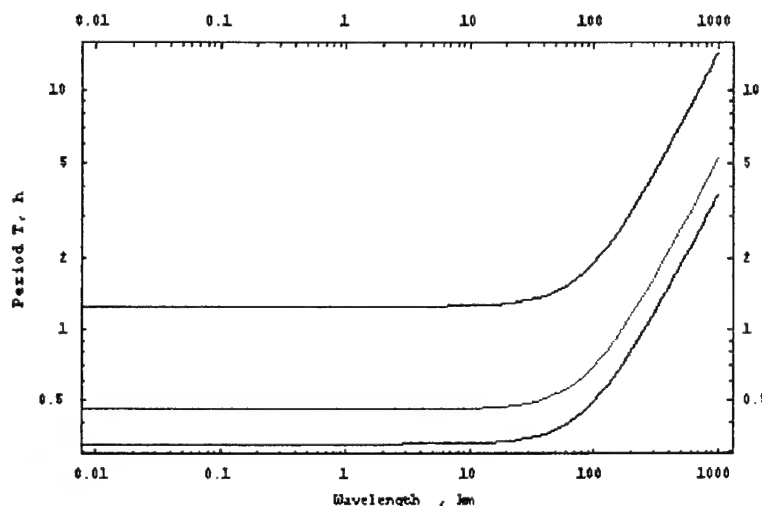


Fig. 3.3.2 Wave periods calculated in dependence on the wavelength for a variety of propagation directions (top to bottom: $\theta = 0^\circ$; $\theta = 45^\circ$ and $\theta = 80^\circ$)

The AGW observations at *Vernadsky* are single-site measurements which do not permit determining the modal composition of the wave observed (i.e. finding wave vector components in addition to the frequency). Therefore, we will make use of the general data stating that baric pressure variations of periods 1 to 3 hr are manifestations of AGWs whose horizontal scale lengths $\lambda_x = 2\pi/k_x$ make a few hundreds of kilometers [Hocke and Schlegel, 1996]. Assuming that the pressure variations measured near *Akademik Vernadsky* are no exception, we can estimate the length of the corresponding AGWs as $\lambda = \lambda_x \cos\theta \sim 100$ km. All other parameters then can be estimated from the dispersion law (3.3.2) (cf. Table.3.3.2).

Table.3.3.2

AGW parameters as determined from experiment and theory
 (θ and ψ are the angles made by phase and group velocities relative to the horizontal plane)

Measured data		Literature data	Theoretical estimates		
Amplitude near the surface	Frequency, ω and period, T	Wavelength, λ	Vertical group velocity component, V_{gz}	Directions of the phase (θ) and group (ψ) velocities	AGW growth factor, $\exp\{z/2H\}$
$\delta N/N _{z=0} = 3 \times 10^{-4}$ (0.3 mbar)	$(6-17) \times 10^{-4} \text{ s}^{-1}$ ($T=1-3 \text{ hr}$)	$\sim 100 \text{ km}$	8 - 23 m/s	$\theta = 75^\circ - 85^\circ$, $\psi = 7^\circ - 2^\circ$	3×10^3 at $z = 120 \text{ km}$ $\langle H \rangle = 7 \text{ km}$

The group velocity is shown in Fig. 3.3.3 as a function of the AGW period and wavelength. Taking $z_i \sim 130 \text{ km}$ as the level of localization of ionospheric currents, we can find, for the AGW parameters of Tables 3.3.1 and 3.3.2, $\tau_{\text{delay}} = 10 - 60 \text{ min}$. This figure is agreement with the magnitude obtained from the cross-correlation analysis of measured data (see Subsection 4.5)

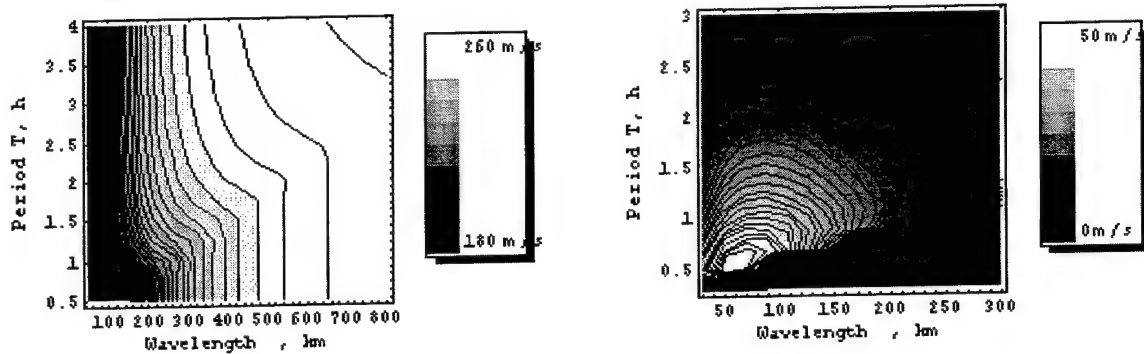


Fig. 3.3.3 The horizontal (left panel) and vertical (right-hand panel) group velocity components of AGWs.

Proceeding from a simple (barometric model of the height profile of neutral atmosphere density, we can evaluate the relative AGW amplitude as a function of altitude (Fig. 3.3.4).

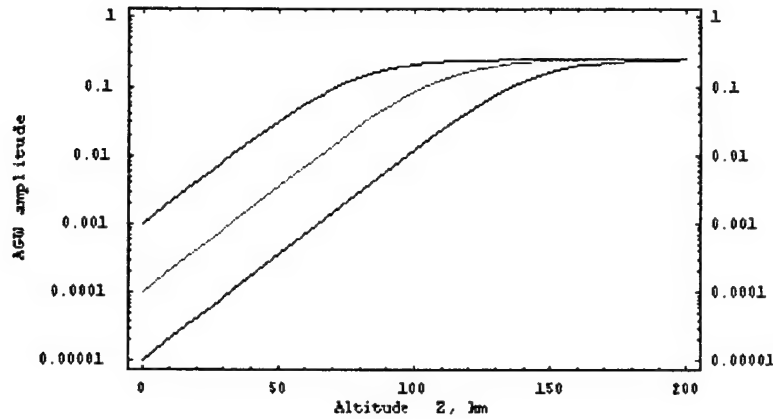


Fig. 3.3.4 Model dependence of the relative AGW amplitude, $\delta N/N$, versus height (with account of the nonlinear saturation, $(\delta N/N)_{\max}=0.3$)

3.3.2 Generation mechanisms of the dynamo current. Ion drag and modulated conductivity

A vast body of literature is known on the theory of processes in the ionospheric dynamo layer [Rishbeth and Garriot; 1969, Gershman, 1974; Sorokin and Fedorovich, 1982; Evans, 1978; Pokhotelov et al., 1994; Galperin and Hayakawa, 1996; Lizunov, 2002, etc. See also the bibliographies therein]. In most cases, the authors study the magnetic response to ionospheric propagation of small-scale AGWs (generated by chemical or nuclear explosions, volcanic eruptions, earthquakes, etc.) or on the contrary, of the large-scale flows associated with solar and lunar tides, planetary waves, etc. We will discuss here the physical mechanisms that may be responsible for the generation of dynamo currents by an atmospheric gravity wave. Consider the electric current of density \vec{j}_0 produced in the dynamo region by some external sources,

$$\vec{j}_0 = en_p \vec{V}_0 = \hat{\sigma} \cdot \vec{E}_0, \quad (3.3.4)$$

where n_p is the plasma density; $\vec{V}_0 = \hat{\mu} \vec{E}_0$ the current-related ion velocity; \vec{E}_0 the large scale electric field (for example, of magnetospheric origin); $\hat{\mu}$ the ion mobility tensor, and $\hat{\sigma}$ the conductivity tensor. We will be interested in the AGW-produced modulation of (3.3.4). Within the linear approximation ($\delta V \ll V_0$, $\delta n_p \ll n_p$) the current variation is

$$\delta \vec{j} = en_p \cdot \delta \vec{V} + e \delta n_p \cdot \vec{V}_0. \quad (3.3.5)$$

The two terms in the right-hand part of (3.3.5) correspond to two different physical processes.

The first term,

$$\delta \vec{j}_{drag} = en_p \cdot \delta \vec{V} \quad (3.3.6)$$

represents the current appearing when ions get involved in the oscillatory motion of neutral particles, $\delta V_i \sim V_n$. This mechanism of current generation does not require presence of a background current, j_0 . The second term,

$$\delta \vec{j}_{mod} = e \delta n_p \cdot \vec{V}_0 = \delta \hat{\sigma} \cdot \vec{E}_0 \quad (3.3.7)$$

describes the effect of conductivity modulation (the Pedersen and Hall conductivities of the plasma are modulated by the AGW). To analyze the motion of ionospheric ions under the action of an AGW, we introduce the primed frame tied to the geomagnetic field and, accordingly, tilted with respect to the XYZ frame (see Fig. 3.3.5). In the quasistatic limit ($\omega \ll \omega_{ci}$) the particle velocities are related as

$$\vec{V}_i + \frac{\omega_{ci}}{v_{in}} \hat{z}' \times \vec{V}_i = \vec{V}_n \quad (3.3.8)$$

where \vec{V}_i is the ion velocity; $\vec{V}_n \approx \hat{x} \cdot u$ the oscillatory speed of neutral particles in the AGW (it is oriented roughly within the horizontal plane); \hat{x} is the unit vector along OX; \hat{z}' the unit vector along the geomagnetic field; ω_{ci} is the ion gyrofrequency (also denoted Ω_i in other Subsections of this Report), and v_{in} the ion-neutrals collision frequency. By solving (3.3.8) we can obtain the ion velocity components perpendicular to the geomagnetic field,

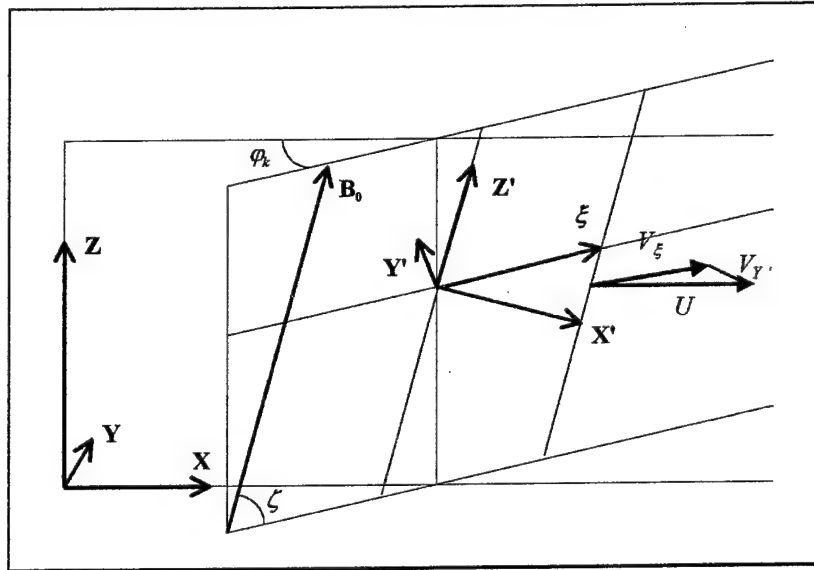


Fig.3.3.5 Mutual orientation of the XYZ (AGW-related) and X'Y'Z' (geomagnetic field-related) frames of reference. See the velocity vector U of neutral particles get projected onto the magnetic sheet

$$\begin{aligned} V_{X'} &= p \cdot u_{X'} - h \cdot u_{Y'}, \\ V_{Y'} &= h \cdot u_{X'} + p \cdot u_{Y'}, \end{aligned} \quad (3.3.9)$$

where $u_{X',Y'}$ are velocity components of neutral particles in the primed frame of reference,

$$p = \frac{1}{1 + r_i^2}, \quad h = \frac{r_i}{1 + r_i^2}, \quad r_i = \frac{\omega_{ci}}{\nu_{in}}. \quad (3.3.10)$$

The latter functions can be approximately represented in an analytic form. To do so let, us determine the characteristic height z_i having the sense of the upper edge for the dynamo region. It is defined by

$$\omega_{ci} = \nu_{in} \text{ at } z = z_i. \quad (3.3.11)$$

The prevailing ion in the E-region being NO^+ , the gyrofrequency is $\omega_{ci} = 168 \text{ c}^{-1}$ and, according to the model of Fatkullin et al.[1981], z_i can be estimated as $z_i \approx 130 \text{ km}$. The collision frequency decreases with height in proportion with the density of neutrals, $\nu_{in} \sim N = N_0 e^{-z/H}$, hence

$$p = p(z - z_i) = \frac{1}{1 + e^{2(z-z_i)/H}}, \quad h = h(z - z_i) = \frac{e^{(z-z_i)/H}}{1 + e^{2(z-z_i)/H}}, \quad r_i = e^{(z-z_i)/H}. \quad (3.3.12)$$

The electron velocity is calculated in a similar way,

$$\begin{aligned} V_{ex'} &= p(z - z_e) \cdot u_{x'} - h(z - z_e) \cdot u_{y'}, \\ V_{ey'} &= h(z - z_e) \cdot u_{x'} + p(z - z_e) \cdot u_{y'}, \end{aligned} \quad (3.3.13)$$

where $z_e \approx 80 \text{ km}$ is the lower edge of the dynamo region which is determined from $\omega_{ce} = \nu_{en}(z_e)$. Inside the dynamo region, at $z_e < z < z_i$ we have $p(z - z_e) \ll 1$ and $h(z - z_e) \ll 1$ (the electrons are glued to the lines of force), and hence the current density across the magnetic field is controlled largely by the motion of the ion component, i.e.

$$\begin{aligned} j_{x'} &= en_p (V_{ix'} - V_{ex'}) \approx en_p [p(z - z_i)u_{x'} - h(z - z_i)u_{y'}], \\ j_{y'} &= en_p (V_{iy'} - V_{ey'}) \approx en_p [h(z - z_i)u_{x'} + p(z - z_i)u_{y'}]. \end{aligned} \quad (3.3.14)$$

Thus, the current density in the dynamo region proves to be height-dependent, both because the AGW is a nonuniform wave, $u \sim \exp\{z/2H\}$, and because $p = p(z)$ and $h = h(z)$ are not constant values. As a result, the current divergence is not zero $\nabla \cdot \vec{j} \approx \partial j_z / \partial z \sim j_z / H$.

The current to close the circuit and 'neutralize' the dynamo-region current apparently is the field aligned electron current. Without dwelling on details of its generation (see [Gershman, 1974, Rishbeth and Garriot, 1969], we can devise the geometric scheme of the circuit closure. According to Fig. 3.3.6, the net current in the dynamo region (the electron and the ion current components) is directed horizontally. The primed geometric components are $j_\xi = j_{x'} / \sin \zeta$ and $j_{y'}$, while the components in the XYZ system are

$$\begin{aligned}
 j_X &= j_P + j_H \frac{\sin 2\varphi_k \cos^2 \zeta}{2 \sin \zeta}, \\
 j_Y &= j_H \frac{\sin^2 \varphi_k + \cos^2 \varphi_k \sin^2 \zeta}{\sin \zeta},
 \end{aligned}
 \tag{3.3.15}$$

where $j_P = en_p u \cdot p(z - z_i)$ and $j_H = en_p u \cdot h(z - z_i)$ are the Pedersen and the Hall current components, respectively.

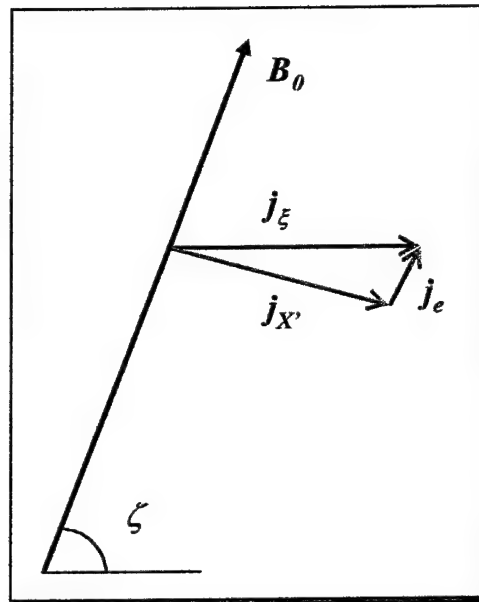


Fig. 3.3.6 Closing the transverse ion current with a field-aligned electron current

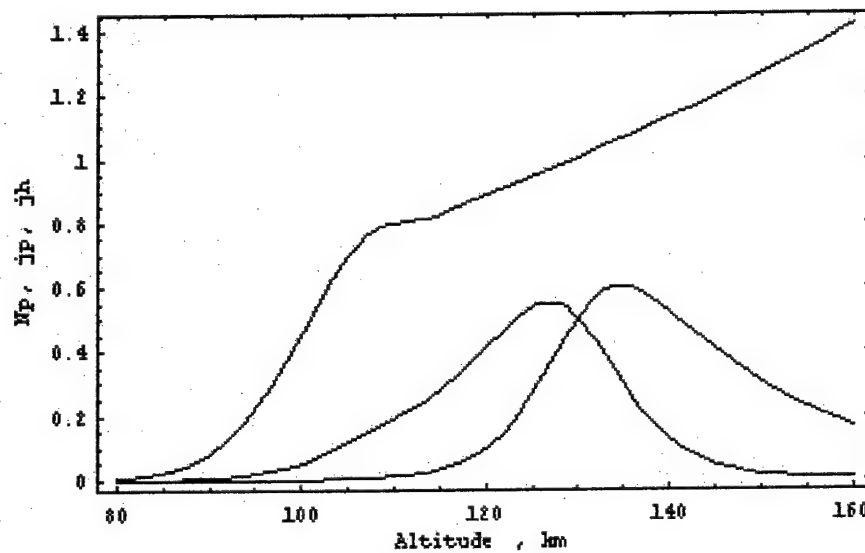


Fig. 3.3.7 Plasma density and current distributions: $N_p(z)$ (black); $\tilde{j}_P(z)$ (red) and $\tilde{j}_H(z)$ (blue)

Having estimated the conductivity distributions, it is easy to evaluate current densities in the dynamo-region and their magnetic effect. Such estimates are given in Table 3.3.3 for several values of the AGW amplitude. Shown in Fig. 3.3.8 are magnetic field dependences on the azimuthal direction φ_k of AGW propagation (the calculations have been done for $\zeta = 60^\circ$, i.e. the magnetic dip angle of *Vernadsky*).

Table. 3.3.3

AGW-produced magnetic field and current disturbances in the ionosphere: n_* and u_* are, respectively, the plasma density and neutral component velocity at $z_i=130$ km

$n_* = 2 \cdot 10^4 \text{ cm}^{-3}$ (night)		$n_* = 2 \cdot 10^5 \text{ cm}^{-3}$ (day time)	
$u_* = 10 \text{ m/s}$ (moderate)	$u_* = 70 \text{ m/s}$ (high)	$u_* = 10 \text{ m/s}$ (moderate)	$u_* = 70 \text{ m/s}$ (high)
$I_* = 0.5 \frac{\text{A}}{\text{m}}, B_* = 0.3 \text{ nT}$	$I_* = 3.5 \frac{\text{A}}{\text{m}}, B_* = 2 \text{ nT}$	$I_* = 5 \frac{\text{A}}{\text{m}}, B_* = 3 \text{ nT}$	$I_* = 35 \frac{\text{A}}{\text{m}}, B_* = 20 \text{ nT}$

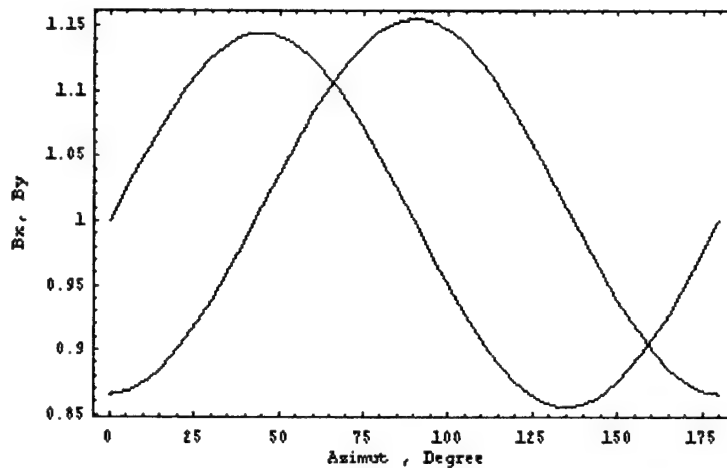


Fig.3.3.8 Azimuthal dependences of magnetic components, $B_X = \delta B_X / B_*$, $B_Y = \delta B_Y / B_*$ (red and blue, respectively), upon the AGW propagation direction

3.3.3 AGW impact on ionospheric plasma parameters

The effect of atmospheric gravity waves upon ionospheric parameters, including the plasma conductivity, was analyzed in the fundamental paper of Hooke [1968]. The attention was centered mainly on the F-region (since the subject was traveling ionospheric disturbances), and the analysis faced certain difficulties. The lifetime of ions above 200 km is long enough to require allowance for variations in the photochemical coefficients under the action of the AGW,

as well as for the spatial transport of ions. The variation in electron temperature in this range of altitudes is not equal to the ion temperature variation, and both are different from the temperature variation of the neutral component. In addition, the back action of plasma motion on the propagation of AGWs cannot be ignored at the heights of F2 region [Sorokin and Fedorovich, 1982]. Meanwhile, many of these problems do not apply the dynamoregion which is the area of our interest. The ion lifetime τ_i below 150 km is less than one minute in the daytime or about 1 hr at night [Briunelli and Namgaladze, 1988], which is less than the period of the AGWs considered. 'Strong' inequalities hold in the daytime, namely

$$\omega\tau_i \ll 1, \quad kV_{Ti}\tau_i \ll 1, \quad (3.3.16)$$

($V_{Ti} = \sqrt{2T_i/M_i}$ is the ion thermal velocity). Under these conditions an AGW plays the part of a quasistationary and quasiuniform background exerting influence on the plasma density through variation of photochemical coefficients, specifically of ion production and recombination rates.

Consider the disturbances of density and temperature of the neutral component, produced by an atmospheric gravity wave,

$$\frac{\delta N(z)}{N(z)} \equiv A(z), \quad (3.3.17)$$

$$\frac{\delta T(z)}{T} \approx (\gamma - 1)A(z), \quad (3.3.18)$$

where $\gamma = c_p/c_v \approx 1.4$. We will aim at estimating variations in the density and temperature of the charged components, and in the ion-neutral collision frequency, i.e.

$$\frac{\delta n_p}{n_p}, \quad \frac{\delta T_i}{T_i}, \quad \frac{\delta \nu_{in}}{\nu_{in}} = \frac{\delta N}{N} + \frac{\delta T_i}{2T_i}.$$

Variations in plasma temperature. The scale times of temperature exchange between the electrons, ions and neutral atmospheric particles below some 130 or 150 km are short (e.g., the time of ion thermalization is $\tau_T \sim \nu_{in}^{-1} \sim 0.01$ s, with the electron thermalization time being a value of the same order). For this reason, $T_e = T_i = T$ to a very good accuracy, and hence

$$\frac{\delta T_i}{T_i} = \frac{\delta T}{T} = (\gamma - 1)A(z). \quad (3.3.19)$$

Variations in plasma density. The mechanism of AGW effect on the ion production rate is more complex. To analyze this physics, let us start with a simple model where the ionosphere is represented by a single Chapman layer (see Fig. 3.3.9). Then

$$q(z) = q(N(z)) = A_\lambda N(z) \exp\left\{-\sigma_\lambda \sec \chi \int_z^\infty N(z) dz\right\}, \quad (3.3.20)$$

where A_λ and σ_λ are certain coefficients dependent on the ionizing radiation wavelength, and χ is the zenith angle of the Sun. With $N(z) \sim \exp\{-z/H\}$ (3.3.20) reduces to the Chapman distribution,

$$q(z) = q_m \exp\{1 - \tilde{z} - \sec \chi \cdot e^{-\tilde{z}}\}, \quad (3.3.21)$$

where $\tilde{z} \equiv (z - z_m)/H$ is the normalized height, and z_m the layer peak height. By varying the neutral density N in (3.3.21) we can express the variation in the ion production rate as.

$$\frac{\delta q}{q} = F(\tilde{z}) \frac{\delta N}{N}, \quad (3.3.22)$$

with $F(\tilde{z}) \equiv 1 - 2 \sec \chi \cdot e^{-\tilde{z}}$ (Actually, 3.3.22 has been obtained in the linear approximation, on the assumption of $|\delta q/q| \ll 1$). The function $F(z)$ is shown in Fig. 3.3.9 for the E-layer plasma ($z_m = 105$ km, $H = 7$ km).

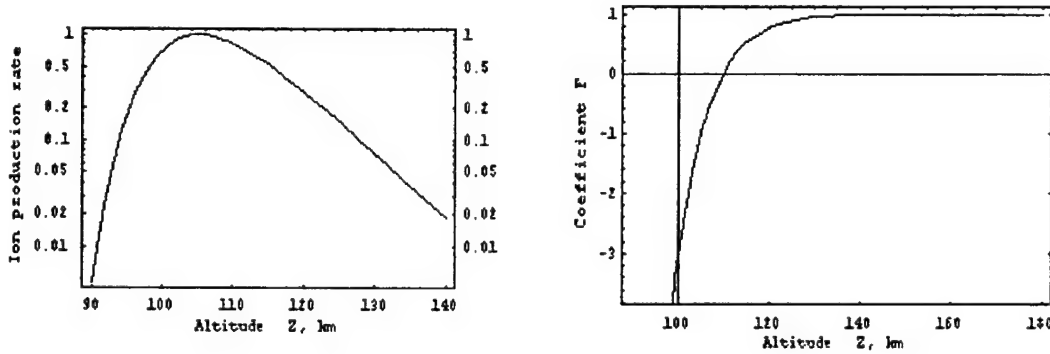


Fig. 3.3.9 The left-hand pattern represents the ion production rate for the Chapman layer modeling the ionospheric E-region. The function $F(z)$ in the right-hand pattern describes the relation between variations in the neutral particle density and the rate of ion production.

As can be seen from the results discussed, the effect of AGW on the rate of ion production is height dependent. Above the layer peak (at $z \gg z_m$) the relation holds

$$F(z) \approx 1, \quad \frac{\delta q}{q} \approx \frac{\delta N}{N}, \quad (3.3.23)$$

i.e. the rate of production of electron – ion pairs is proportional to the local density of ion-producing neutrals. The $\delta q - \delta N$ relation of a greatly different kind exists near the layer peak

and below ($\tilde{z} \leq 0$). The variations in q and N are in counter-phase ($\delta q \sim -\delta N$) and differ in relative magnitude,

$$\left| \frac{\delta q}{q} \right| \gg \left| \frac{\delta N}{N} \right|. \quad (3.3.24)$$

In this case, the effect of the neutral component's density variation upon the rate of ion production is not local but is rather exerted through changes in the ionizing radiation intensity owing to the extra absorption (transmission) in the upper lying atmosphere.

Now we can consider a more realistic model of the dynamo region. Up to 80-150 km (the E and F1 regions), the ion production rate will be represented approximately by a set of partial Chapman layers [Briunelli and Namgaladze, 1988]:

$$q_{\Sigma}(z) = q_{O_2}(z) + q_{N_2}(z) + q_O(z) = \sum_m q_m(z), \quad (3.3.25)$$

where $q_m(z) = q_m \exp\{1 - \tilde{z}_m - \sec \chi \cdot e^{-\tilde{z}_m}\}$, $\tilde{z}_m \equiv (z - z_m)/H$, z_m is the peak height of the partial layer. All the layers are characterized by the same scale height of the atmosphere, H (like in the region below the turbopause). The variation of (3.3.25) takes the form

$$\frac{\delta q}{q} = F_{eff}(z) \frac{\delta N}{N}, \quad \text{где} \quad F_{eff}(z) \equiv 1 - 2 \sec \chi \cdot \sum_m \frac{q_m(z)}{q_{\Sigma}(z)} e^{-(z-z_m)/H} \quad (3.3.26)$$

The dynamo-layer model (3.3.25) and the function $F_{eff}(z)$ are presented in Fig. 3.3.10

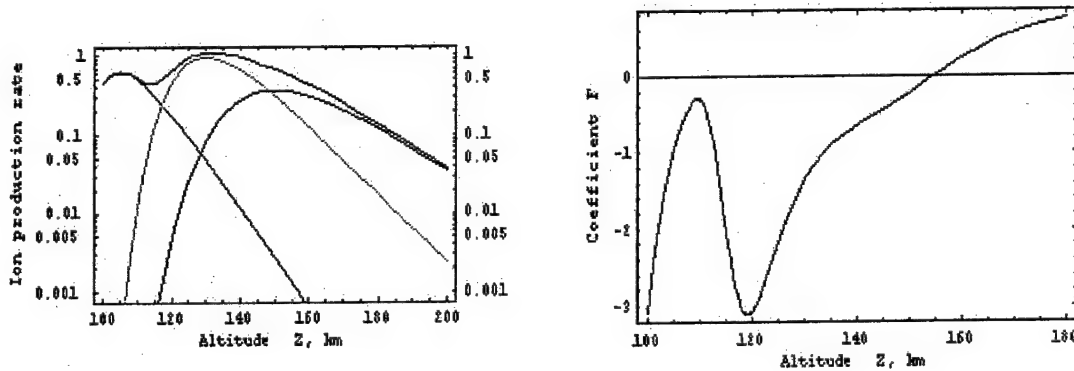


Fig. 3.3.10 The left-hand pattern shows the height profile of the ion production rate, $q_{\Sigma}(z)$. The dynamo region is represented by a sum of partial Chapman layers. The right-hand pattern is the correspondent $F_{eff}(z)$ distribution.

The results obtained permit evaluating the plasma density variation under the action of a AGW. The photochemical equilibrium in the E and F1 regions is controlled by the recombination via binary electron-ion collisions [Briunelli and Namgaladze, 1988], when

$$n_p(z) = \sqrt{\frac{q_z(z)}{\alpha_{eff}(T)}}, \quad (3.3.27)$$

(α_{eff} is the temperature dependent effective recombination factor). Mul and McGowan [1979], suggested a power-law phenomenological dependence for $\alpha_{eff}(T)$,

$$\alpha_{eff} = \alpha_{eff}(T) \sim T^{-\beta}, \quad (3.3.28)$$

with $\beta \approx 0.5$. By combining (3.3.35), (3.3.36), (3.3.34) and (3.3.28), we can express the sought-for density variation as

$$\frac{\delta n_p}{n_p} = \frac{1}{2} \left(\frac{\delta q_z}{q_z} - \frac{\delta \alpha_{eff}}{\alpha_{eff}} \right) = \frac{1}{2} \left(F_{eff} \frac{\delta N}{N} + \beta \frac{\delta T}{T} \right) = \frac{1}{2} (F_{eff}(z) + \beta(\gamma - 1)) \cdot A(z). \quad (3.3.29)$$

The collision frequency variation is

$$\frac{\delta \nu_m}{\nu_m} = \frac{\delta N}{N} + \frac{\delta T_i}{2T_i} = \frac{\gamma + 1}{2} A(z). \quad (3.3.30)$$

3.3.4 Variations in ionospheric conductivity

The cross-field part of the conductivity tensor can be written in the primed system X'Y'Z' (the OZ' axis is along the geomagnetic field) as [Pokhotelov et al., 1994]:

$$\hat{\sigma} = \begin{pmatrix} \sigma_{X'X'} & \sigma_{X'Y'} \\ \sigma_{Y'X'} & \sigma_{Y'Y'} \end{pmatrix} = \begin{pmatrix} \sigma_P & \sigma_H \\ -\sigma_H & \sigma_P \end{pmatrix}, \quad (3.3.31)$$

where $\sigma_P = \frac{ec}{B_0} n_p \cdot \left(\frac{r_i}{1+r_i^2} + \frac{r_e}{1+r_e^2} \right)$, and $\sigma_H = \frac{ec}{B_0} n_p \cdot \left(\frac{r_i^2}{1+r_i^2} - \frac{r_e^2}{1+r_e^2} \right)$ are, respectively, the Pedersen and the Hall conductivities; $r_\alpha = \omega_{c\alpha} / \nu_{\alpha m}$, $\alpha = e, i$. In the dynamo region ($r_i \sim 1$, $r_e \gg 1$) we have

$$\sigma_P \approx \frac{ec}{B_0} n_p \frac{r_i}{1+r_i^2}, \quad \sigma_H \approx -\frac{ec}{B_0} n_p \frac{1}{1+r_i^2}. \quad (3.3.32)$$

Approximate analytical expressions for these functions are (cf. (3.3.12)):

$$\sigma_P = \sigma_P(z) = \frac{ec}{B_0} n_p(z) h(z), \text{ and } \sigma_H = \sigma_H(z) = -\frac{ec}{B_0} n_p(z) p(z). \quad (3.3.33)$$

Now we can turn to considering the AGW-produced variations. According to (3.3.32),

$$\frac{\delta\sigma_P}{\sigma_P} = \frac{\delta n_P}{n_P} + \frac{r_i^2 - 1}{r_i^2 + 1} \frac{\delta v_{in}}{v_{in}}, \quad \frac{\delta\sigma_H}{\sigma_H} = \frac{\delta n_P}{n_P} + \frac{2r_i^2}{r_i^2 + 1} \frac{\delta v_{in}}{v_{in}}. \quad (3.3.34)$$

Having substituted (3.3.29), (3.3.30) and (3.3.12) into (3.3.34) we arrive at

$$\begin{aligned} \delta\sigma_P &= \frac{ec}{2B_0} n_P(z) \cdot A_* \cdot \left[F_{eff}(z) + a_1 + \frac{a_2}{1+r_i^2(z)} \right] \frac{r_i^{3/2}(z)}{1+r_i^2(z)}, \\ \delta\sigma_H &= -\frac{ec}{2B_0} n_P(z) \cdot A_* \cdot \left[F_{eff}(z) + a_3 - \frac{2a_2}{1+r_i^2(z)} \right] \frac{r_i^{1/2}(z)}{1+r_i^2(z)}, \end{aligned} \quad (3.3.35)$$

where $r_i(z) = \exp\{z - z_i\}/H\}$; $A_* = A(z_i)$ is the AGW amplitude at the edge of the dynamo region; $a_1 = \beta(\gamma - 1) + 1 + \gamma \approx 2.6$, $a_2 = \gamma - 1 \approx 0.4$ and $a_3 = a_1 + 1 + \gamma \approx 5$. The conductivity profiles calculated from (3.3.34), (3.3.35) with $A_* = 0.2$ are given in Fig.3.3.11

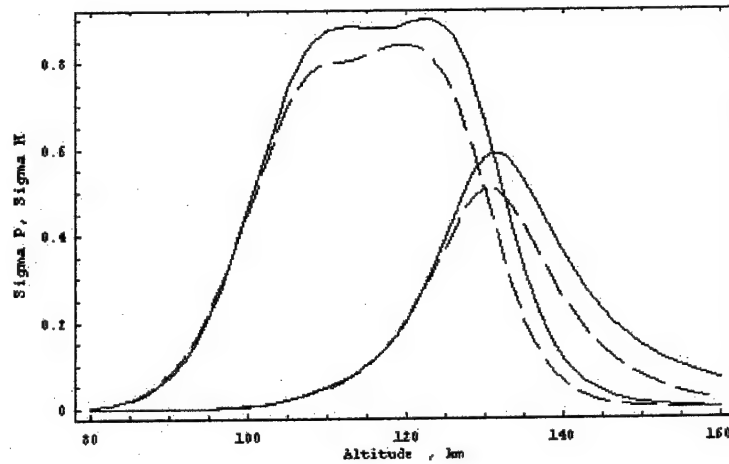


Fig. 3.3.11 Vertical profiles of the Pedersen (red line) and Hall (blue line) ionospheric conductivities. The dashed curves show the run of the conductivities in the absence of a AGW.

3.3.5 Generation of magnetic disturbances

We can analyze now the dynamo current arising from modulation of the ionospheric plasma conductivity. Let us assume that a background current, unrelated to the AGW, flows through the ionosphere. At this point we are not interested in its physical nature, just noting that a background current is always present and can reach considerable magnitudes (cf. Table 3.3.4). Within the spatial scales of the AGW, this current may be regarded as quasisuniform and quasi-d.c., which assumptions are valid for the structures listed in Table 3.3.4., with the exception of small-scale auroral currents. Further, we assume the background current to be produced by a

horizontal electric field \vec{E}_0 acting in the ionosphere. The fields and currents can be described in the frame of reference $X''Y''Z''$ whose x-axis (OX'') is directed along \vec{E}_0 ; the OY'' axis is at an angle φ_E to OY' (thus, φ_E is the azimuthal angle of \vec{E}_0 with respect to the magnetic plane $X'Y'Z'$, see Fig. 3.3.5). The components of the integrated ionospheric current are

Табл. 3.4

Characteristics of powerful current systems in the ionosphere

Source	Maximum disturbance	Localized at
Equatorial electrojet	Integrated current $I \sim 350$ mA/m Magnetic variation $B \sim 200$ nT	Equatorial ionosphere
Magnetospheric convection field mapped to the ionosphere	Integrated current $I \sim 200$ mA/m Magnetic variation $B \sim 120$ nT	Polar caps
Large-scale auroral (Birkeland) currents	Current $I \sim 100$ mA/m Magnetic variation $B \sim 60$ nT	Auroral ovals
Small-scale auroral structures	Maximal current $I \sim 500$ mA/m Magnetic variation $B \sim 300$ nT	Auroral arcs, scale lengths ~ 10 km
Solar tides (S_q variations)	Dynamo field $E \sim 10$ mV/m, Integrated current $I \sim 40$ mA/m Magnetic variation $B \sim 20$ nT	Low and middle latitudes

$$I_{X''} = \left[\Sigma_P - \Sigma_H \frac{\sin 2\varphi_E \cos^2 \zeta}{2 \sin \zeta} \right] \cdot E_0, \quad (3.3.36)$$

$$I_{Y''} = -\Sigma_H \frac{\sin^2 \varphi_E + \cos^2 \varphi_E \sin^2 \zeta}{\sin \zeta} \cdot E_0,$$

where $\Sigma_P = \int_{z_e}^{\infty} \sigma_P dz$, $\Sigma_H = \int_{z_e}^{\infty} \sigma_H dz$ are integrated Pedersen and Hall conductivities, respectively. If the plasma density profiles are sufficiently smooth, like in Fig. 3.3.7 or 3.3.9, then

$$\Sigma_P = \frac{ec}{B_0} n_* \frac{\pi}{2} H, \text{ and } \Sigma_H = -\Gamma \cdot \Sigma_P \approx -2.5 \cdot \Sigma_P \quad (3.3.37)$$

where $n_* = n_p|_{z=z_i}$ and $\Gamma = |\Sigma_H / \Sigma_P|$ (in the present case, $\Gamma \approx 2.5$). Integrating (3.3.37), we obtain the AGW-produced variation of the integrated conductivities,

$$\delta \Sigma_P = \int_{z_e}^{\infty} \delta \sigma_P dz = A_* \cdot g \cdot \Sigma_P, \text{ and } \delta \Sigma_H = \int_{z_e}^{\infty} \delta \sigma_H dz \approx \delta \Sigma_P \quad (3.3.38)$$

(g is a numerical factor about unity which is dependent on the $n_p(z)$ and $F_{eff}(z)$ distributions).

The appropriate variation in the dynamo current can be expressed as

$$\begin{aligned}\delta I_{X''} &= A_i g \frac{2 \sin \zeta - \sin 2\varphi_E \cos^2 \zeta}{2 \sin \zeta - \Gamma \sin 2\varphi_E \cos^2 \zeta} I_{X''}, \\ \delta I_{Y''} &= \frac{A_i g}{\Gamma} I_{Y''}.\end{aligned}\quad (3.3.39)$$

It seems more convenient to express the magnetic variation $\delta B_{X''} = -\frac{2\pi}{c} \delta I_{Y''}$, $\delta B_{Y''} = \frac{2\pi}{c} \delta I_{X''}$ in terms of the background magnetic field variation rather than the ionospheric current which is not directly measurable. The background variation is $\delta B_{0X''} = -\frac{2\pi}{c} I_{Y''}$, $\delta B_{0Y''} = \frac{2\pi}{c} I_{X''}$

$$\begin{aligned}\delta B_{X''} &= \frac{A_* g}{\Gamma} \delta B_{0X''}, \\ \delta B_{Y''} &= A_* g \frac{2 \sin \zeta - \sin 2\varphi_E \cos^2 \zeta}{2 \sin \zeta - \Gamma \sin 2\varphi_E \cos^2 \zeta} \delta B_{0Y''}.\end{aligned}$$

The magnitude of a AGW-produced magnetic pulsation thus is $\delta B_{AGW} \sim A_* \cdot \delta B_0$. For a maximum AGW amplitude of $A_* \sim 0.2$ (at the dynamo region altitude) and an external disturbance $\delta B_0 \sim 100$ nT we would have $\delta B_{AGW} \sim 20$ nT.

So, we have shown magnetic field variations to appear under the action of two factors, namely generation of the dynamo current δj_{drag} , associated with ion drag, and variation δj_{mod} of the external current owing to modulation of the ionospheric conductivity. Comparison of contributions from the two effects shows the former to be greater. The modulation effect prevails only with sufficiently high pressure disturbances.

3.3.6 Transfer of disturbances to the conjugate region

The geomagnetic variations recorded at *Akademik Vernadsky* in Antarctica are often detected in the conjugate region, near Boston, Mass.— practically without distortion of the waveform but with a slight delay in time (a few seconds). A natural explanation seems to be that the AGW-produced dynamo current in the Southern ionosphere becomes closed by field-aligned magnetospheric currents via the conjugate ionosphere. The schematic is given in Fig. 3.3.12.

To analyze the process, we will make some simplifying assumptions:

- 1) the geomagnetic field is vertically oriented, $\zeta = \pi/2$;
- 2) the ionospheric background current is absent ($E_0 = 0$);

- 3) the ionosphere is an infinitesimally thin current sheet located at $z = z_i$, with a uniform magnetosphere above;
- 4) the magnetosphere can be described within the ideal magnetohydrodynamics (implying $\sigma_{zz} / \sigma_{p,H} \rightarrow \infty$ for quasistationary processes, where σ_{zz} is the longitudinal plasma conductivity).

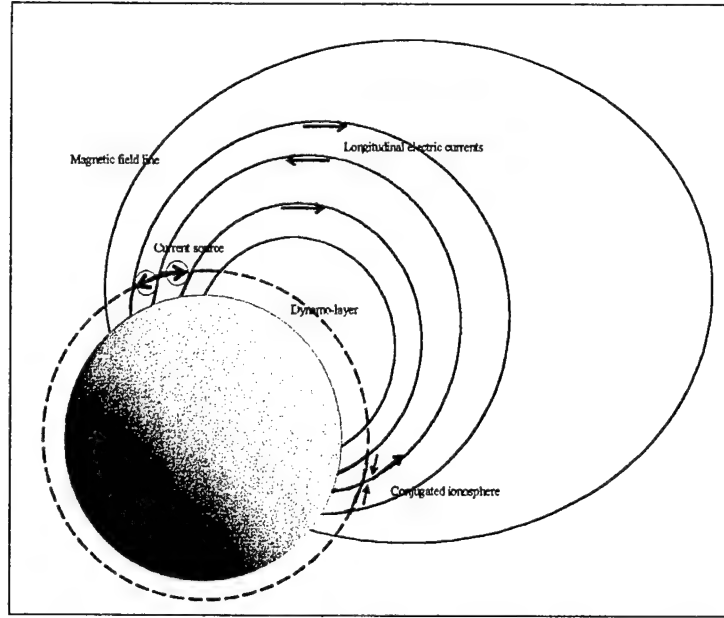


Fig. 3.3.12 Closing the electric circuit for dynamo currents via the conjugate ionosphere.
The source region is represented as a chain of current generators

It can be easily shown that components of the integrated dynamo current reproduce the horizontal-plane structure of the AGW (see Fig. 3.3.1). With $\zeta = \pi/2$, we have

$$I_X(t, x, y) = I_Y(t, x, y) = I_* \cos(\omega t - k_X x + \Delta\varphi), \quad (3.3.40)$$

where $\Delta\varphi$ is the phase shift appearing in the course of AGW propagation from the Earth surface up to the ionosphere. The current wave (3.3.40) plays the role of a source injecting field-aligned currents into the magnetosphere. By integrating the continuity equation $\nabla \cdot \vec{j} = 0$ within the dynamo layer we obtain:

$$j_z|_{Z=Z_1} = - \int_{-\infty}^{Z_1} (\partial j_X / \partial x) dz = - \partial I_X / \partial x = -k_X I_* \sin(\omega t - k_X x + \psi). \quad (3.3.41)$$

The field aligned current propagates through the magnetosphere as an Alfvén mode,

$$\frac{\partial^2}{\partial z^2} j_z - V_A^{-2} \frac{\partial^2}{\partial t^2} j_z = 0, \quad (3.3.42)$$

V_A being the Alfvén velocity. The electric current distribution (3.3.41) is a boundary condition for the equation (3.3.42). The similar condition is imposed at the opposite end of the magnetic line of force, whence it follows that the I_x component of the dynamo current is reproduced in the conjugate ionosphere without alterations.

Turning back to the model assumptions let us discuss item 3). The research station *Akademik Vernadsky* lies at the foot of the magnetic line $L = 2.4$. The line of force connecting *Vernadsky* with the Northern hemisphere is almost 40 000 km long, which is much less than the Alfvén wavelength corresponding to periods about one hour. Thus, the entire current system of Fig. 3.3.12 is in the near-field zone of the source, (3.3.41). Accordingly, neither the nonuniformity of the magnetosphere, nor the $V_A = V_A(z)$ dependence of the Alfvén velocity play any substantial part. In fact, solution of the wave equation has been replaced by analysis of an electric circuit whose current contours obey the Kirchhoff law of currents. The assumption of point 4) concerning applicability of the ideal magnetohydrodynamics suggests neglecting the attenuation which is present in the real current contour, and loss of information on some finer effects, like slow (loaded) hydromagnetic waves in the ionosphere [Sorokin and Fedorovich, 1982].

It should be noted that the communication channel connecting pressure variations in one hemisphere to magnetic field pulsations in the other is symmetric. If a magnetic response to atmospheric weather variations at *Vernadsky* can be observed in the Boston area, then weather disturbances near Boston can be observable at *Vernadsky* through magnetic pulsations too. In both cases the geomagnetic variation exists along the entire line of force, while the AGW at one end only.

4 RECOVERING THE CHARACTERISTICS OF FIELD SOURCES AND WAVE GUIDING STRUCTURES

4.1 Recovering the parameters of ULF micropulsations from polarization measurements

This subsection of the Project Report is dedicated to polarization properties of the Pc3 – Pc4 geomagnetic pulsations (time periods 10 to 45 s and 45 to 150 s, respectively) recorded at *Akademik Vernadsky*, in particular to diurnal variations in the horizontal-plane orientation angle of the polarization ellipse. Geomagnetic field measurements at the station were performed with a three-component magnetometer, following the methodology described in Subsection 2.1 of this Report. The physical mechanisms that may contribute to diurnal variations of the ULF wave polarization belong to two categories. One features changes with time in the angular spectrum of the waves incident on the ionosphere, in other words, variations of the effective source of hydromagnetic disturbances in the magnetosphere. The other stresses variations in the transverse ionospheric conductivities that control wave reflection and mode conversion at the ionosphere – neutral atmosphere interface [Saka et al., 1980; Itonaga and Kitamura, 1993; Sinitsin et al., 1999]. The effectiveness of both kinds of mechanisms in the formation of the time run of polarization is analyzed in the Report through numerical simulation.

4.1.1 Experimental data

The magnitudes followed were two parameters of the polarization ellipse, namely the orientation angle of the major semi-axis (counted from the equatorward meridional direction) and the ellipticity ratio. The angle was considered positive if the semi-axis rotated toward the East. The ellipticity ratio (defined as the minor-to-major axis length ratio) also was introduced as a sign dependent magnitude. It was positive if the horizontal-plane magnetic vector component rotated in the counter-clockwise direction. It should be noted that the \vec{H} vector rotated predominantly counter-clockwise in the Southern hemisphere (while clockwise in the North) and the absolute magnitude of the day-time ratio was often close to zero. During data processing and numerical simulation of the polarization variations attention was centered mostly on the orientation angle and its diurnal variations. Analysis of the great amount of data obtained at *Akademik Vernadsky* has allowed identifying two distinct types of behavior of the horizontal-plane magnetic polarization ellipse. One can be described as daytime rotation whereby the major axis follows the visible azimuthal position of the Sun on the celestial sphere. This ‘sunflower’ effect was first discovered for Pc4 pulsations in

the Antarctic region [Zalizovski et al., 2000], see Fig. 4.1.1. The other type of polarization variations is rotation of the major axis counter the apparent solar motion during morning hours and appearance of a characteristic 'arch' in the 'angle – local time' plane in the afternoon (Fig.4.1.2). This run is observed for day-time resonance pulsations only.

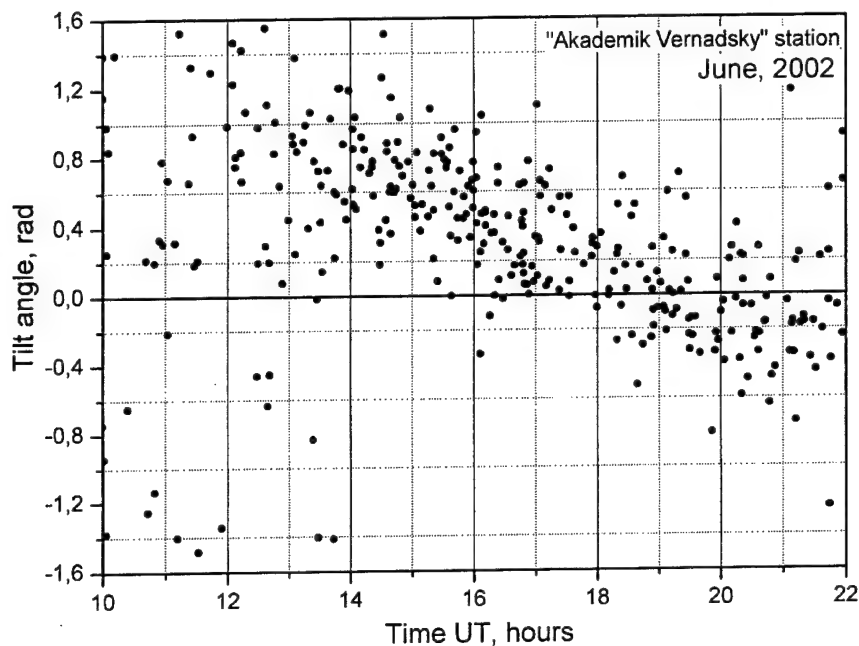


Fig. 4.1.1 Diurnal variation in the orientation angle of the polarization ellipse of pulsations: June, 2002

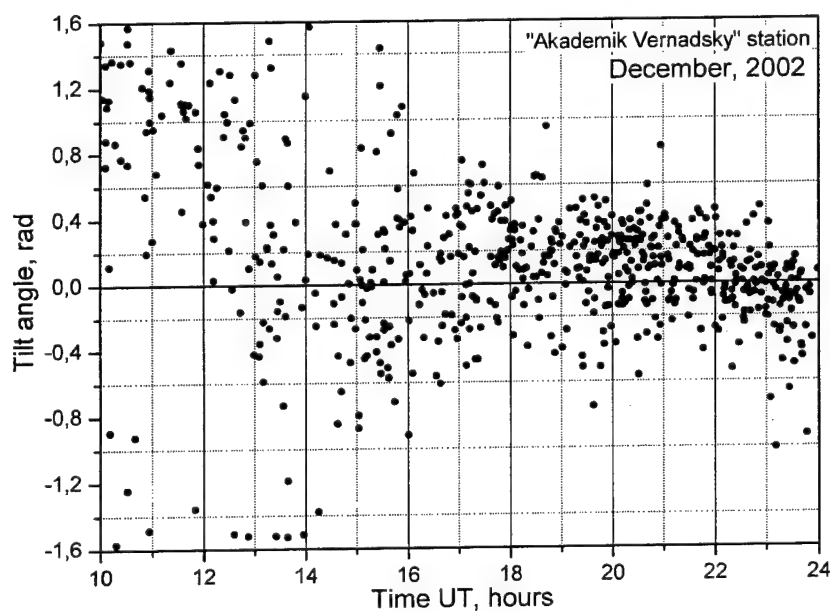


Fig. 4.1.2 Diurnal variation in the orientation angle of the polarization ellipse of pulsations:
December, 2002

The long period observations of 1999 to 2003 in Antarctica provided material for studying the seasonal behavior of diurnal variations in polarization parameters. In Antarctica, the diurnal pattern of the ‘arch’ kind seems to appear mainly in summer and in periods of low geomagnetic activity (Figs.4.1.2 and 2.1.2). It was not observed in winter, at least at frequencies between 10 and 100 mHz, which is in a contrast with the ‘sunflower’ that can appear in any season. In winter it represents the only type of non-random diurnal variations of polarization. The summertime appearance probability of the ‘sunflower’ is higher for periods of higher geomagnetic activity. It should be noted that the ‘sunflower’ is observable in a wide frequency range, much wider than the band of Pc3 – Pc4 resonance events.

4.1.2 Numerical analysis

The analysis was performed in the framework of the theoretical model presented in Subsection 3.1. The E-region conductivities were calculated after the data of real vertical sounding of the ionosphere at *Vernadsky*. The electron concentration N_0 at the layer peak and the peak height h_m were determined from ionograms for each one-hour interval on the day of measurements. The height profile $N_e(h)$ was approximated to by the Chapman layer formula

$$N_e(h) = N_0 \exp \left[\frac{1}{2} \left(1 - \frac{h - h_m}{H} - \exp \left(- \frac{h - h_m}{H} \right) \right) \right], \quad (4.1.1)$$

where H is the scale height (the value used in the computations was 8 km). The height profiles of specific Pedersen and Hall conductivities,

$$\sigma_P = e^2 N_e(z) \left[\frac{\nu_e}{m(\Omega_e^2 + \nu_e^2)} + \frac{\nu_{in}}{M(\Omega_i^2 + \nu_{in}^2)} \right],$$

$$\sigma_H = e^2 N_e(z) \left[\frac{\Omega_e}{m(\Omega_e^2 + \nu_e^2)} + \frac{\Omega_i}{M(\Omega_i^2 + \nu_{in}^2)} \right]$$

were constructed, based on $N_e(h)$ and literature data on the ion composition and collision frequency profiles of the ionosphere [Gurevich and Schwartzburg, 1973]. The height-integrated conductivities $\Sigma_{P,H} = \int \sigma_{P,H} dz$ were averaged over one-hour intervals through the ten-day cycle near the autumn equinox.

When calculating the spatial structure of the ULF wave field at the observation point, it was assumed that the MHD wave beam arriving to the anisotropic surface $z = 0$ (see Fig.3.1.1) from the

magnetosphere consisted of two discrete modes, namely one alfvénic and one magnetosonic wave, cf. (3.1.2). The aim of the numerical analysis is to identify such parameters of the incident hydromagnetic disturbance (the amplitude ratio A_a/A_f and the wavenumbers $p_{1,2}$ and $q_{1,2}$) that would allow reproducing the observed behavior of polarization parameters on the ground. The time-varying E-region conductivities used in the model were calculated, based on real data of vertical ionospheric sounding at 'Vernadsky' and literature data on collision frequencies. One immediate important result of the numerical experimentation was that the polarization structures observed could be simulated only with allowance for both transverse and compressional modes. The computations could be brought to agreement with the measurements solely with $A_a/A_f \approx 1$. With respect to the directions of wave arrival (transverse wave vector components p and q), two model scenarios were considered. First it was assumed that the wavenumbers of both incident modes remained constant throughout the day, hence variations in the polarization parameters could only result from changes with time of the ionospheric conductivities. The time run of the major axis orientation predicted for this case is shown in Fig.4.1.3 (the scatter of calculated points in the Figure, referred to as noise, reflects presence in the model of uniformly distributed random fluctuations of conductivity). As can be seen, the simulated behavior of the orientation angle resembles closely the 'arch' pattern observed in the experiment. The similarity remains noticeable as long as the angle of incidence of the fast mode is 10 to 20 degrees steeper than the local dip angle of the geomagnetic field (about 57 degrees at Vernadsky), while the Alfvén wave travels along. The components of the wave vector p which are perpendicular to the plane of magnetic meridian ('azimuthal' components) are close to zero.

The other numerical experiment addressed the effect of angle of arrival variations in the compressional (fast) mode, simulating the East to West motion of the wave source. The incident Alfvén wave remained 'tied' to the magnetic line of force. Once again the amplitude ratio was $A_a/A_f \approx (1 \text{ to } 1.2)$, however the resulting behavior of the orientation angle resembled more of the 'sunflower' than the 'arch' (see Fig.4.1.4).

The plane-layered model of the plasma environment has enabled determining the full spatial structure of MHD waves above the reflecting surface, and hence the direction that the MHD waves arrive from. In its turn, this estimate can be used for positioning the effective source of magnetoacoustic modes in the magnetosphere, which task demands that we go beyond the limits set for the plane layered model. Its validity is limited by heights about 500 km above the Earth's surface. While the rigorous approach would require application of complex environmental models, accounting for excitation of the magnetospheric MHD resonance cavities, the spatial spectrum of hydromagnetic waves in the upper halfspace that has been found in the plane model enables

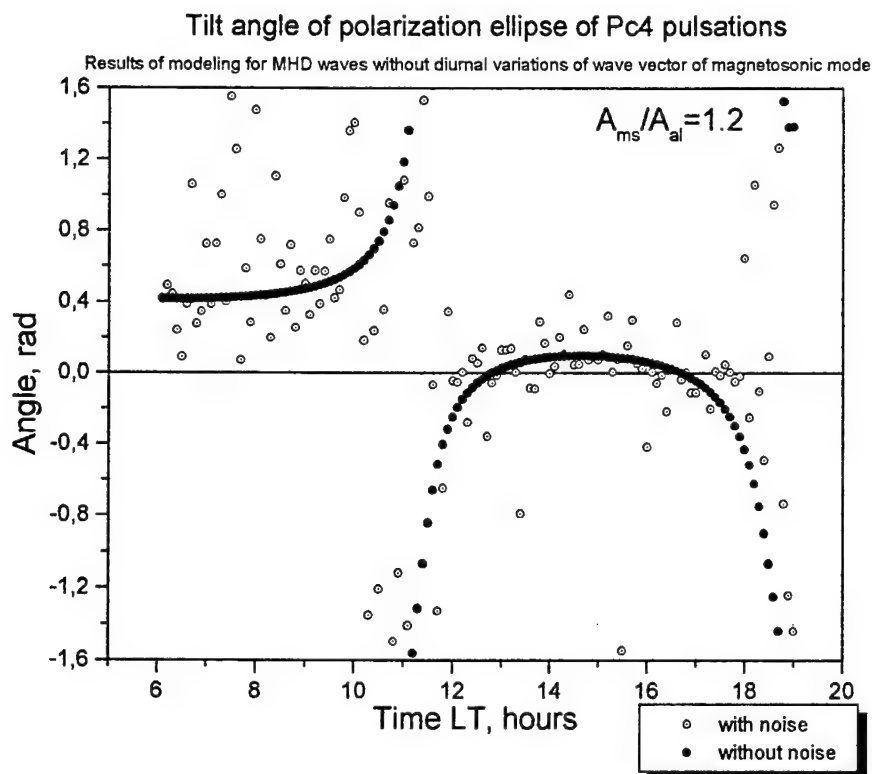


Fig. 4.1.3 Simulated diurnal variation in the orientation angle of the polarization ellipse of pulsations:
Assumption of a fixed spatial spectrum of MHD waves during the day

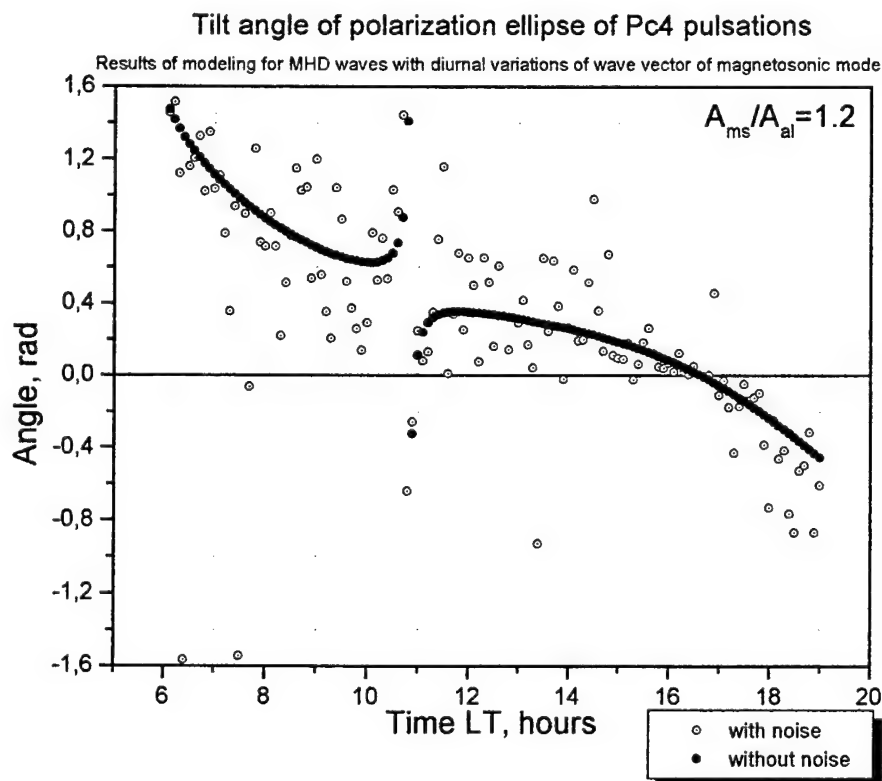


Fig. 4.1.4 Simulated diurnal variation in the orientation angle of the polarization ellipse of pulsations:
Assumption of a varying azimuthal wave vector projection in the magnetoacoustic mode

concluding even now that magnetoacoustic modes arrive from higher L-levels than that of the observation point. This conclusion is supported by results of ray tracing in a global model involving a nonuniform profile of the Alfvén velocity (Fig.4.1.5).

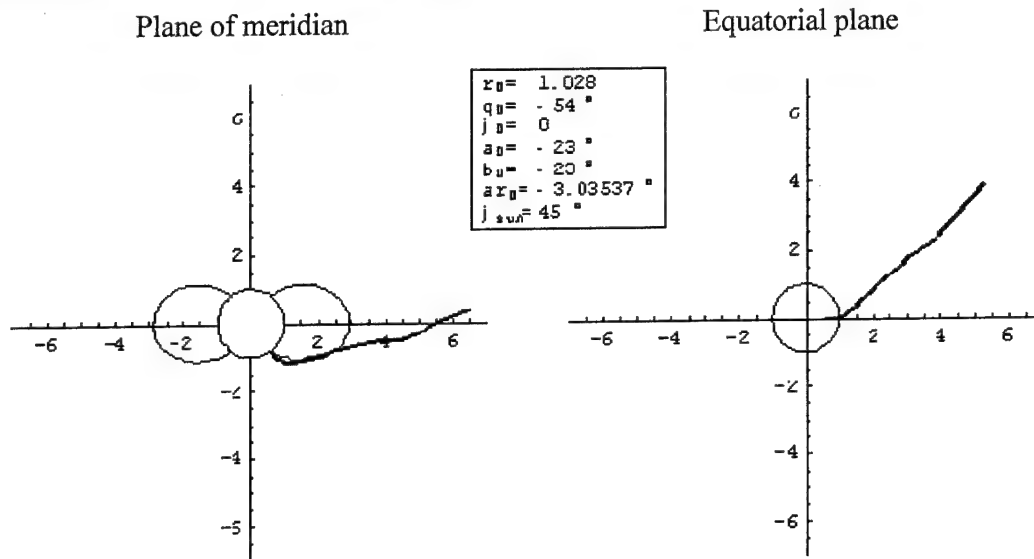


Fig.4.1.5 Magnetoacoustic ray trajectories calculated within the meridional and azimuthal planes.

Thus, for geomagnetic pulsations of magnetospheric origin both types of polarization variations have been given a physical explanation in terms of hydromagnetic wave propagation through the set of coupled resonant structures. The hydromagnetic power from a source at the outer boundary of the magnetosphere can be transported to lower L-shells solely by a compressional wave (fast magnetosonic) which propagates at an arbitrary angle to the external magnetic field. The Alfvén wave appears as a result of reflection/conversion of the primary wave at the ionospheric boundary and then travels to the conjugate ionosphere. If the cross-field conductivities at both ends of the line of force are sufficiently high, then conditions exist for the onset of field line resonances (FLR), and the field structure depends primarily on conductivity variations in the two ionospheres, while being nearly independent of the motion of the subsolar point (this results in the 'arch' pattern of the orientation angle).

In case the Q-factor of the field-line resonator is low, or the excitation frequency of the pulsation is too different from the FLR frequency, the polarization variations are largely controlled by the motion of the effective magnetosonic source, such that the diurnal run of the ellipse orientation can be described as the 'sunflower rotation'.

The angles of incidence on the ionosphere are 23° above the geomagnetic field vector in the plane of meridian and -23° in the azimuthal plane (the azimuth of the subsolar point on the magnetopause is 45°).

4.2 Recovering parameters of the world thunderstorm activity and of the Earth-ionosphere cavity from the data of ELF monitoring at the Antarctic station Akademik Vernadsky

The theoretical analysis of Subsection 3.2 will be employed here to solve the inverse problem of polarization diagnostics at *Vernadsky* of the ELF noise excited by global thunderstorms. First, let us specify the model parameters. We assume the world thunderstorm activity to be supported by joint action of the three equatorial ($\theta_j = \pi/2$) thunderstorm centers mentioned in Subsection 3.2, namely

1) the African, $\varphi_1 \approx 25^\circ$,

2) the East Asian, $\varphi_2 \approx 115^\circ$,

and 3) the South American, $\varphi_3 \approx -65^\circ$,

where φ_j is longitude with respect to the Greenwich meridian. The respective coordinates of the Antarctic station are $\theta = 154.27^\circ$ and $\varphi = -65.25^\circ$. A closer look at these figures reveals that the geometry of relative locations of the thunderstorm centers is rather special. Namely, the East Asian and the South American centers are separated from the African center by roughly equal angular distances $|\varphi_{2,3} - \varphi_1| \approx \pi/2$ along the longitude. As a result, the two centers lie at practically opposite points of the equator. Together with an arbitrary observation point on the Earth surface, they belong to the same great circle, such that the approximate equation holds $\vartheta_2 + \vartheta_3 \approx \pi$. In the case of *Vernadsky*, another special feature of the geometric layout is that *Vernadsky's* longitude is nearly equal to that of the South American thunderstorm center. So, the longitude parameters of the model are

$$\varphi - \varphi_1 \approx -\pi/2; \quad \varphi - \varphi_2 \approx -\pi; \quad \varphi - \varphi_3 \approx 0. \quad (4.2.1)$$

Upon linearization in $\Delta\varphi^{(p)}$ and summation over $j = 1, 2, 3$, equations (3.2.41 – 3.2.44), (3.2.39), (3.2.51) and (4.2.1) yield

$$\begin{aligned} I(\omega^{(p)}, t) = \sum_{j=1}^3 I_j(\omega^{(p)}, t) \approx & \left[\frac{c^2(2p+1)}{8\pi a^3 h \omega^{(p)} \Omega} \right]^2 \left\{ \left| \tilde{M}_1(t) \right|^2 > \left[P'_p(\cos \vartheta_1) \right]^2 + \right. \\ & + \left(\left| \tilde{M}_2(t) \right|^2 > + \left| \tilde{M}_3(t) \right|^2 > \right) \left[P'_p(\cos \vartheta_2) \right]^2 \cos^2 \theta \left. \right\} + \\ & + 2\Delta\varphi^{(p)} \left[\frac{c^2(2p+1)}{8\pi a^3 h \omega^{(p)} \Omega} \right]^2 < \left| \tilde{M}_1(t) \right|^2 > P'_p(\cos \vartheta_1) P''_p(\cos \vartheta_1) \sin \theta, \end{aligned} \quad (4.2.2)$$

$$\begin{aligned}
I(\omega^{(p)}, t) = \sum_{j=1}^3 I_j(\omega^{(p)}, t) \approx & \left[\frac{c^2(2p+1)}{8\pi a^3 h \omega^{(p)} \Omega} \right]^2 \left\{ \left| \tilde{M}_1(t) \right|^2 > [P'_p(\cos \vartheta_1)]^2 + \right. \\
& + \left(\left| \tilde{M}_2(t) \right|^2 > + \left| \tilde{M}_3(t) \right|^2 > \right) [P'_p(\cos \vartheta_2)]^2 \cos^2 \theta \Big\} + \\
& + 2\Delta\varphi^{(p)} \left[\frac{c^2(2p+1)}{8\pi a^3 h \omega^{(p)} \Omega} \right]^2 < \left| \tilde{M}_1(t) \right|^2 > P'_p(\cos \vartheta_1) P''_p(\cos \vartheta_1) \sin \theta,
\end{aligned} \quad (4.2.2)$$

$$\begin{aligned}
Q(\omega^{(p)}, t) = \sum_{j=1}^3 Q_j(\omega^{(p)}, t) \approx & \left[\frac{c^2(2p+1)}{8\pi a^3 h \omega^{(p)} \Omega} \right]^2 \left\{ \left| \tilde{M}_1(t) \right|^2 > [P'_p(\cos \vartheta_1)]^2 - \right. \\
& - \left(\left| \tilde{M}_2(t) \right|^2 > + \left| \tilde{M}_3(t) \right|^2 > \right) [P'_p(\cos \vartheta_2)]^2 \cos^2 \theta \Big\} + \\
& + 2\Delta\varphi^{(p)} \left[\frac{c^2(2p+1)}{8\pi a^3 h \omega^{(p)} \Omega} \right]^2 < \left| \tilde{M}_1(t) \right|^2 > P'_p(\cos \vartheta_1) P''_p(\cos \vartheta_1) \sin \theta,
\end{aligned} \quad (4.2.3)$$

$$\begin{aligned}
U(\omega^{(p)}, t) = \sum_{j=1}^3 U_j(\omega^{(p)}, t) \approx \\
\approx 2\Delta\varphi^{(p)} \cos \theta \left[\frac{c^2(2p+1)}{8\pi a^3 h \omega^{(p)} \Omega} \right]^2 \left\{ \left| \tilde{M}_1(t) \right|^2 > [P'_p(\cos \vartheta_1)]^2 - \right. \\
\left. - \left(\left| \tilde{M}_2(t) \right|^2 > + \left| \tilde{M}_3(t) \right|^2 > \right) [P'_p(\cos \vartheta_2)]^2 \right\},
\end{aligned} \quad (4.2.4)$$

and

$$\begin{aligned}
V(\omega^{(p)}, t) = \sum_{j=1}^3 V_j(\omega^{(p)}, t) \approx \\
\approx -2\Delta\varphi^{(p)} \cos \theta \left[\frac{c^2(2p+1)}{8\pi a^3 h \omega^{(p)} \Omega} \right]^2 \left\{ \left| \tilde{M}_1(t) \right|^2 > [P'_p(\cos \vartheta_1)]^2 + \right. \\
\left. + \left(\left| \tilde{M}_2(t) \right|^2 > + \left| \tilde{M}_3(t) \right|^2 > \right) [P'_p(\cos \vartheta_2)]^2 \right\}.
\end{aligned} \quad (4.2.5)$$

These are Stokes parameters of the ELF noise excited by the world thunderstorms at Schumann resonance frequencies $\omega^{(p)}$ and detected at *Akademik Vernadsky* in Antarctica. Use has been made of the relation $[P'_p(\cos \vartheta_3)]^2 \approx [P'_p(\cos(\pi - \vartheta_2))]^2 = [P'_p(\cos \vartheta_2)]^2$ and the notation

$P''_p(x) \equiv \frac{d^2}{dx^2} P_p(x)$. It can be seen from (4.2.2) to (4.2.5) that the contributions of the

thunderstorm center $j=2$ and $j=3$ cannot be resolved in principle because of the above mentioned special character of their mutual positioning. On the other hand, by combining the

Stokes parameters into $I \pm Q$ and $U \pm V$ one can easily separate the total intensity

$\langle |\tilde{M}_2(t)|^2 \rangle + \langle |\tilde{M}_3(t)|^2 \rangle$ from $\langle |\tilde{M}_1(t)|^2 \rangle$, viz.

$$\begin{aligned} I(\omega^{(p)}, t) + Q(\omega^{(p)}, t) &= \\ &= 2 \left[\frac{c^2(2p+1)}{8\pi a^3 h \omega^{(p)} \Omega} \right]^2 \langle |\tilde{M}_1(t)|^2 \rangle + P'_p(\cos \vartheta_1) \{ P''_p(\cos \vartheta_1) + 2\Delta\varphi^{(p)} P''_p(\cos \vartheta_1) \sin \theta \}, \end{aligned} \quad (4.2.6)$$

$$\begin{aligned} I(\omega^{(p)}, t) - Q(\omega^{(p)}, t) &= \\ &= 2 \left[\frac{c^2(2p+1)}{8\pi a^3 h \omega^{(p)} \Omega} \right]^2 \left(\langle |\tilde{M}_2(t)|^2 \rangle + \langle |\tilde{M}_3(t)|^2 \rangle \right) [P'_p(\cos \vartheta_2)]^2 \cos^2 \theta, \end{aligned} \quad (4.2.7)$$

$$\begin{aligned} U(\omega^{(p)}, t) + V(\omega^{(p)}, t) &= \\ &= -4\Delta\varphi^{(p)} \left[\frac{c^2(2p+1)}{8\pi a^3 h \omega^{(p)} \Omega} \right]^2 \left(\langle |\tilde{M}_2(t)|^2 \rangle + \langle |\tilde{M}_3(t)|^2 \rangle \right) [P'_p(\cos \vartheta_2)]^2 \cos \theta, \end{aligned} \quad (4.2.8)$$

$$\begin{aligned} U(\omega^{(p)}, t) - V(\omega^{(p)}, t) &= \\ &= 4\Delta\varphi^{(p)} \left[\frac{c^2(2p+1)}{8\pi a^3 h \omega^{(p)} \Omega} \right]^2 \langle |\tilde{M}_1(t)|^2 \rangle [P'_p(\cos \vartheta_1)]^2 \cos \theta. \end{aligned} \quad (4.2.9)$$

After some algebra with (4.2.7) - (4.2.9), it is possible to determine the 'apparent' longitudinal shift of the thunderstorm centers as observed at an arbitrary resonance frequency $\omega^{(p)}$,

$$\Delta\varphi^{(p)}(t) = - \left(\frac{\cos \theta}{2} \right) \frac{U(\omega^{(p)}, t) + V(\omega^{(p)}, t)}{I(\omega^{(p)}, t) - Q(\omega^{(p)}, t)}. \quad (4.2.10)$$

All of these equations are simplified additionally for the first Schumann resonance at $\omega = \omega^{(1)}$, since $P'_p(\cos \vartheta_j) = 1$ and $P''_p(\cos \vartheta_j) = 0$. In this case (4.2.6) and (4.2.7) can be used to determine

time dependences of individual center intensities, $\langle |\tilde{M}_1(t)|^2 \rangle$ and, $\langle |\tilde{M}_2(t)|^2 \rangle + \langle |\tilde{M}_3(t)|^2 \rangle$ as

well as the integral intensity of global thunderstorms, $\langle |\tilde{M}(t)|^2 \rangle \equiv \sum_{j=1}^3 \langle |\tilde{M}_j(t)|^2 \rangle$,

$$\langle |\tilde{M}_1(t)|^2 \rangle = \frac{1}{2} \left(\frac{8\pi a^3 h \omega^{(1)} \Omega}{3c^2} \right)^2 [I(\omega^{(1)}, t) + Q(\omega^{(1)}, t)], \quad (4.2.11)$$

$$\left\{ \langle |\tilde{M}_2(t)|^2 \rangle + \langle |\tilde{M}_3(t)|^2 \rangle \right\} = \frac{1}{2 \cos^2 \theta} \left(\frac{8\pi\alpha^3 h \omega^{(i)} \Omega}{3c^2} \right)^2 [I(\omega^{(i)}, t) - Q(\omega^{(i)}, t)]. \quad (4.2.12)$$

$$\begin{aligned} \langle |\tilde{M}(t)|^2 \rangle &\equiv \sum_{j=1}^3 \langle |\tilde{M}_j(t)|^2 \rangle = \\ &= \frac{1}{2 \cos^2 \theta} \left(\frac{8\pi\alpha^3 h \omega^{(i)} \Omega}{3c^2} \right)^2 \{ I(\omega^{(i)}, t) (1 + \cos^2 \theta) - Q(\omega^{(i)}, t) \sin^2 \theta \} \end{aligned} \quad (4.2.13)$$

Besides, (4.2.6) and (4.2.9) provide an alternative estimate for $\Delta\varphi^{(i)}(t)$ (other than (4.2.10)), viz.

$$\Delta\varphi^{(i)}(t) = \left(\frac{1}{2 \cos \theta} \right) \frac{U(\omega^{(i)}, t) - V(\omega^{(i)}, t)}{I(\omega^{(i)}, t) + Q(\omega^{(i)}, t)}. \quad (4.2.14)$$

The knowledge of $\Delta\varphi^{(i)} = 0.75 \frac{\rho}{1 + \sqrt{1 + \rho^2}}$ (see Subsection 3.2) will allow evaluating both the gyrotropy parameter ρ at the ionospheric wall $z = h$ of the cavity,

$$\rho(h) \equiv \omega_H / \nu_{\text{eff}}(h) \approx (8/3) \Delta\varphi^{(i)}, \quad (4.2.15)$$

and the cavity height h , based on the adopted magnitude of the electron gyrofrequency in the lower ionosphere, $\omega_H \approx 8.4 \cdot 10^6 \text{ s}^{-1}$, and literature models of the collision frequency profile $\nu_{\text{eff}} = \nu_{\text{eff}}(z)$.

The theoretical results presented in this Subsection have been used for solving the inverse problem of radio diagnostics of world thunderstorm centers and the gyrotropic Earth-ionosphere cavity. The diagnostics proceeds from the ELF polarization measurements that were performed at *Akademik Vernadsky* in March, 2002 through January, 2003. The corresponding processing procedures are discussed in Subsection 2.2.

First, the observational data and theoretical equations (4.2.11) to (4.2.13) were used to determine diurnal variations in the intensity of individual centers, and thus in the integral intensity of the global thunderstorm activity. Fig.4.2.1 shows intensity variations as the activity is re-distributed between the centers both during the day and on the month-to-month scale. The intensity peaks about 15:00 UT are associated with the activity of the African center; at 8:00 UT with the West Asian center, and at 20:00 UT with the South American center.

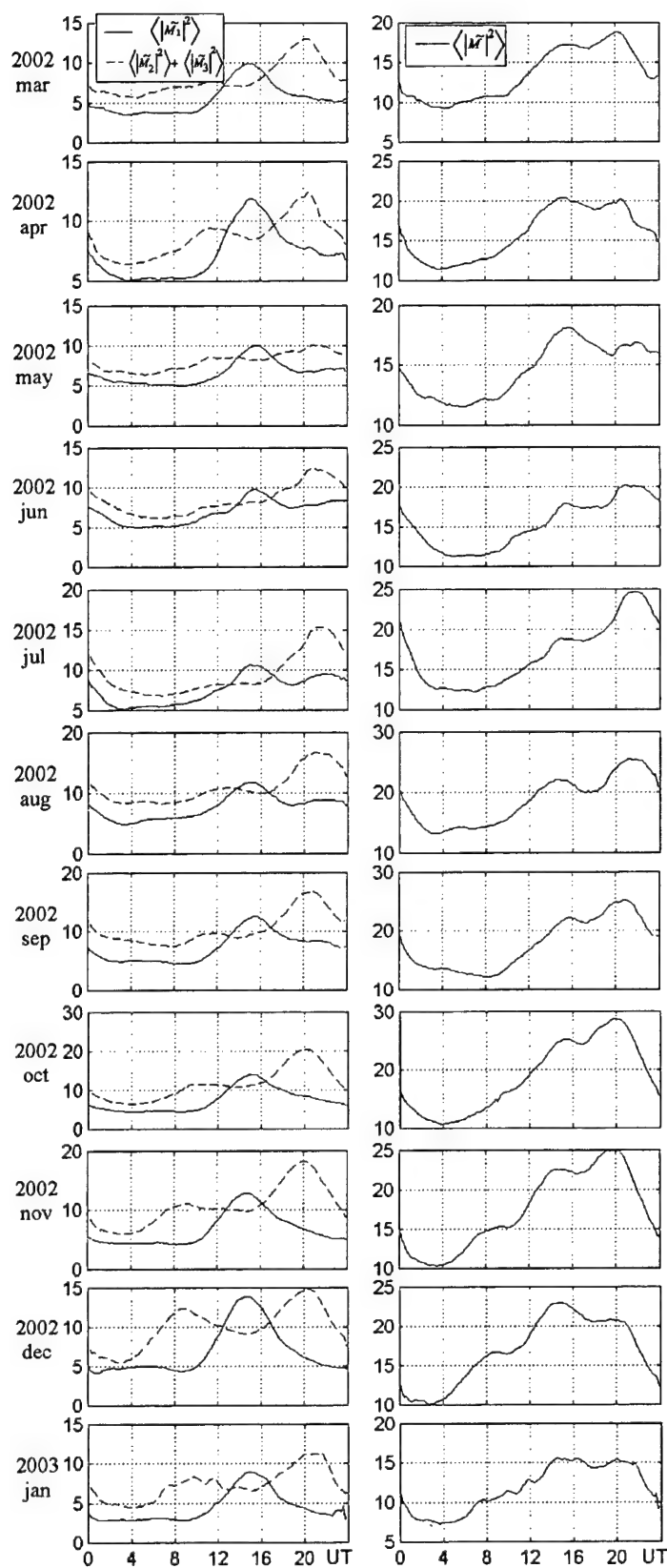


Fig. 4.2.1 Estimated diurnal variations in the intensity of the African thunderstorm center $\langle |M_1|^2 \rangle$; East Asian with South American centers, $\langle |M_2|^2 \rangle + \langle |M_3|^2 \rangle$, and in the integral global thunderstorm activity: March, 2002 to January, 2003.

To compare quantitatively the intensities of individual thunderstorm centers and seasonal variations of their activity, diurnal averages were estimated of the respective magnitudes, i.e. $\overline{<|M_1|^2>}$, $\overline{<|M_2|^2>}$ and $\overline{<|M_3|^2>}$ and $\overline{<|M|^2>}$ (the bar above the value denotes time averaging over the period 00 UT to 24 UT). The results are shown in Fig.4.2.3 a. The summarized intensity of the East Asian and South American centers can be seen to exceed the African center intensity in all seasons through the year. In fact, it is greater by a factor of 2 or more between August and December.

Fig. 4.2.2 presents the 'apparent' longitudinal shifts $\Delta\varphi^{(1,2)}$ of the thunderstorm centers as seen at two lower-order resonance frequencies, $f^{(1)} = 8\text{Hz}$ and $f^{(2)} = 14\text{Hz}$.

The 'two halves of a hedgehog' geomagnetic field model that we have used in the theory does not give grounds to expect faster variations in $\Delta\varphi^{(1,2)}(t)$ than diurnal. Meanwhile, the measured data reveal a pronounced 12-hour harmonic, particularly bright at $f^{(1)} = 8\text{Hz}$. We ascribe this to the approximate character of the theoretical model developed, and hence regard the effect as an error of $\Delta\varphi^{(1,2)}$ estimation.

We have computed daily averages $\overline{\Delta\varphi^{(1,2)}}$ for every month and standard deviations of the values, $\sqrt{[\delta(\Delta\varphi^{(1,2)})]^2}$, to estimate the error. The relative error varied through the year between 10% (in October) and 22% (in December), with the mean level equal to 15%. As for the ratio $\overline{\Delta\varphi^{(2)}}/\overline{\Delta\varphi^{(1)}}$, it varied between 0.24 in January and 0.54 in May. The yearly mean was 0.37, which is reasonably close to the model magnitude of 0.41 (cf. Subsection 3.2). The 'apparent' longitudinal shift $\Delta\varphi^{(1)}$ shows a pronounced seasonal run (see Fig. 4.2.3 b) with a maximum value about 15° (August) and minimum of 11° (January).

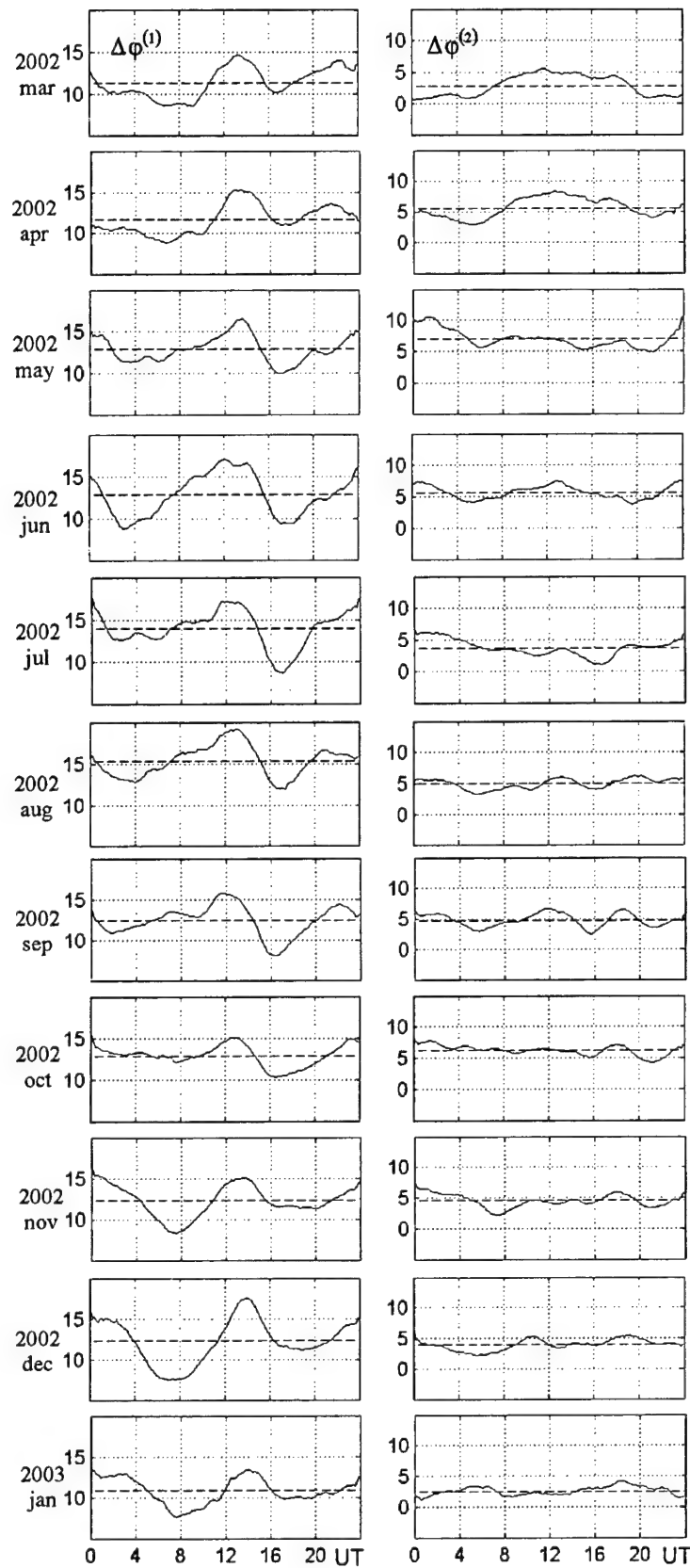


Fig. 4.2.2 Estimated diurnal variations of the “apparent” longitudinal shifts, $\Delta\phi^{(1,2)}(t)$, of thunderstorm center for the Schumann resonances $f^{(1)} = 8\text{ Hz}$ and $f^{(2)} = 14\text{ Hz}$: March, 2002 to January, 2003.

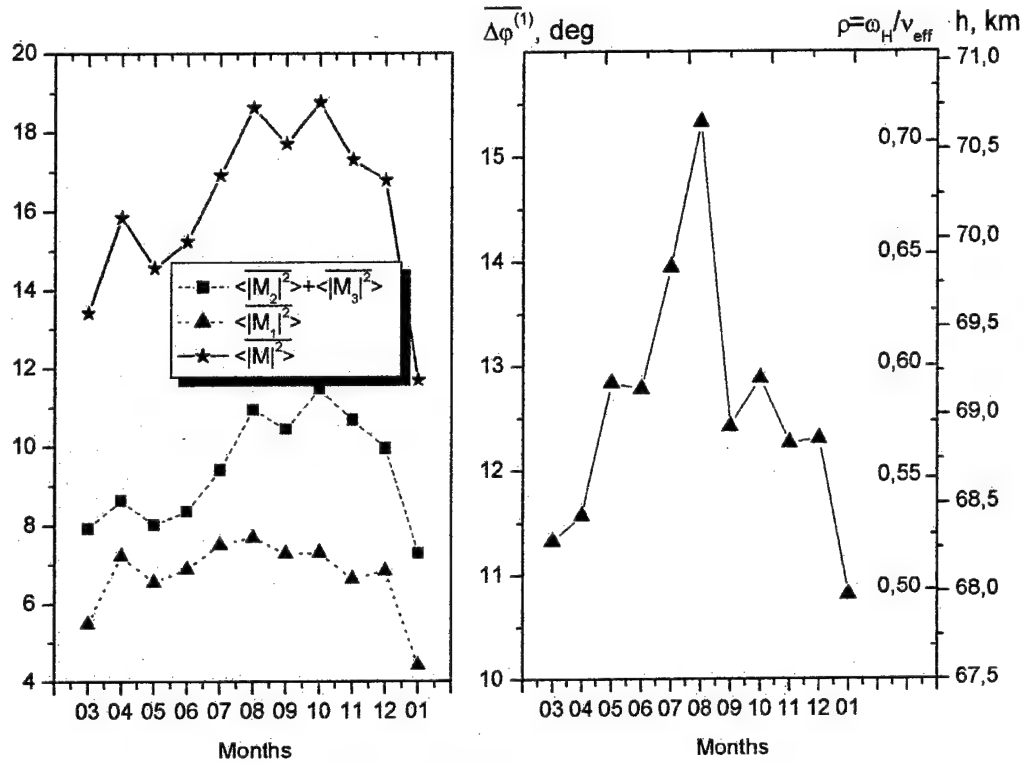


Fig.4.2.3 Estimated seasonal variations in March, 2002 to January, 2003, of

a) daily mean intensities of individual thunderstorm centers, $\langle |M_1|^2 \rangle$ and $\langle |M_2|^2 \rangle + \langle |M_3|^2 \rangle$, and integral thunderstorm intensity, $\langle |M|^2 \rangle$;

b) daily mean values of the “apparent” longitudinal shift $\Delta\phi^{(1)}$ of thunderstorm centers at $f^{(1)} = 8\text{Hz}$ (left-hand scale along the vertical axis), and gyrotropy parameter, ρ , and effective channel height, h (two respective right-hand scales along the vertical).

According to (4.2.15), this shift is linearly related to the magnitude of the gyrotropy parameter ρ at the upper edge $z = h$ of the propagation channel. This permits using the curve of Fig.4.2.3 b to evaluate the seasonal behavior of both ρ and h . To that end, the vertical axis in Fig.4.2.3 b has been provided with three scales, of which the two on the right side have been calibrated in the units of ρ and h . The $\rho - h$ relation can be established from the familiar model $v_{eff} = v_{eff}(z)$ of the electron collision frequency [Bliokh et al., 1980] which is nearly linear at the altitudes of 65 to 75 km. As can be seen from the figure, the growth in the ‘apparent’ shift $\Delta\phi^{(1)}$ noted for the January – August period is accompanied by a similar increase of the gyrotropy parameter ρ (from 0.5 to 0.7) and effective height of the cavity (from 68 km to nearly 71 km).

4.3 Recovering sea wave parameters from the data of bistatic HF radio sounding

Experimental and theoretical investigations of HF radio wave scattering by the rough sea surface started more than half a century ago. Over that time a physical interpretation was offered for the majority of features in the signal spectra, and their relation to the sea surface condition specified. It became possible to solve the inverse problem (though through the use of special dedicated radars only), i.e. to recover some of oceanographic parameters from the analysis of the radio spectra.

In case a HF receiver were located right near the sea surface, it would receive ionospherically propagated signals, e.g. from broadcasting radios, and the same signals again upon scattering by the sea surface. Owing to the high frequency stability of modern transmitters it is possible to organize, in a close vicinity of the carrier, a high-resolution analysis of variations in the signal spectral components resulting from resonant scattering by the gravitation component of sea roughness. Thus, we are technically in a position to make use of nondedicated radiation in the special application like radio oceanography over large areas on the Earth's surface. First experiments of the kind were carried through in the course of the marine cruise of the 5-th Ukrainian Antarctic mission [Kascheev, et al., 2000].

4.3.1 Measured results

The investigations were continued during the marine part of the 7-th Antarctic expedition, with measurements performed along the path Sevastopol – *Akademik Vernadsky*. Fig. 4.3.1 carries a fragment of the dynamic spectrum received during ship moorage at open sea in the Atlantic. The illuminating frequency was 21 500 kHz and the resolution 0.04 Hz. Three peaks are clearly seen in the figure. The central peak corresponds to the sounding signal. The other two that are constantly present arise from resonant scattering by the sea waves. Each individual instantaneous spectrum is the result of reflection from a random rough surface. To obtain a statistically meaningful result, it would be necessary to perform a *post hoc* incoherent averaging, which is hindered by the slow drift in the frequency domain resulting from ionospheric processes. A special data processing algorithm has been developed to compensate for the drift. Essentially, it consists of averaging the spectral density of the received signal in a band of fixed width about a running peak. Strictly speaking, this approach is not well justified as the ionospheric signal at the receiving antenna might be slightly different from the signal above the sea surface where resonance scattering is formed.

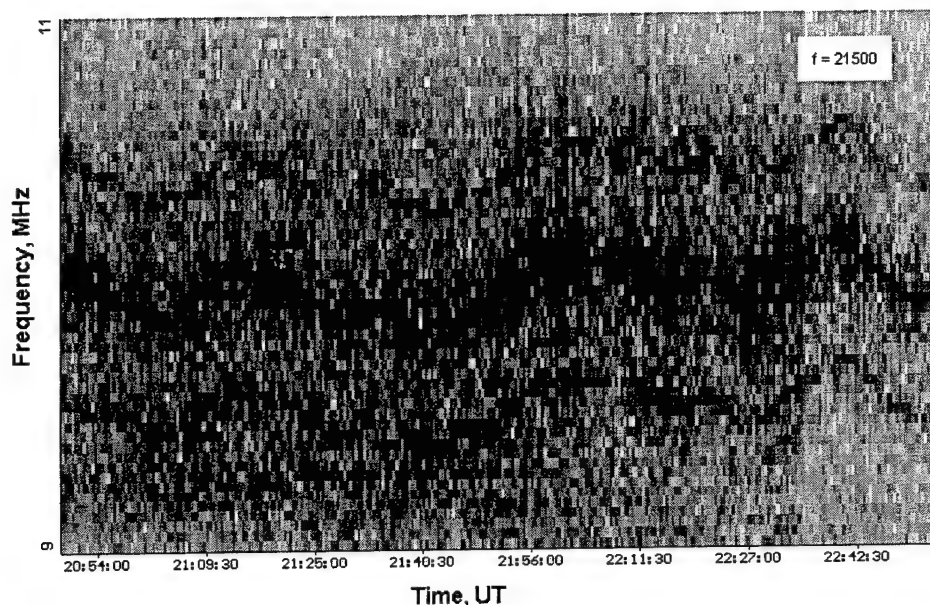


Fig. 4.3.1 Dynamic spectrum of the received signal.

Yet with account of the correlation length of the ionospheric signal (tens of kilometers in the presence of large-scale TIDs – [Galushko, 1984] and size of the effective scattering area on the rough surface (below 20 km, [Kascheev, et al., 2000] the approach might be admissible. An example of processed results is given in Fig. 4.3.2 (curves 1 to 3). The experiment was carried out 24 January, 2002 when the research vessel was anchored in the Atlantic ocean. The surface wind speed initially was about 10m/s, with the direction varying near 60° with respect to the viewing (receiver-transmitter) line. The seas reached 4 on the standard scale. The operating frequency of Radio SGO (Santiago de Chile) was 21.5 MHz and the corresponding Bragg

frequency $F = 0.4728$ Hz. Shown in Fig. 4.3.2 are three spectra averaged over one hour intervals. Each curve in the Figure is the average of six instantaneous spectra. The time lag between the averaging procedures was also equal to one hour. The abscissa is the frequency shift from the ionospheric signal peak, normalized by the Bragg frequency. The frequency resolution was

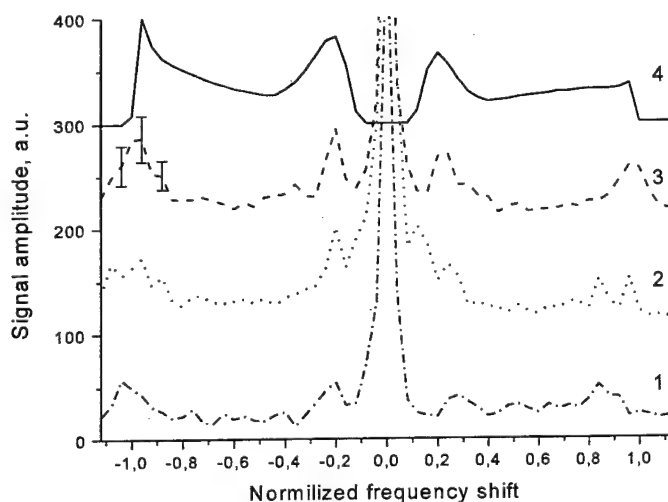


Fig 4.3.2 Statistically averaged spectra of the scattered HF signal

0.0224 Hz (i.e. coherent integration time 51.2 s). The vertical axis represents spectral amplitudes in arbitrary units. To avoid mutual masking, the curves have been separated along the vertical by 100 a.u. The actual peak magnitudes at $F = 0$, due to the illuminating signal, are not shown as they reach beyond the dynamic range adopted.

4.3.2 Theoretical formulation and solution pattern for the scattering problem

To provide an interpretation of the measured data, the radio wave scattering by the sea was analyzed theoretically (within a first order perturbation scheme) for the near-field range of the receive antenna. The electric, \vec{E} and magnetic, \vec{H} , field vectors obeyed impedance-type (Leontovich) simplified boundary conditions at the highly conductive air-water interface, viz.

$$[\vec{N}, \vec{E}] - \eta_0 [\vec{N} [\vec{N}, \vec{H}]] \big|_{z=\zeta(\vec{r}, t)} = 0 \quad (4.3.1)$$

Here η_0 is the small surface impedance, $|\eta_0| \ll 1$; $z = \zeta(\vec{r}, t)$ the random sea surface; $\vec{N} = (\vec{i}_z - \vec{\gamma}) / \sqrt{1 + \gamma^2}$ the external normal to the surface; $\vec{\gamma} = \nabla \zeta(\vec{r}, t)$, and \vec{i}_z the unit vector along the z axis. The scale frequencies characterizing variations in the surface geometry and other parameters are small compared with the electromagnetic wave's frequency ω_0 , such that the problem may be analyzed in the quasistationary approximation. The field source at O_1 (vectorial separation \vec{R}_1 from the scattering site) lies high above the average interface $z = \langle \zeta(\vec{r}, t) \rangle = 0$ in the region of separated spectra [Bass and Fuks, 1975] $kL/R_1 \ll 1$. The inequality is opposite for the observation point O_2 (vectorial separation \vec{R}_2 from the scattering site), $kL/R_2 \gg 1$. Here l is the correlation length of surface irregularities; L the scale size of the illuminated area, and $k = \omega_0/c$ the electromagnetic wave's wavenumber. The average field vectors $\vec{E} = \langle \vec{E} \rangle$ and $\vec{H} = \langle \vec{H} \rangle$ will be determined in the Born approximation (neglecting terms of order $O(\zeta^2)$ in the boundary condition). The first-order conditions for the fluctuating fields, $\vec{e} = \vec{e}_\perp + \vec{i}_z e_z$ and \vec{h} can be written as

$$\vec{e}_\perp - \eta_0 [\vec{i}_z \vec{h}] \big|_{z=0} = -\vec{B}_1 - \vec{B}_2 \equiv -\vec{B}, \quad (4.3.2)$$

with

$$\vec{B}_1 = [\vec{i}_z [\nabla \zeta, \vec{E}]] \big|_{z=0} \text{ and } \vec{B}_2 = -\zeta \left[\vec{i}_z \left[\vec{i}_z \frac{\partial}{\partial z} \vec{E} \right] \right] \big|_{z=0}.$$

Our further analysis will be confined to the case of vertically polarized fields which is of greater practical interest. In view of the condition $kL/R_1 \ll 1$, knowledge of the field sources can be formally replaced by specification of an incident wave,

$$\vec{E}^{(i)} = -G\vec{g}_0 e^{i[\vec{k}_\perp \vec{r} + k_z z - \omega_0 t]}, \quad \vec{H}^{(i)} = G\vec{p}_0 e^{i[\vec{k}_\perp \vec{r} + k_z z - \omega_0 t]}, \quad (4.3.3)$$

with $G = (A/R_1)e^{ikR_1}$, $A = \text{const}$,

$$\begin{cases} k = \vec{k}_\perp + \vec{i}_z k_z, & \vec{k}_\perp = k\vec{\alpha}_\perp, & k_z = k\alpha_z, & \vec{\alpha} = -\vec{R}_1/R_1, \\ \vec{p}_0 = [\vec{i}_z, \vec{\alpha}]/|\vec{i}_z, \vec{\alpha}|, & \vec{g}_0 = [\vec{\alpha}, \vec{p}_0], & \vec{g} = [\vec{\beta}_0, \vec{p}_0], & \vec{\beta}_0 = \vec{\alpha} - 2\vec{i}_z\alpha_z. \end{cases}$$

By introducing the angle of incidence, θ_0 , the wave vectors can be written as $k_\perp = k \sin \theta_0$, $k_z = -k \cos \theta_0$. Let the plane of incidence coincide with the plane $y = 0$. Then

$$\begin{cases} \vec{p}_0 = (0, 1, 0), & \vec{\beta}_0 = (\sin \theta_0, 0, \cos \theta_0), & \vec{\alpha} = (\sin \theta_0, 0, -\cos \theta_0), \\ \vec{g}_0 = (\cos \theta_0, 0, \sin \theta_0), & \vec{g} = (-\cos \theta_0, 0, \sin \theta_0). \end{cases} \quad (4.3.4)$$

The mean scattered field will be sought in the form

$$\begin{Bmatrix} \vec{E}^{(s)} \\ \vec{H}^{(s)} \end{Bmatrix} = \begin{Bmatrix} -\vec{g} \\ \vec{p}_0 \end{Bmatrix} G R_\parallel e^{i(\vec{k}_\perp \vec{r} - k_z z - \omega_0 t)}, \quad (4.3.5)$$

where R_\parallel is the reflection coefficient which can be formally derived when the mean field (a sum of the incident and mean scattered field) is substituted into the boundary condition,

$$R_\parallel = (\cos \theta_0 - \eta_0)/(\cos \theta_0 + \eta_0). \quad (4.3.6)$$

Let the fluctuating fields \vec{e} and \vec{h} be represented by Fourier expansions with respective spectral amplitudes $\tilde{e}(\vec{\chi}, \omega)$, $\tilde{h}(\vec{\chi}, \omega)$;

$$\{\vec{e}(\vec{r}, z, t), \vec{h}(\vec{r}, z, t)\} = \int_{-\infty}^{\infty} d\omega \int_{-\infty}^{\infty} d^2 \vec{\chi} \left\{ \tilde{e}(\vec{\chi}, \omega), \tilde{h}(\vec{\chi}, \omega) \right\} e^{i(\vec{\chi} \vec{r} + \chi_z z - \omega t)}, \quad (4.3.7)$$

with $\chi_z = \sqrt{k^2 - \chi^2}$, $\text{Im } \chi_z \geq 0$. By combining the Fourier expansion of the rough surface,

$$\zeta(\vec{r}, t) = \int_{-\infty}^{\infty} d\omega' \int_{-\infty}^{\infty} d^2 \vec{\chi}' \sum_{s=\pm} \tilde{\zeta}_s(\vec{\chi}') e^{i(\vec{\chi}' \vec{r} - \omega' t)} \delta[\omega' - \tilde{\Omega}_s(\vec{\chi}')],$$

with the boundary condition (4.3.2) one can obtain

$$\tilde{e}_z(\bar{\chi}, \omega) = D(\bar{\chi}) \sum_{s=\pm} \tilde{\zeta}_s(\bar{\chi} - \bar{k}_\perp) \cdot \delta[\omega - \omega_0 - \tilde{\Omega}_s(\bar{\chi} - \bar{k}_\perp)], \quad (4.3.8)$$

where $\tilde{\Omega}_s(\bar{\chi} - \bar{k}_\perp)$ is the dispersion law of surface oscillations (with account of a surface stream, [Monin and Krasitsky, 1985]) and

$$D(\bar{\chi}) = -[iG/(\chi_z + k\eta)] [\bar{\chi}(\bar{\chi} - \bar{k}) [g_{0z} + R_{//} g_z] + k_z(\bar{\chi} \cdot [\bar{g}_0 - R_{//} \bar{g}])].$$

Making use of the time domain correlation function $B(\tau)$ of the fluctuating signal $e_z(\bar{r}, z, t)$, we can derive the power spectrum

$$S(\omega) = \frac{1}{2\pi} \int_{-\infty}^{\infty} d\tau e^{i\omega\tau} \int_{-\infty}^{\infty} d^2\bar{\chi}' \frac{1}{2} |D(\bar{\chi}')|^2 \sum_{s'=\pm} \tilde{W}_{s'}(\bar{\chi}' - \bar{k}_\perp) \cdot e^{i(\bar{\chi}' \bar{u} \tau - \omega \tau)} e^{-2\text{Im} \chi'_z z}, \quad (4.3.9)$$

with account of the delta-correlation property of the spectral amplitudes, i.e.

$$\langle \tilde{\zeta}_{s'}(\bar{\chi}' - \bar{k}_\perp) \cdot \tilde{\zeta}_{s''}^*(\bar{\chi}' - \bar{k}_\perp) \rangle = \frac{1}{2} \tilde{W}_{s'}(\bar{\chi}' - \bar{k}_\perp) \cdot \delta_{s's''} \delta(\bar{\chi}' - \bar{\chi}''). \quad (4.3.10)$$

Here $\delta_{s's''}$ is Kronecker's delta and $\tilde{W}_{s'}(\bar{\chi}' - \bar{k}_\perp)$ a nonsymmetric wavenumber spectrum [Monin and Krasitsky, 1985], with $\omega' = \omega_0 + \tilde{\Omega}_s(\bar{\chi}' - \bar{k}_\perp)$ and $\text{Im} \chi'_z z \geq 0$, as both $\text{Im} \chi' \geq 0$ and $z \geq 0$.

Consider a compact-size antenna at $z = 0$. Performing integration over τ in (4.3.9) and going over from $\bar{\chi}$ to $\bar{q} = \bar{\chi}' - \bar{q}$, we can arrive at

$$S(\omega_0 + \Delta\omega_s) = \frac{1}{2} \sum_{s=\pm} \int_{-\infty}^{\infty} d^2\bar{q} |D(\bar{q} + \bar{k}_\perp)|^2 \tilde{W}_s(\bar{q}) \delta[\Delta\omega_s - s\Omega(\bar{q})]. \quad (4.3.11)$$

4.3.3 Interpretation of model results and comparison with experiment

Eq. (4.3.11) was used in numerical modeling of the scattering process. The input parameters were the operating frequency, wave vector of the radio wave, dielectric constant and conductivity of sea water, wind speed and angle made by the wind direction and the viewing line, length of the radio path, and spectral resolution. The computed output involved graphic and numerical representations of the sea-scattered signal. The computer program allowed a variety of models for the sea spectrum, which could be isotropic, 'semi-isotropic' or anisotropic.

Examples of computed amplitude spectra of the sea-scattered signal are given in Fig.4.3.3-4.3.4, where wind speed is the basic parameter. The graphs in the figures are for $f_{oper} = 15$ MHz and

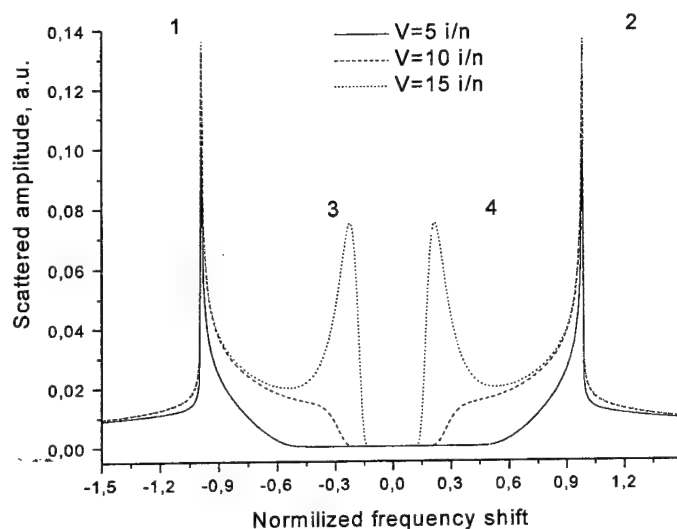


Fig. 4.3.3 Model spectra of the scattered signal

shape is dependent everywhere (except the peaks near $F = \pm 1$) upon the wind speed and the operating frequency. The spectrum may involve more than two peak, plus non-zero components at frequencies above the Bragg values.

Fig. 4.3.4 shows similar scattered spectra, however calculated for an anisotropic sea wave spectrum. Comparing Fig. 4.3.3 and Fig. 4.3.4, one can see that the effect of an anisotropic

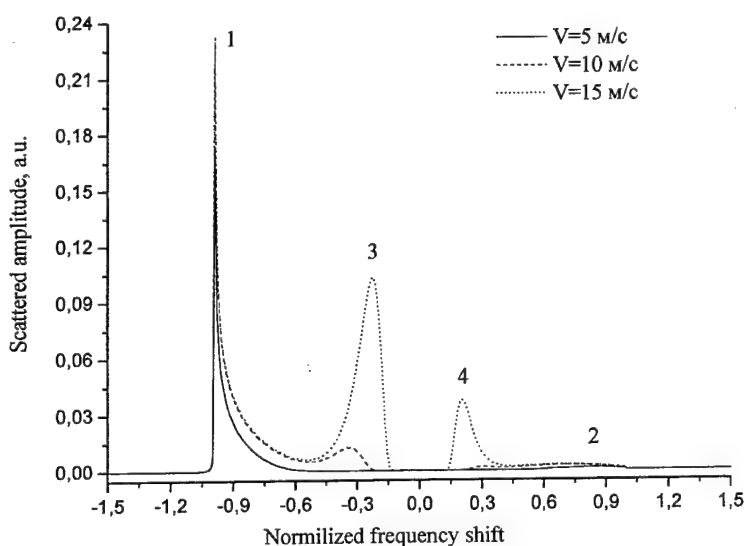


Fig. 4.3.4 Model spectra of the scattered signal

angle of incidence of the radio signal $\theta_0 = 75^\circ$. The abscissa represents the frequency shift normalized to the Bragg frequency for grazing incidence.

The curves have been computed with a relative spectral resolution of 0.01 for the isotropic Pierson-Moskowitz sea wave spectrum. By analyzing Fig. 4.3.3, one can clearly see differences between the 'bistatic' sea-scattered spectrum and the known spectra typical of monostatic radar sounding. First, the scattered spectrum is continuous rather than discrete and, which is quite important, its

shape is dependent everywhere (except the peaks near $F = \pm 1$) upon the wind speed and the operating frequency. The spectrum may involve more than two peak, plus non-zero components at frequencies above the Bragg values.

Fig. 4.3.4 shows similar scattered spectra, however calculated for an anisotropic sea wave spectrum. Comparing Fig. 4.3.3 and Fig. 4.3.4, one can see that the effect of an anisotropic spatial distribution of sea waves is to change the relative importance of the scattered spectral peaks 1 to 4. Numerical simulation for the conditions of the experiment of Fig. 4.3.2 has allowed recovering the theoretical scattering spectrum. It is represented by curve 4 in Fig. 4.3.2 and shows a fair qualitative agreement with the measured spectrum of curve 3. In both cases four spectral peaks are present, located at

the same points on the frequency axis (the locations are determined by the wind speed, height of the sea-waves and angle of incidence of the radio signal). The amplitudes of the negative-frequency peaks are greater in magnitude, which effect is controlled by the wind direction with respect to the line of vision. It seems of interest to compare three measured spectra that were taken one after another with a fixed length of the radio path and fixed frequency (curves 1 to 3 in Fig. 4.3.2). The first spectrum taken corresponds to curve 1. By the time it was measured the direction and speed of wind in the area had remained nearly unchanged for at least four hours. The spectrum clearly demonstrates a negative-directed shift of the Bragg frequencies of about 0.05 Hz, which corresponds to a 0.34 m/s radial speed component of the wind-driven surface current. Later on the wind speed dropped down. The corresponding radio spectrum is represented by curve 2 of the Figure. As can be seen, the Bragg maxima have acquired a multiple mode character. Some of the peaks are at the frequencies that can be obtained through a calculation without account of the surface current, and thus are symmetrical with respect to zero frequency (cf. curve 4). Other peaks on this curves are shifted toward the negative end. Finally, the spectrum of curve 3 was measured when the wind speed dropped down to 2 or 4 m/s. Like in curve 1, the spectrum peaks are of single-mode character again, however none of them shows a negative-directed shift. Besides, all show a slight increase in amplitude.

Summarizing the results of this Subsection, note the rigorous mathematical model of the effects of bistatic HF radio scattering by the rough sea surface. The model has been used for numerical analysis of power spectra of the scattered signal in dependence on meteorological conditions, for a variety of model spatial spectra of the sea roughness. Comparison of measured spectra of the scattered radio signal with the numerical model has demonstrated a qualitative agreement of the theory developed with the experiment. If the ionospherically reflected sounding signal is sufficiently higher than the external noise level, analysis of the scattered radio spectra permits estimating some oceanographic parameters, like sea wave height, surface-level wind speed and radial component of the surface stream velocity.

4.4 Magnetic effect of atmospheric weather disturbances in Antarctica

Monitoring of the geospace with the aim of forecasting its physical state is a scientific and technical problem of utmost importance in the XXI century. The attention of researchers is centered mainly on the direct impact of corpuscular and radiative solar fluxes on the terrestrial plasma. Meanwhile, a counter flow of energy is also known, which is directed upwards from the Earth's surface. The energy carriers in the case are the large-scale atmospheric gravity waves (AGW)

generated by earthquakes, powerful cyclones and atmospheric fronts or technogenic agents of various kind. When reaching the altitudes of the ionospheric dynamo region, these AGWs may be able to modify ionospheric conductivities and electric currents (cf. Section 3.5), bringing forth periodic variations in the magnetic field strength at the Earth surface.

The Antarctic Peninsula is highly suitable for studying these effects for quite a number of reasons. First, the cyclone activity which the region is known for should be able to excite large-scale AGWs. Besides, the Peninsula itself represents an extended 'transverse' obstacle on the way of active cyclones, and hence might play the part of an orographic source of AGWs.

The processing procedures applied to the available sets of measured data were aimed at assessing the feasibility of AGW-effectuated transfer of the energy contained in tropospheric disturbances to ionospheric heights, with subsequent transformation in the dynamo region into magnetic field variations.

4.4.1 Methodology of data processing

To answer the question posed, it is necessary to first identify signatures of the waves we seek in the parameters that are measured. As is known, the only AGWs capable of propagating between the Earth's surface and the dynamo region (altitudes about 100 to 140 km) are large-scale waves of much lower frequencies than the Brunt – Väisälä magnitude (0.002 Hz). Atmospheric waves of smaller scales traveling away from the surface are reflected back at much lower altitudes. Therefore, when designing the data processing scheme we concentrated on wave processes of greater periods than 0.5 hr. Generally, an individual realization of a large scale AGW is seen as quasiperiodic changes of measurable parameters with a period of 0.5 hr to 3 h and consisting of a few variations. Since the time-domain window to perform the analysis should be matched with the expected duration of the process of interest, data processing was made in a sliding six-hour window that was shifted in one hour steps.

The amplitudes of AGW-related variations are about 1mbar in terms of atmospheric pressure or units of nT in terms of magnetic field (cf. Section 3.5). Both in air pressure and in magnetic field components, the variations we seek occur against the background of stronger but slower variations. In the magnetic field, such are the regular diurnal variations (summertime span up 50nT) or the disturbances associated with changing phases of magnetic storms (up to 100nT). In the surface air pressure, these are the variations associated with passage of large-scale formations like cyclones or anticyclones (pressure surges about 30 to 50 mbar). From the point of data processing, all this suggests the necessity of preliminary filtering. For example, application of high-pass filters in the frequency domain could be recommended at this stage. It is essential that

the filters used for different parameters possessed similar response functions. An alternative technique might be to evaluate sliding means of the individual records, averaged over greater time periods than the longest expected period of variation. The technique that proved particularly efficient (and was adopted in the end) was that of record detrending, i.e. approximation of the time domain window by a set of N -th order polynomials and further subtraction of these from the magnitude being treated.

At the next step the observational periods were subdivided into magnetically quiet and magneto-disturbed. The quasiperiodic magnetic field variations related to the AGWs of tropospheric origin were sought for in the first case only.

The next task was detection of the effect. By applying a program-implemented algorithm we intended to find out whether quasiperiodic variations of the surface air pressure and magnetic field component, admittedly associated with AGWs, were present in the records within the limits of a specified one-hour interval. If they were, then the question was if they really were related to the same source. An answer to the first question was sought through construction of amplitude spectra for the realizations of both processes. As a further step, their peaks were determined and compared with a specified threshold value. The conclusion on the presence (absence) of the effect could be made in each channel, depending on whether the peak was higher (lower) than the threshold (see Table 4.4.1).

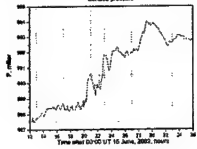
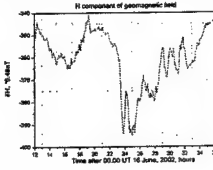
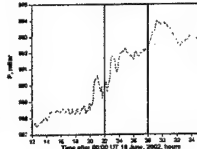
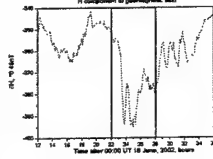
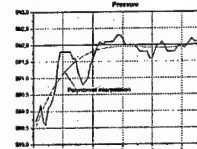
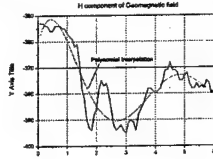
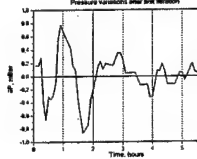
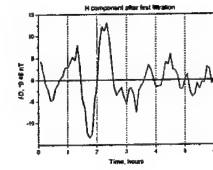
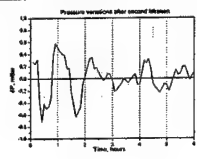
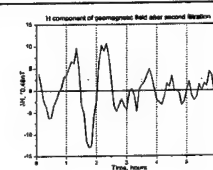
To clarify if the variations originate from the same source, several steps have been envisaged in the detection algorithm. Step1 consists of comparing the frequencies of peak location in the spectra of magnetic field components and air pressure. Further steps are taken if these frequencies fully coincide or differ by no more than one discrete count in the frequency domain. Step2 is filtering with a rectangular window to suppress low frequency components of longer periods than 2 hr. Then follows construction of the cross-correlation function for the variations. The sought for effect is considered to be present if the correlation maximum is greater than a certain threshold (specifically, greater than 0.3 in absolute value).

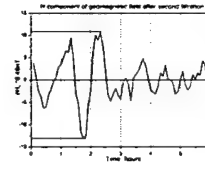
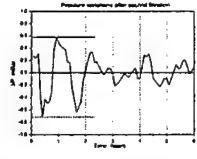
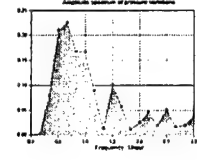
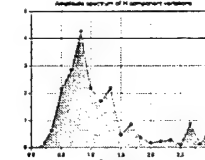
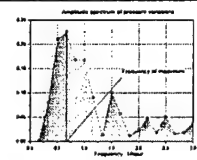
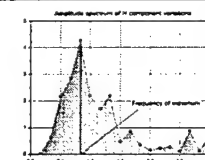
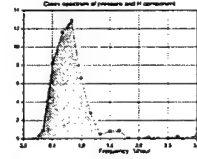
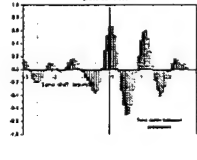
Validity tests for the detection algorithms

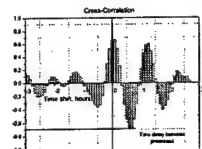
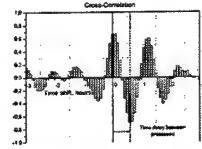
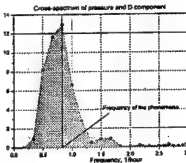
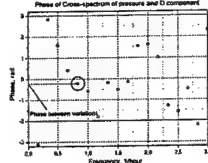
It seems quite probable that several different sources of AGWs might be active simultaneously at different altitudes in the atmosphere. For example, these might be a magnetic disturbance produced by fluctuations in the solar wind or passage of the solar terminator – both can generate atmospheric gravity waves detectable near the Earth's surface. In case periods of the AGWs at different altitudes happened to be close to each other, the detection algorithm would signal positively about presence of the effect we seek, which would be a wrong decision since we are interested in the AGWs propagating from the troposphere to the ionosphere. Unfortunately, a

Table 4.4.1

Processing algorithm for meteorological and magnetic data

Stage	Baric pressure	Illustrating examples	Magnetic field component	Illustrating examples
	Surface pressure		Relative variation in components of the Earth's magnetic field	
Pre-processing	Gap detection and filling up		Gap detection and filling up	
			Reducing the magnetic data to the 5-min sampling rate of the meteo data	
Filtering	Detection of the sought for data in a specified time interval		Detection of the sought for data in a specified time interval	
	Approximation by 5-th order polynomial		Approximation by 5-th order polynomial	
	Detrending (subtraction of the 5-th order polynomial)		Detrending (subtraction of the 5-th order polynomial)	
	High pass filtering with a rectangular spectral window ("zero level suppression" of three lowest-order harmonics in the amplitude spectrum)		High pass filtering with a rectangular spectral window ("zero level suppression" of three lowest-order harmonics in the amplitude spectrum)	

			Estimating the span of magnetic field variations	
			In case the span is less than 30 nT, the magnetic conditions are regarded as quiet and the analysis is continued	
<i>Detection algorithm for quiet magnetic conditions</i>	Estimating the span of variation in filtered air pressure data			
	In case the span is greater than 1 mbar, the analysis is continued			
	Evaluating the amplitude spectrum		Evaluating the amplitude spectrum	
	Searching for maximum value in the spectrum		Searching for maximum value in the spectrum	
	In case the maxima in both spectra belong to variation periods less than 2 hr, the analysis is continued			
	If the peak frequencies of the two spectra are separated less than by one discrete count in the frequency domain ($1/6 \text{ hr}^{-1}$), then the analysis is continued			
	If the amplitude spectrum peaks exceed the mean level of fluctuations by more than 2 dB, then the analysis is continued			
	Evaluating the cross spectrum of filtered data			
	Evaluating the cross-correlation function (CCF)			
	If the CCF extremum is greater than 0.3 in absolute value, then it is concluded that the effect is present over the time period under analysis			

<i>Estimating parameters of the effect</i>	Evaluating the CCF extremum in a ± 1 hr interval about zero		
	Measuring the time shift of the CCF extremum from zero		
	Estimating parameters of the cross spectrum (peak magnitude and phase shift)		
	Saving the processed data in the RESULTS file: year; month; effect containing period; variation frequency (as determined from the cross-spectrum); span of air pressure variations; span of magnetic field variations; magnitude of the cross spectrum peak; phase of the cross-spectrum at the peak frequency; magnitude of the CCF extremum with respect to zero lag		

hundred per cent guarantee of excluding mistakes cannot be given. However, if long enough series of observational data are available, it is possible to evaluate statistically the efficiency of detecting the interrelated events in some special way. Here is how it was done at the stage of algorithm optimization. The data series belonged to a seven-year period (1996-2002). First, the detection algorithm was applied to synchronized data on the pressure and magnetic field variations. Later on, the algorithm was tested with records shifted with respect to one another by a one-year interval. For example, a 1997 record of baric pressure was fed together with a 1998 magnetic field realization, or vice versa. Parameters of the detection algorithm were adjusted so as to maximize the ratio of the number of true detections to that of accidental coincidences (with shifted record series).

At the end of the detection procedure the stage of parameter evaluation started with respect to the AGWs detected in the pressure and magnetic field variations. As soon as the detection algorithm signaled on the presence of like variations in the two magnitudes, apparently related to AGWs, parameters of the cross-correlation function (CCF) and co-spectrum were determined. The time lag between the processes was evaluated by establishing the absolute extremum of the cross-correlation function within the ± 2 hr range of lags.

This technique is analogous to time lag determination from the maximum of the CCF envelope. Next, the appearance frequency histogram was constructed for time shift of the CCF extrema with respect to the zero lags. The median of this histogram was used for estimating the AGW

propagation time. It seems plausible that the time shifts shown by the CCF of the pressure and magnetic field variations that coincided in time accidentally and were not related to any common source should be a uniformly distributed random value. Whereas related processes of the same period would be characterized by nearly equal time and phase shifts, and hence give rise to a peak in the histogram.

4.4.2 Results of data processing

Shown in Fig. 4.4.1 is the histogram of relative time shifts for air pressure variations and those of horizontal magnetic field components (H and D), characterized by periods of 0.5 to 1.5 hr. Positive shifts of the CCF maximum correspond to the cases where pressure variations are in advance of changes in the magnetic field. The median value of the time shift is positive and equal to ≈ 0.5 hr. This fact can be interpreted as a manifestation of an upward directed vertical component in the AGW velocity. The magnitude of the vertical velocity component (estimated as the altitude of the dynamo region divided by the time shift between the pressure and magnetic field variations) proves to be ≈ 200 km/hr, or 60 m/s.

4.4.3 Conjugate area effects of weather perturbations in Antarctica

We have shown above that variations of the geomagnetic field may be related to the propagation of AGWs stimulated by a meteorological process in the lower atmosphere. Meanwhile, a comparative analysis of the magnetic data measured at *Akademik Vernadsky* and in the vicinity of its conjugate point (specifically, in Millstone Hill, MA) has demonstrated a high level of correlation between variations in horizontal components of the geomagnetic field. This suggests a possible transfer of meteo-stimulated disturbances in the magnetic field from one hemisphere to the other, namely to the magnetically conjugate area. By way of example, consider the behavior of surface air pressure and magnetic field components on 21 September, 1999 (Fig. 4.4.2.). The cyclone that passed over station *Vernadsky* generated an AGW (see pressure variations at 18 to 24hr UT in Fig. 4.4.2 a, Fig. 4.4.2 d). Some time later similar variations started in the D-component of the magnetic field at *Vernadsky* (18 to 24 hr UT, Fig. 4.4.2 b, Fig. 4.4.2 e) and, with a smaller amplitude, in the conjugate area (Fig. 4.4.2 c, Fig. 4.4.2 f).

Summarizing the results described in this Subsection, we note significant points as follows. A special methodology has been developed for the treatment of large volumes of meteorological and magnetic data, aimed at revealing parameter variations associated with propagation of large-scale atmospheric gravity waves (AGW). The methodology was applied to a seven year array of data accumulated at the Ukrainian Antarctic station *Akademik Vernadsky*, which allowed relating variations in surface air pressure to such in horizontal components of the geomagnetic field. The

median value of the time shift between variations in the two magnitudes is close to 0.5 hr, with pressure variations being in advance of the magnetic field. This can be regarded as evidence for energy transfer from tropospheric disturbances to ionospheric/magnetospheric altitudes by means of large scale AGWs of time periods between 0.5 hr and 1.5 hr. The estimated vertical velocity of AGW propagation (derived from the time shift between the pressure and magnetic field waveforms) is about 200 km/hr. The disturbances in the Earth's magnetic field produced by the AGWs propagating in the dynamo region can be transferred to the magnetic conjugate area. This is evidenced by observations of synchronous changes in the magnetic field at *Vernadsky* and near Boston, MA (the MIT Haystack Observatory). The corresponding theoretical model is given in Subsection 3.5.

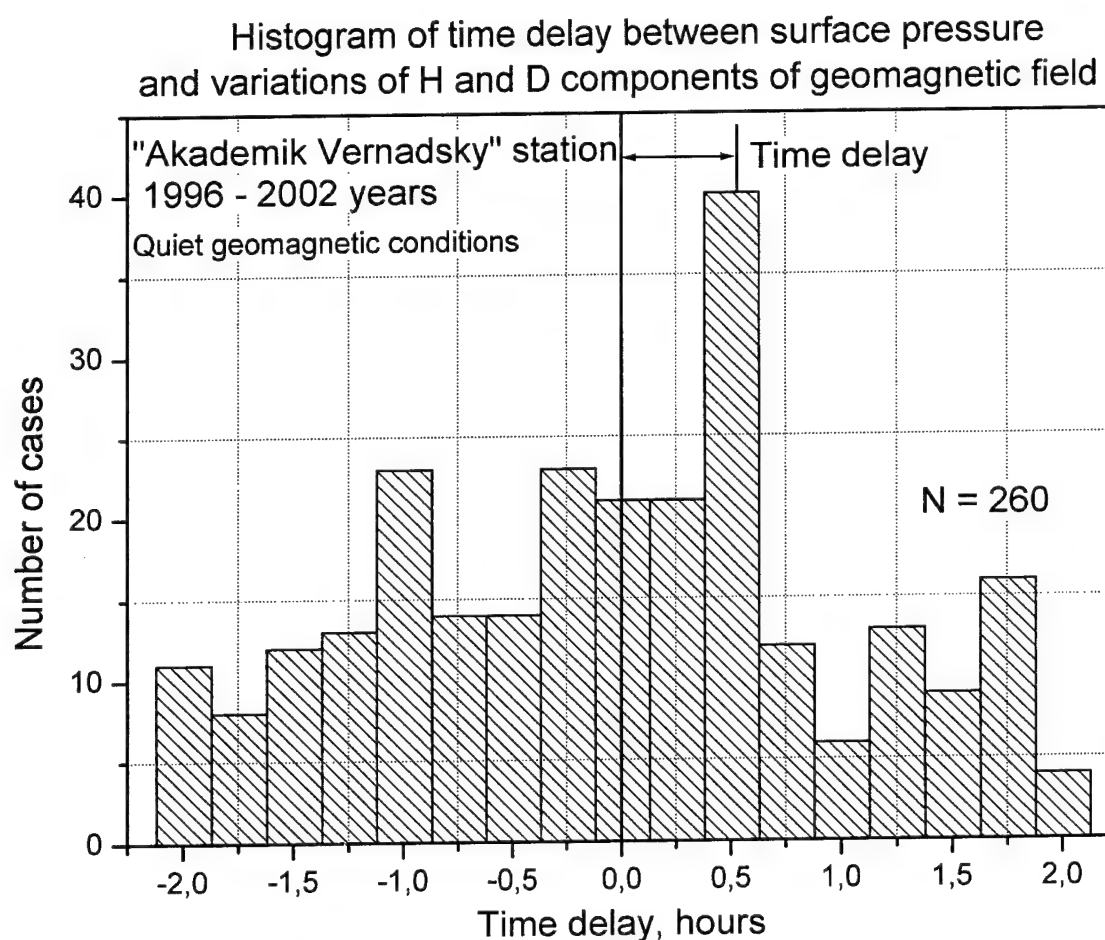


Fig. 4.4.1 Histogram of time delays between variations of the surface air pressure and horizontal components of the Earth's magnetic field.

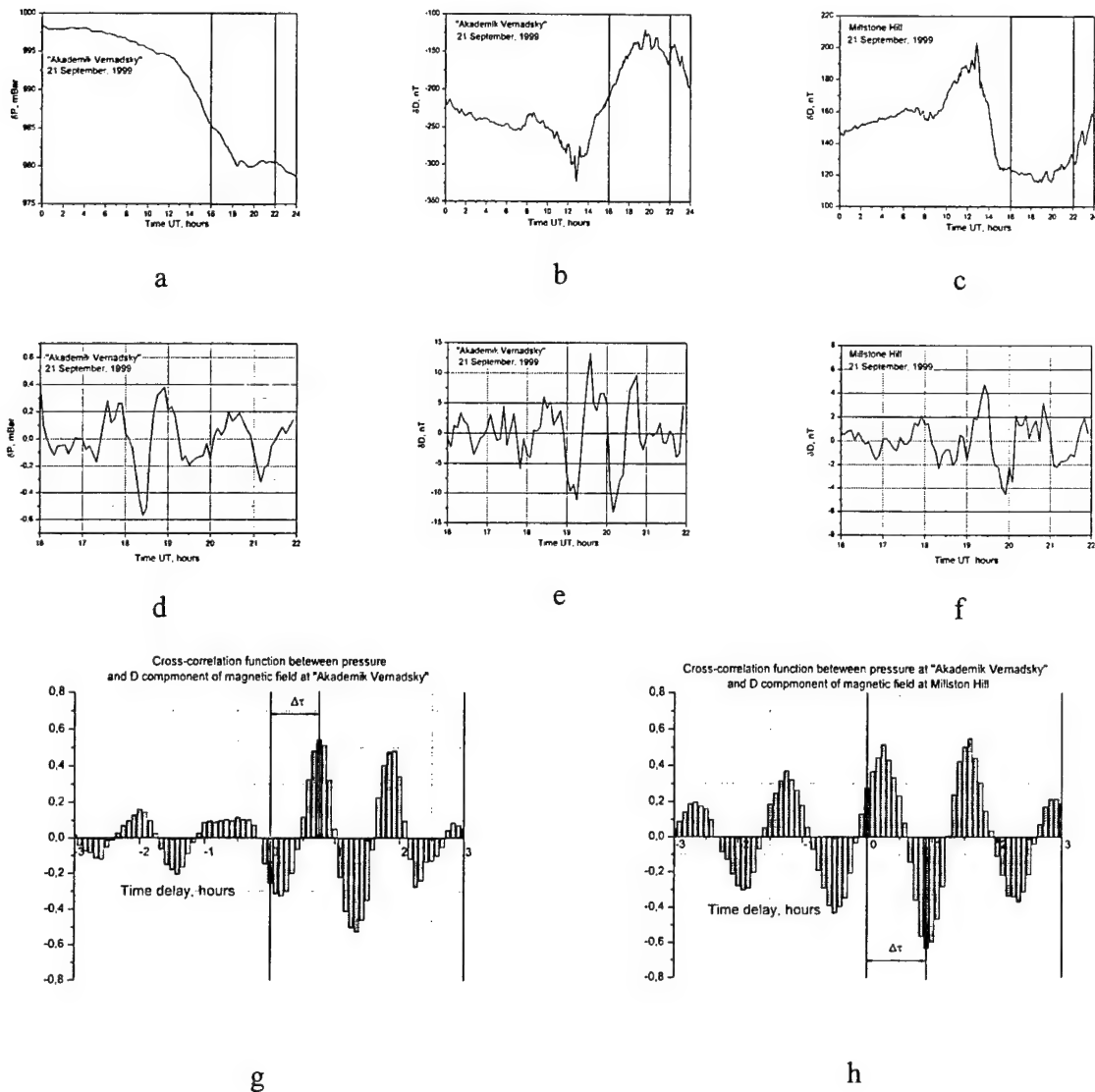


Fig 4.4.2

- a) Atmospheric pressure at *Akademik Vernadsky*, 21 September, 1999
- b) Variations in the geomagnetic field D-component at *Vernadsky*, 21 September, 1999
- c) Variations in the magnetic field's D-component in Millstone Hill, 21 September, 1999
- d) Narrow band-filtered variations of atmospheric pressure at *Akademik Vernadsky*, 16.00 to 22.00 UT, 21 September, 1999
- e) Narrow band-filtered variations of the magnetic field D-component at *Akademik Vernadsky*, 16.00 to 22.00 UT, 21 September, 1999
- f) Narrow band-filtered variations of the magnetic field D-component in Millstone Hill, MA, 16.00 to 22.00 UT, 21 September, 1999
- g) Cross-correlation function of atmospheric pressure and D-component variations at *Akademik Vernadsky*, 16.00 to 22.00 UT, 21 September, 1999
- h) Cross-correlation function of atmospheric pressure at *Vernadsky* and D-component variations in Millstone Hill, MA, 16.00 to 22.00 UT, 21 September, 1999

4.5 Is the spread F related to geomagnetic field disturbances?

This Subsection describes attempts of finding a correlation between the special kind of natural ionospheric turbulence (which manifests itself as the spread-F effect in ionograms) and disturbances of the geomagnetic field. It is generally accepted as an undisputable fact that magnetic disturbances have a strong impact on many ionospheric parameters, mainly of the upper ionosphere. Owing to ion drag, quick variations of the maximum concentration heights of both F1 and F2 layers are possible. Since the upper ionosphere plasma is 'frozen' in the magnetic field, deformations of magnetic lines of force lead to corresponding drifts of the plasma, and hence to quick fluctuations of the ionospheric critical frequency. In all evidence, a correlation should exist between the intensity of natural ionospheric turbulence and the amount of disturbance in the geomagnetic field. In this Report we have analyzed details of the effect of magnetic disturbances on the appearance probability of ionospheric turbulence and searched for seasonal and diurnal variations in the spread F with the aim of clarifying the physics of the upper ionosphere turbulence.

The spread F effect has been known since early days of vertical ionospheric sounding which technique is used to estimate the basic parameters of ionospheric layers. The phenomenon is manifested as a more or less pronounced broadcasting of reflection traces in an ionogram along the frequency axis (see Fig. 4.5.1)

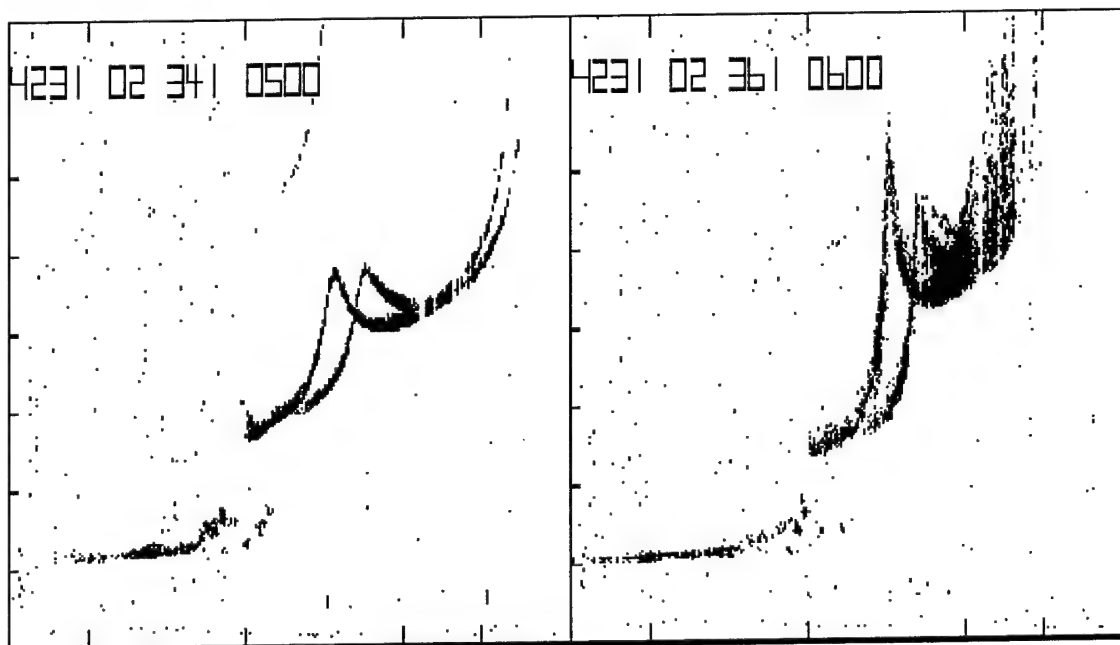


Fig. 4.5.1 A typical 'normal' ionogram (a) and the spread F effect

The reason for this widening of the reflection pattern is scattering of the sounding signal by intense natural irregularities in the ionosphere. During Project execution, we have analyzed the correlation between three-hour K-indices of magnetic activity and appearances of the spread F in ionograms. The interval between the ionograms considered was 1 hour and the period of analysis covered years of 1996 through 2002 (all the data from *Akademik Vernadsky*).

As is known [Parkinson, 1983; Russel and Mc Pherron, 1973], both the geomagnetic activity and ionospheric turbulence show seasonal variations. The magnetic activity is maximal near equinox periods and minimal near solstices. During magnetoquiet years greater levels of ionospheric turbulence are observed mostly in winter and decrease gradually toward summer. The activity shows a pronounced diurnal dependence, with the appearance probability of spread F being higher at night. In the years of enhanced magnetic activity the probability of observing spread F is relatively higher near solstices (see Fig. 4.5.2).

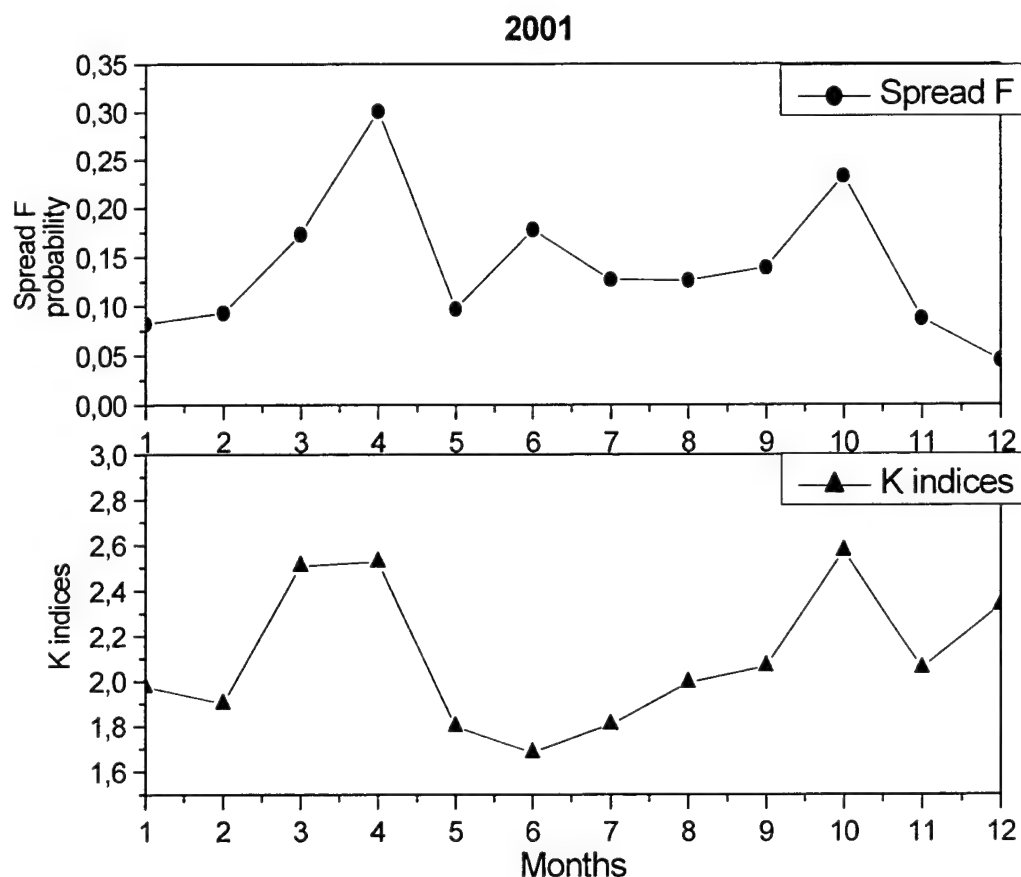


Fig. 4.5.2 Seasonal dependences of the level of geomagnetic activity and observation frequency of spread F in 2001

The data belonging to the seven-year observation period were subjected to several treatment procedures. All the 1hr ionograms containing reflection traces from the F-region were considered. First, the conditional probability of spread F appearance was estimated for every year of observation in dependence on the level of magnetic disturbance (Fig. 4.5.3) It can be seen from the Figure that the dependence is practically absent while the level of disturbance in the geomagnetic field remains low. The appearance probability of spread F increases quite sharply as the level of magnetic disturbance increases to $K \approx 3-4$, however becoming practically invariant at $K > 5$. This run of the appearance probability can be tentatively explained by a threshold dependent character of energy transfer from the varying magnetic field to ionospheric turbulence. The threshold value of the magnetic field might be related to the magnitude of the electric field component exceeding a critical field of some plasma instability.

Another investigation concerned seasonal dependences in the behavior of spread F, having in mind the enhanced geomagnetic activity about the spring or autumn equinox periods. The relative appearance frequency of spread F was calculated for different seasons over the seven year period (Fig. 4.5.4)

As can be seen from the figures, the connection between appearance of spread F and disturbance in the magnetic field is best pronounced around the spring and autumn equinox periods, i.e. near the peaks of geomagnetic activity. The contribution of these periods to the run of ionospheric turbulence versus magnetic activity is the greatest through the entire seven year cycle of observations (Fig. 4.5.5).

That the connection between ionospheric turbulence and geomagnetic disturbances is poorly pronounced in winter periods (May through July, Fig. 4.5.4) might reflect a different nature of the winter spread F effect. It can be stated that the winter spread F is a mostly a night-time effect which accompanies declines of the mean electron density in the F-region.

Conclusions. In this Subsection the behavior of the spread F effect, as observed at the Ukrainian Antarctic station *Akademik Vernadsky* in 1996 through 2002, has been analyzed in its relation to the disturbed geomagnetic field for different seasons. The appearance probability of ionospheric turbulence has been found to demonstrate a nonlinear dependence on the intensity of geomagnetic activity. The threshold value of surface level geomagnetic disturbance after which the probability of observing spread F increases sharply has been estimated as 14 nT. Seasonal variations of the probability have been analyzed for a seven year period of observations. The dependence on the level of geomagnetic disturbances is best pronounced for the spring and autumn equinox periods.

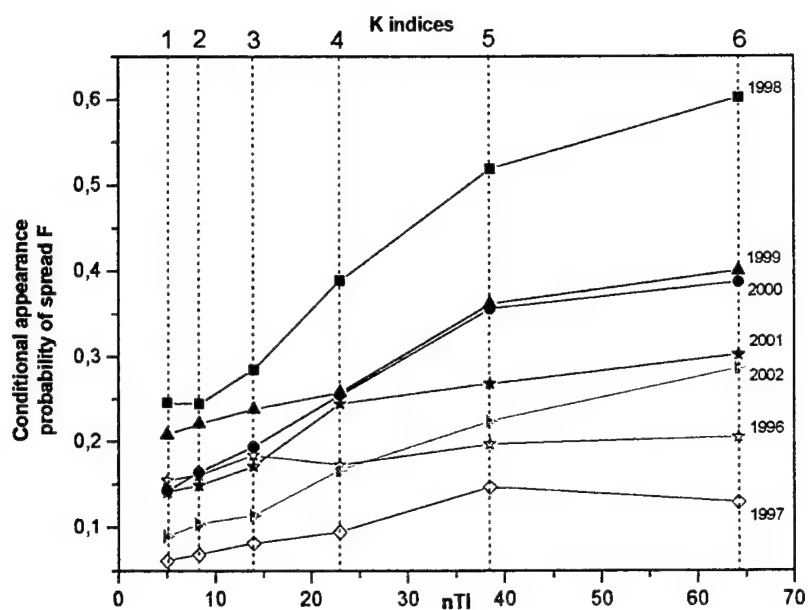


Fig. 4.5.3 Appearance probability of spread F as a function of the geomagnetic activity level

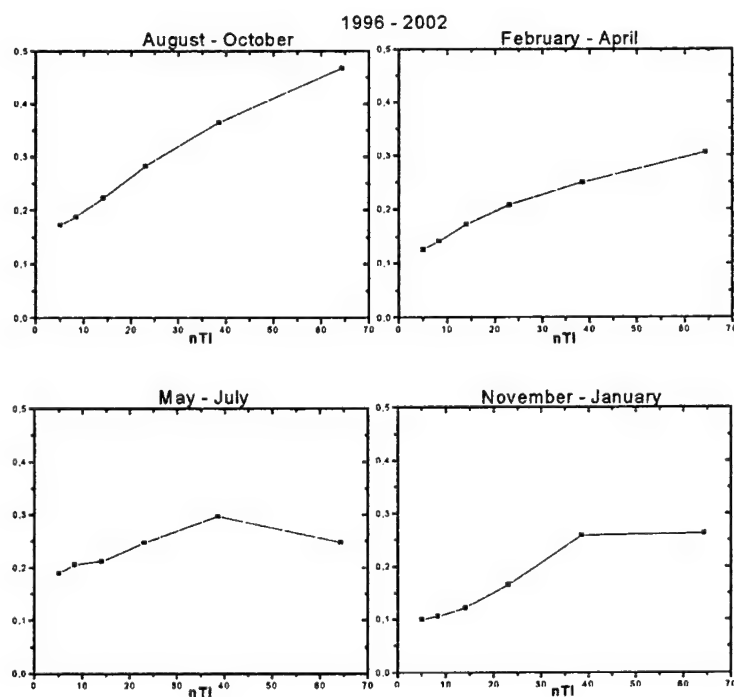


Fig. 4.5.4 Seasonal variations of spread F dependences on geomagnetic activity

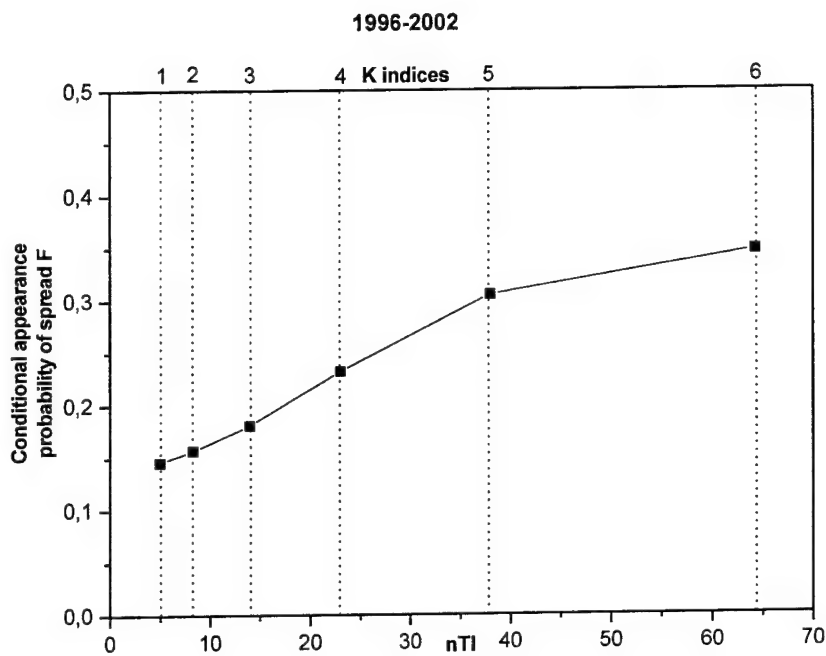


Fig. 4.5.5 Conditional appearance probability of spread F as a function of geomagnetic disturbance level over 1996-2002.

CONCLUSIONS

The principal results obtained within Partner Project P-072 can be summarized as follows.

1. *Ultra low frequency (ULF) band.*

- 1.1. Statistical analysis has been performed of the time series obtained during several years of magnetic field measurements at *Akademik Vernadsky* in the range of Pc3 – Pc4 micropulsations. The most probable frequencies of the resonance pulsations have been established and their diurnal and seasonal variations analyzed.
- 1.2. Two characteristic patterns have been revealed for diurnal dependences shown by the orientation angle of the micropulsation polarization ellipse. The theoretical model developed to describe hydromagnetic wave propagation in the ionosphere provides an adequate physical explanation both to the ‘sunflower’ and ‘arch’ type of behavior of the polarization parameter. A technique has been suggested for recovering transverse ionospheric conductivities from multiple site, multicomponent measurements of pulsations.
- 1.3. A nonlinear interaction of hydromagnetic waves with small-scale ionospheric irregularities has been analyzed theoretically and considered as a candidate mechanism of resonance excitation of turbulence.
- 1.4. The atmospheric gravity waves (AGW) generated by cyclone fronts in Antarctica have been found to produce magnetic field variations. Seven years of data have been analyzed, concerning simultaneous magnetic and meteorological observations at the Ukrainian Antarctic station. A time lag has been revealed between surface air pressure variations and the magnetic response they stimulate. For the AGWs excited by cyclone fronts near the Antarctic Peninsula estimates of characteristic periods have been obtained.
- 1.5. The projection of atmospheric weather disturbances to ionospheric/magnetospheric altitudes and further to the conjugate ionosphere in the North has been analyzed theoretically.

2. *Extremely low frequency (ELF) band.*

- 2.1. Systematic, 24-hour observations of ELF noise were performed in the Schumann range (1 Hz to 40 Hz) during the two years of Project execution..

- 2.2. Diurnal and seasonal dependences have been determined for polarization, frequency and power characteristics of three first resonance modes. Emissions from three centers of global thunderstorm activity have been identified.
- 2.3. An improved theoretical model of the resonant Earth-ionosphere cavity has been developed, taking into account anisotropic properties of the lower ionosphere. Azimuthal corrections to the directions of arrival have been established for the Schumann resonance signals coming from each of the thunderstorm centers. The feasibility of separating a single (African) center has been demonstrated. An algorithm to recover the anisotropy ratio and effective channel height of the cavity has been developed. Single-site measurements have been shown to permit monitoring of long period (seasonal) variations of the integral thunderstorm activity.
- 2.4. Measurements were performed to detect in Antarctica the narrow band radiation at $f = 60$ Hz from systems of electric power production and consumption, and transmission lines of the North American continent. Spectral analysis of intensity variations of this emission has revealed diurnal and weekly periodicities (the weekend effect), and a seasonal run.
- 2.5. A theoretical model of propagation of the narrow band emission from power producing systems and transmission lines has been developed, which permits direction finding toward the source and determination of some parameters of the lower ionosphere.

3. *High frequency (HF) band.*

- 3.1. A triple-channel coherent data taking complex has been manufactured and installed at *Akademik Vernadsky* to record signals from HF broadcasting radios and communication transmitters. These emissions have been registered over the last year of Project execution, with the data processed to determine angles of arrival and Doppler frequency shifts.
- 3.2. The results were used for recovering physical parameters of traveling ionospheric disturbances (TIDs) that passed over the Drake Straits and near the Antarctic Peninsula.
- 3.3. In the course of the marine part of the Antarctic mission HF signals from coastal broadcasting radios were recorded. Bistatic sounding techniques have been developed to study the ionosphere and the rough sea surface.
- 3.4. The bistatic scattering by the sea surface of ionospherically reflected 'illuminating' signals has been analyzed theoretically, which analysis confirmed feasibility of a global scheme of HF radio oceanographic diagnostics.

- 3.5. Very long-range propagation was studied of the radiation from a powerful HF transmitter (heating facility) located in the Northern hemisphere (Tromsø, Norway). Supersonic motions of the artificial ionospheric irregularities stimulated by the heater have been revealed. A simplified theoretical model of plasma drift has allowed estimating motion velocities and directions of the irregularities above the powerful transmitter. Ionosphere-induced nonlinear distortions of the signal spectrum have been detected.
- 3.6. Using a seven-year archive of Antarctic data, the appearance probability of spread F has been analyzed in dependence on the level of disturbance in the geomagnetic fields. A threshold value of the K-index has been established ($K \geq 3$) marking the onset of nonlinear interactions between magnetic field variations and small-scale scattering irregularities.

In the course of Project execution the participants have analyzed noise-like emissions and signals forming the Antarctic electromagnetic environment in a wide frequency range. Possibilities of employing these emissions for monitoring the atmosphere, ionosphere and magnetosphere have been discussed.

It should be noted that only a relatively small fraction of the observational data has been processed by the end date of the Project and it seems expedient to continue this data treatment in the interests of EOARD. Should EOARD express its support as the Partner, the Project participants could take the commitment to complete the processing and interpretation of the data obtained.

The Project Manager and his team express their sincere thanks to Dr. Keith M. Groves who initiated the Project, as well as to directorates of AFOSR and EOARD for their support.

Thanks are also due to Dr. John Foster of the MIT Haystack Observatory, Prof. Bodo Reinisch and Prof. Frank Colby of UMass, Lowell, and Prof. Mark Moldwin of UCLA for fruitful discussion and exchange of scientific data.

APPENDIX:
Spectral and polarization parameters of the Schumann resonances

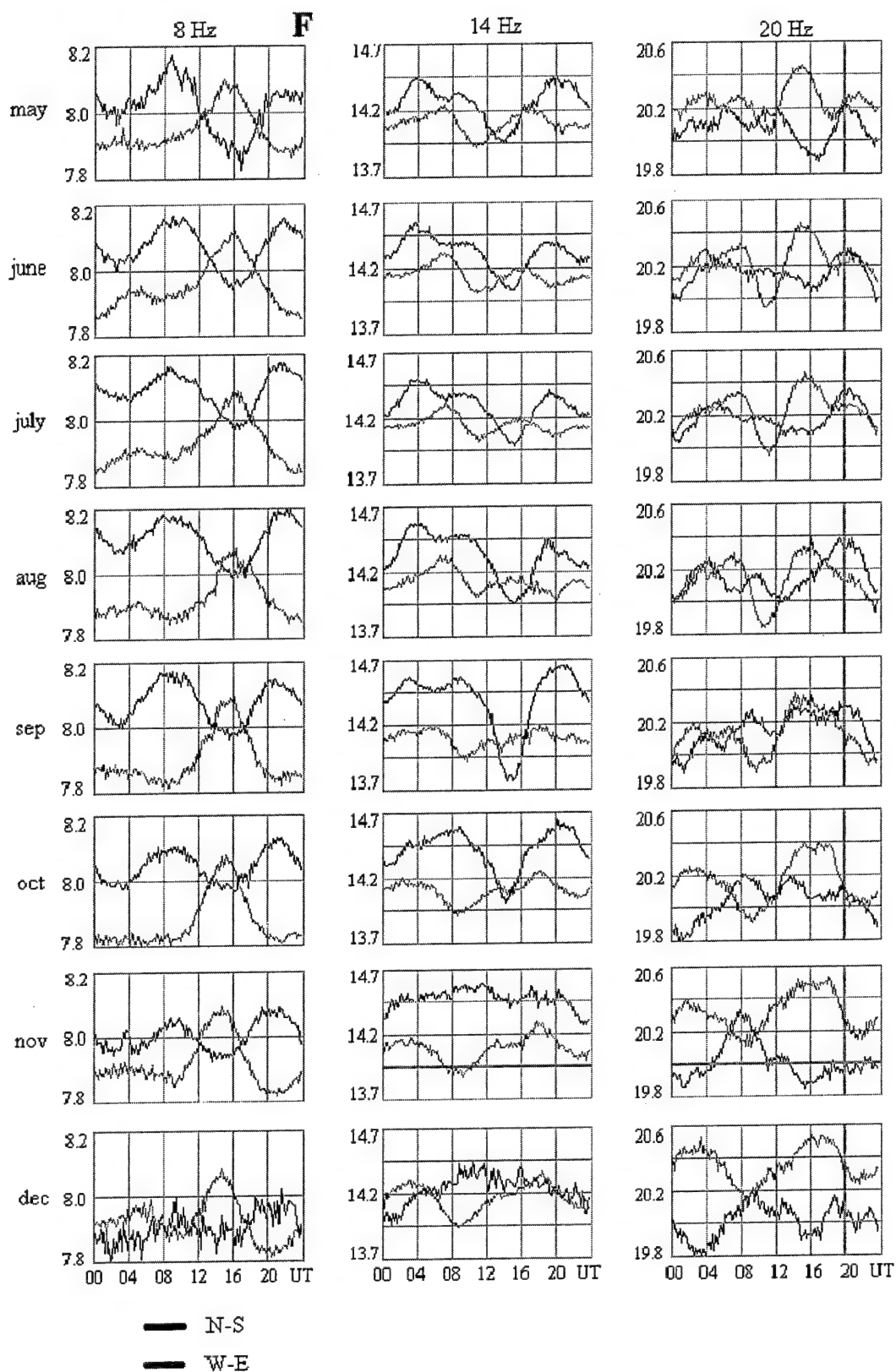


Fig.A 1.1. Month-averaged diurnal variations of the resonance frequency, $F(t)$, for three Schumann resonance modes – May to December, 2001

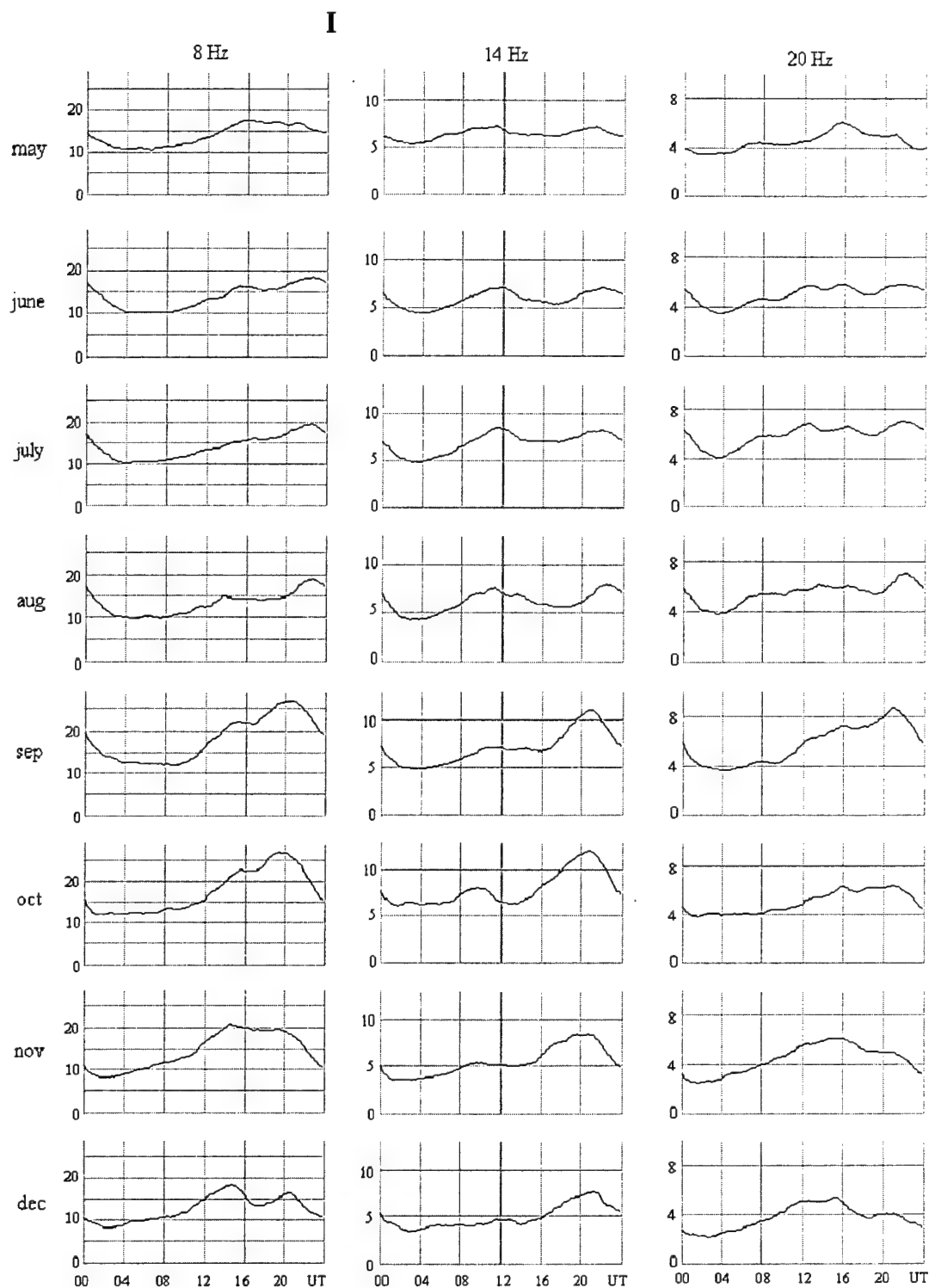


Fig.A 1.2 Month-averaged diurnal variations of intensity, $I(t)$, for three Schumann resonance modes (arbitrary units along the vertical axis): May to December, 2001

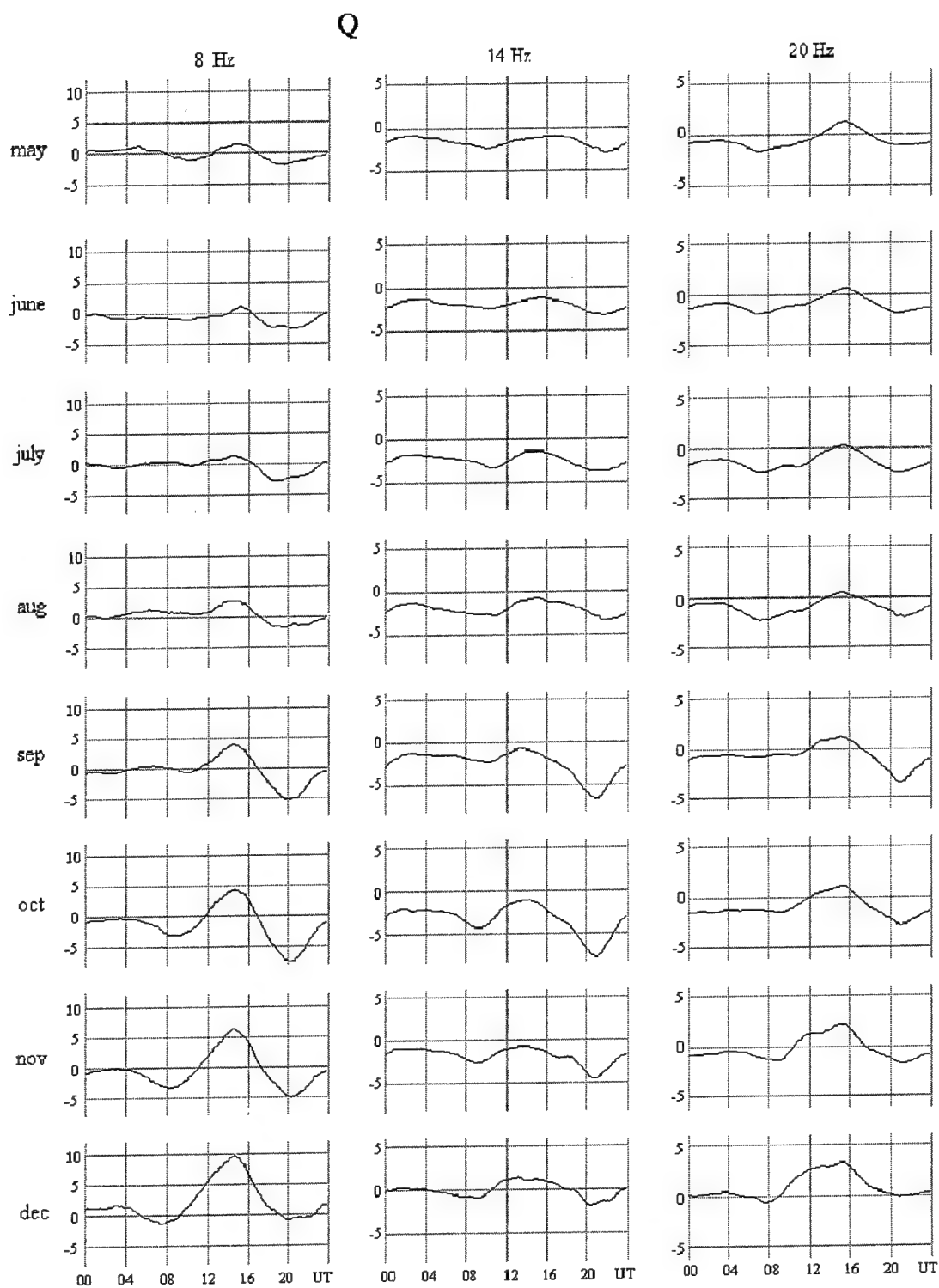


Fig.A 1.3. Month-averaged diurnal variations of the Stokes parameter $Q(t)$ for three Schumann resonance modes (arbitrary units along the vertical axis): May to December, 2001

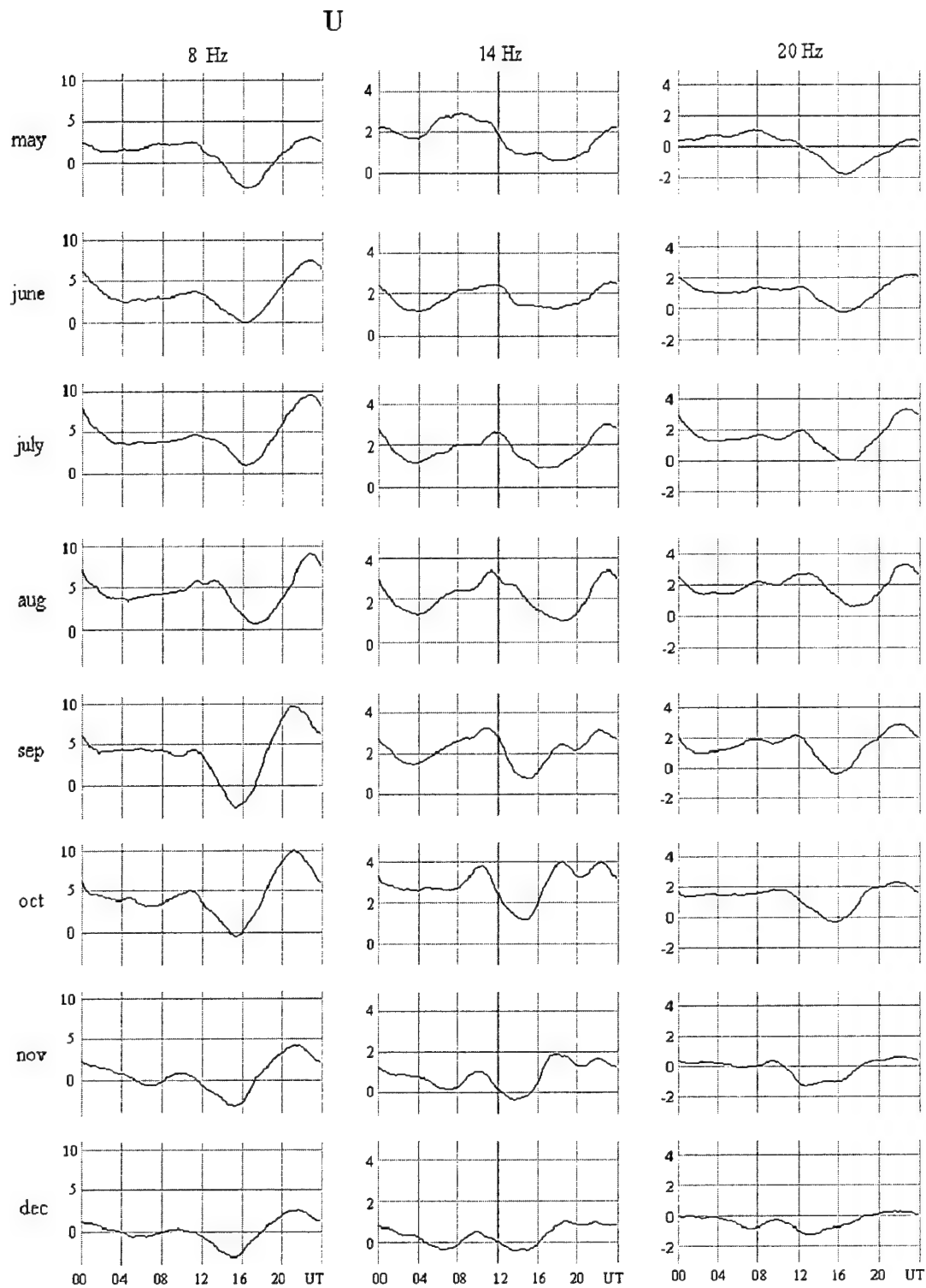


Fig.A 1.4 Month-averaged diurnal variations of the Stokes parameter $U(t)$ for three Schumann resonance modes (arbitrary units along the vertical axis): May to December, 2001

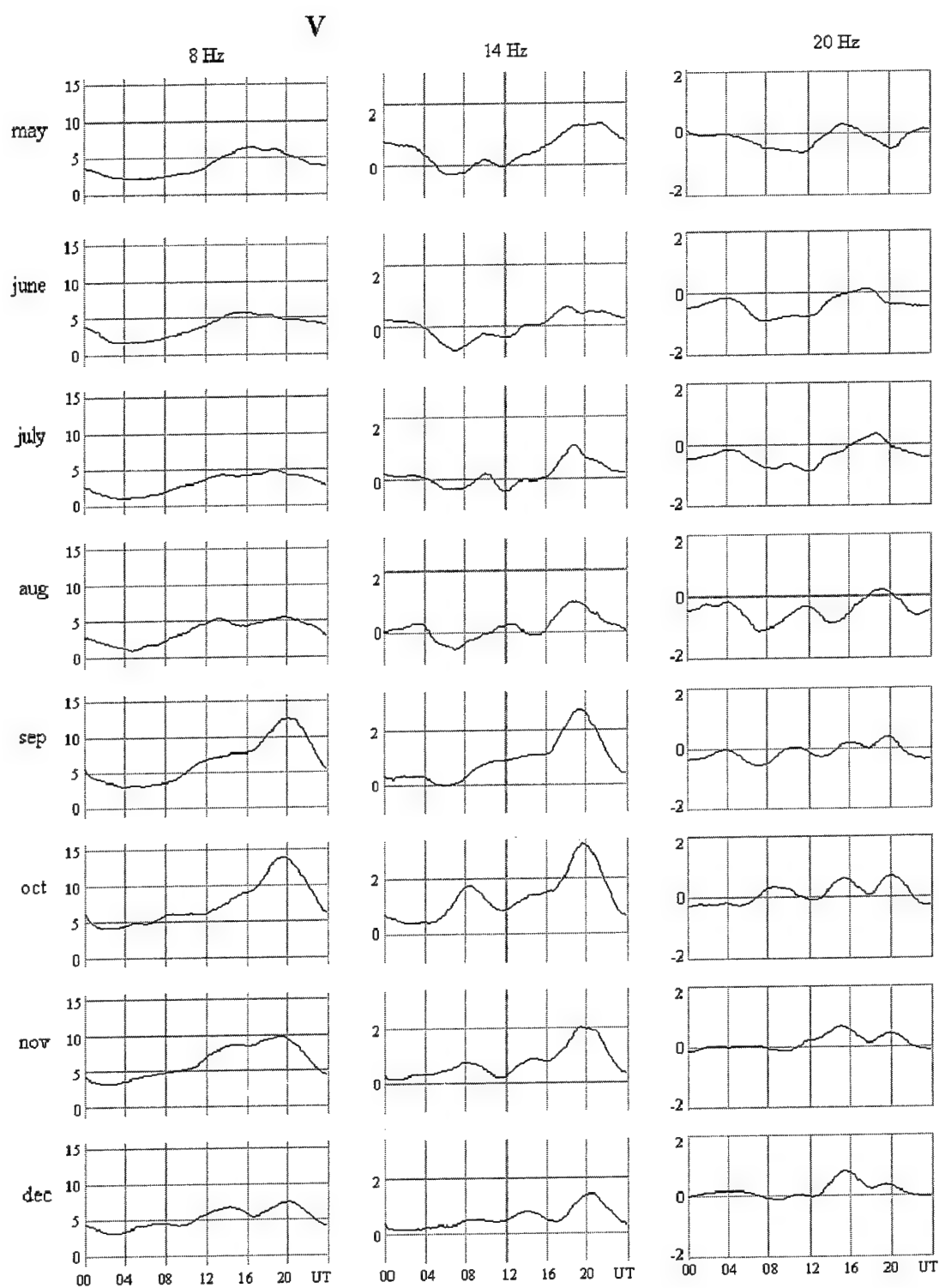


Fig.A 1.5 Month-averaged diurnal variations of the Stokes parameter $V(t)$ for three Schumann resonance modes (arbitrary units along the vertical axis): May to December, 2001

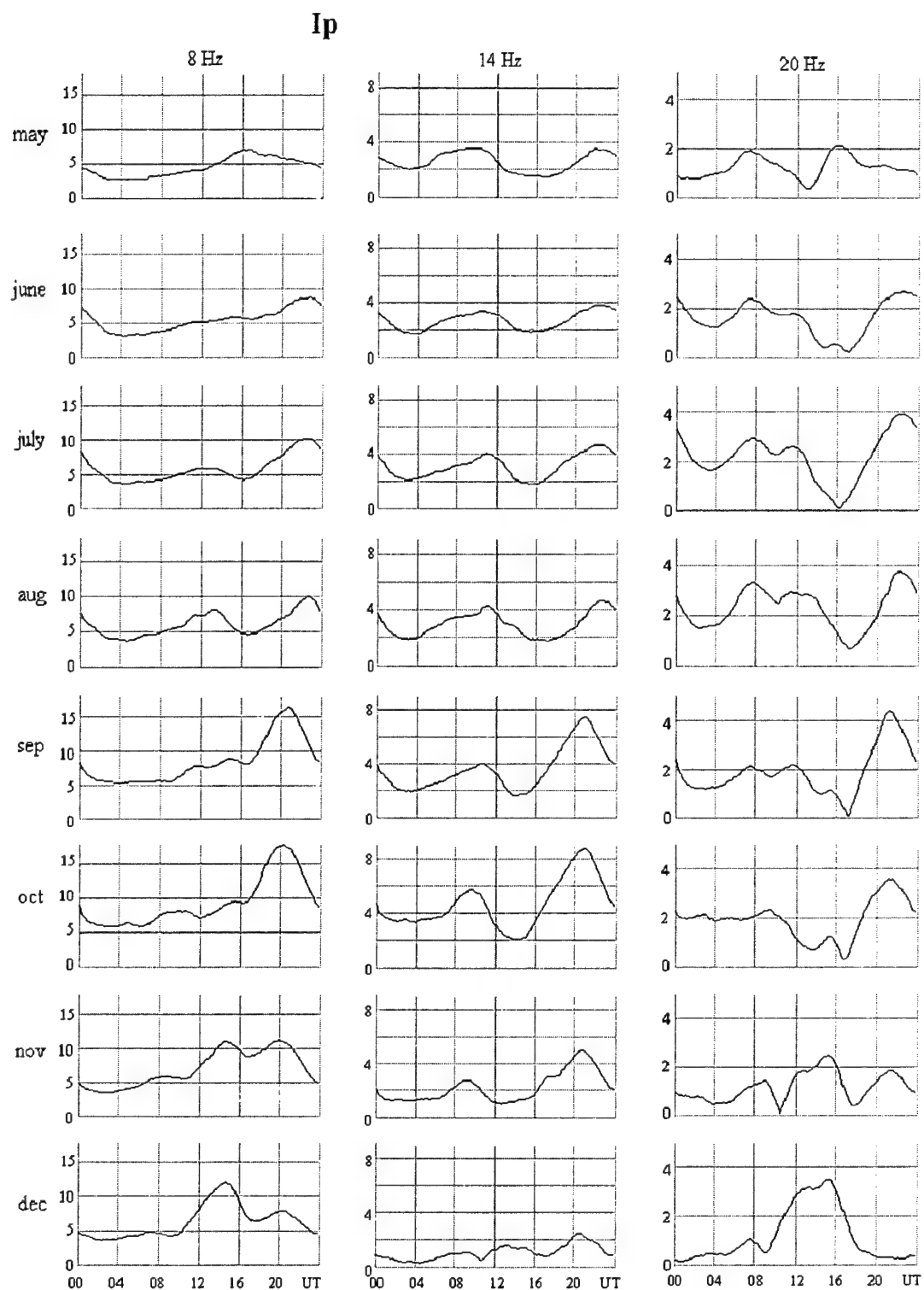


Fig.A 1.6 Month-averaged diurnal variations of polarized component's intensity $I_p(t)$ for three Schumann resonance modes (arbitrary units along the vertical axis): May to December, 2001

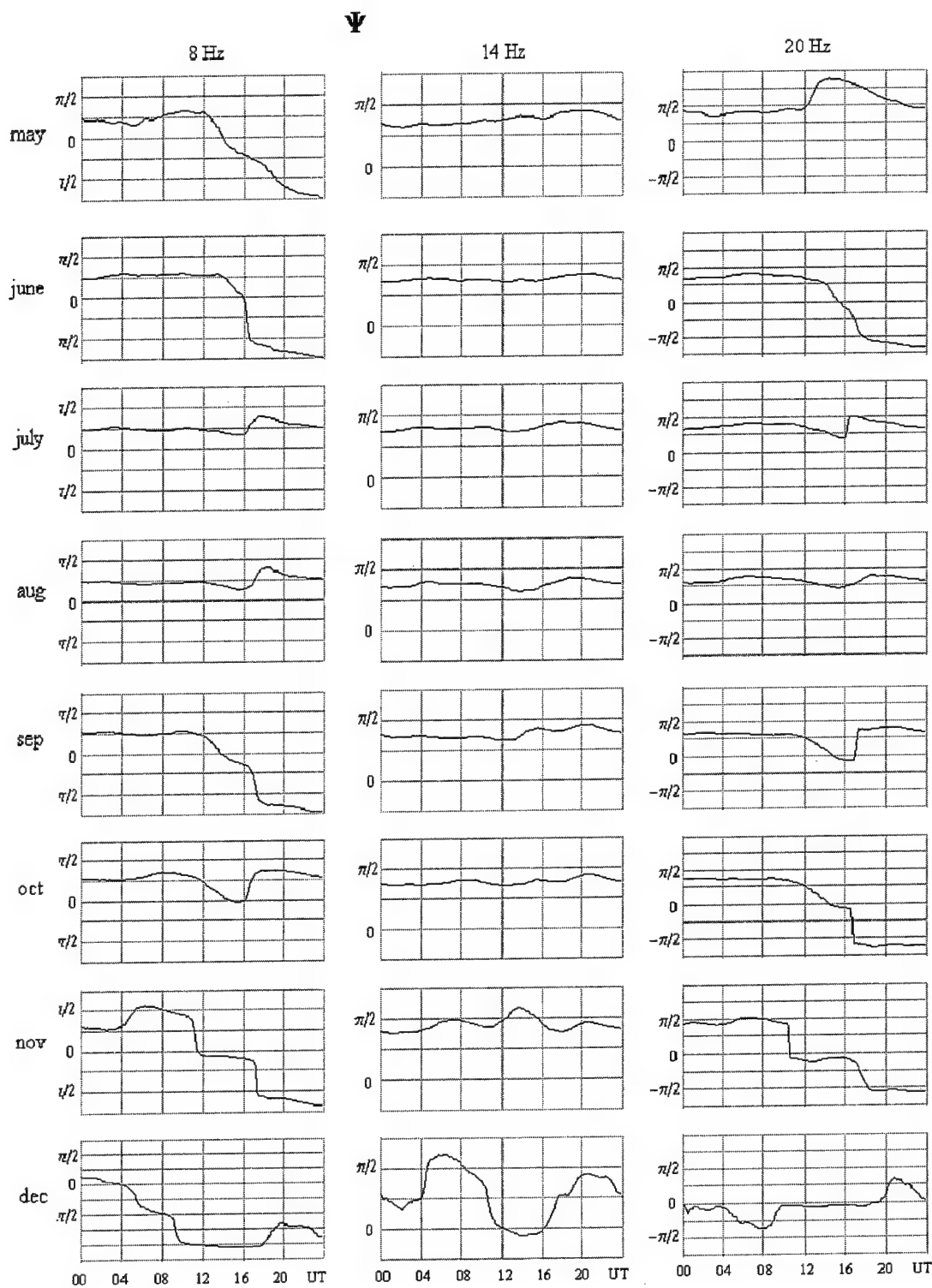


Fig.A 1.7 Month-averaged diurnal variations of the orientation angle $\Psi(t)$ of the polarization ellipse for three Schumann resonance modes (arbitrary units along the vertical axis): May to December, 2001

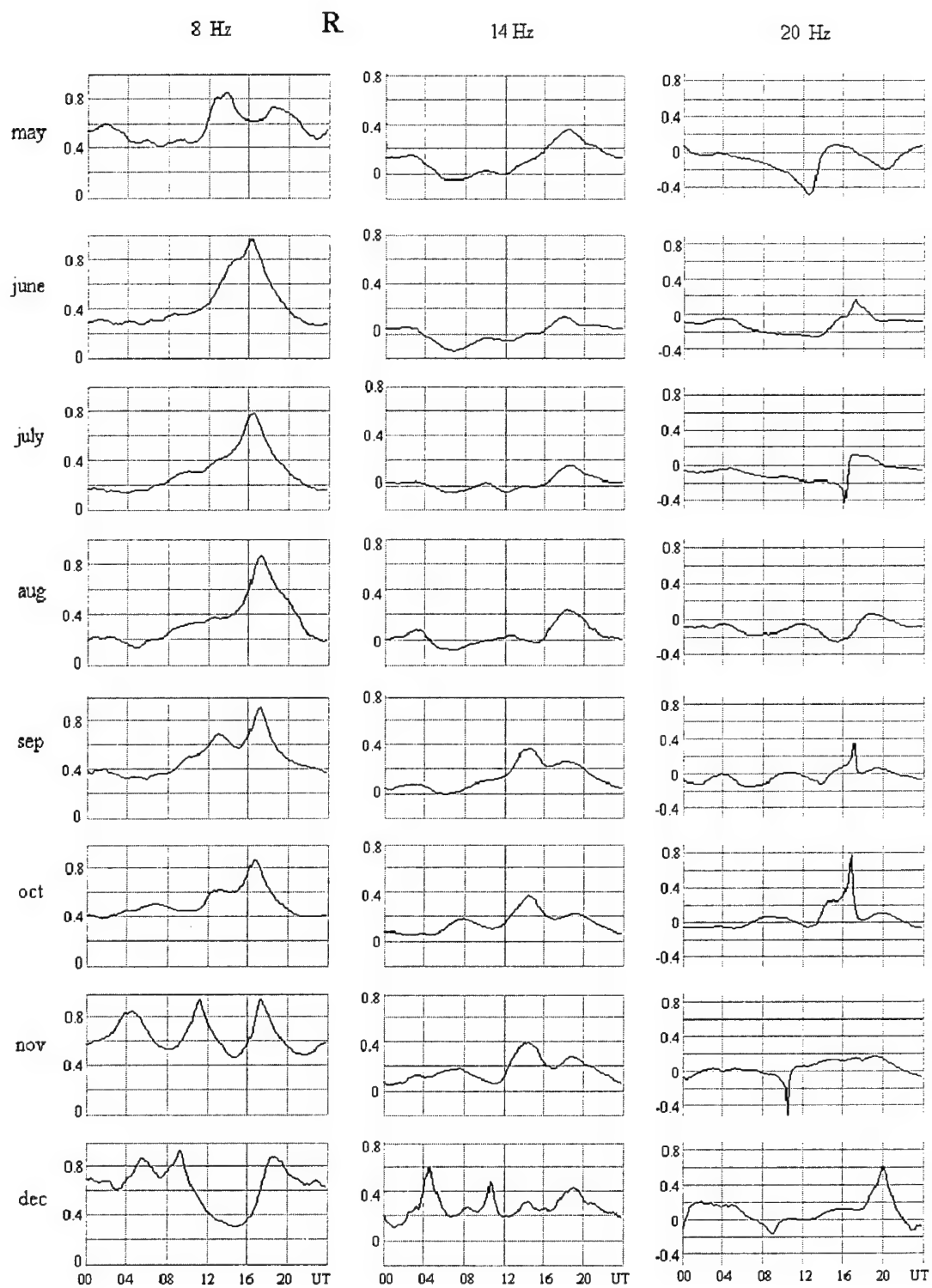


Fig.A 1.8 Month-averaged diurnal variations of the ellipticity ratio $r(t)$ for three Schumann resonance modes: May to December, 2001

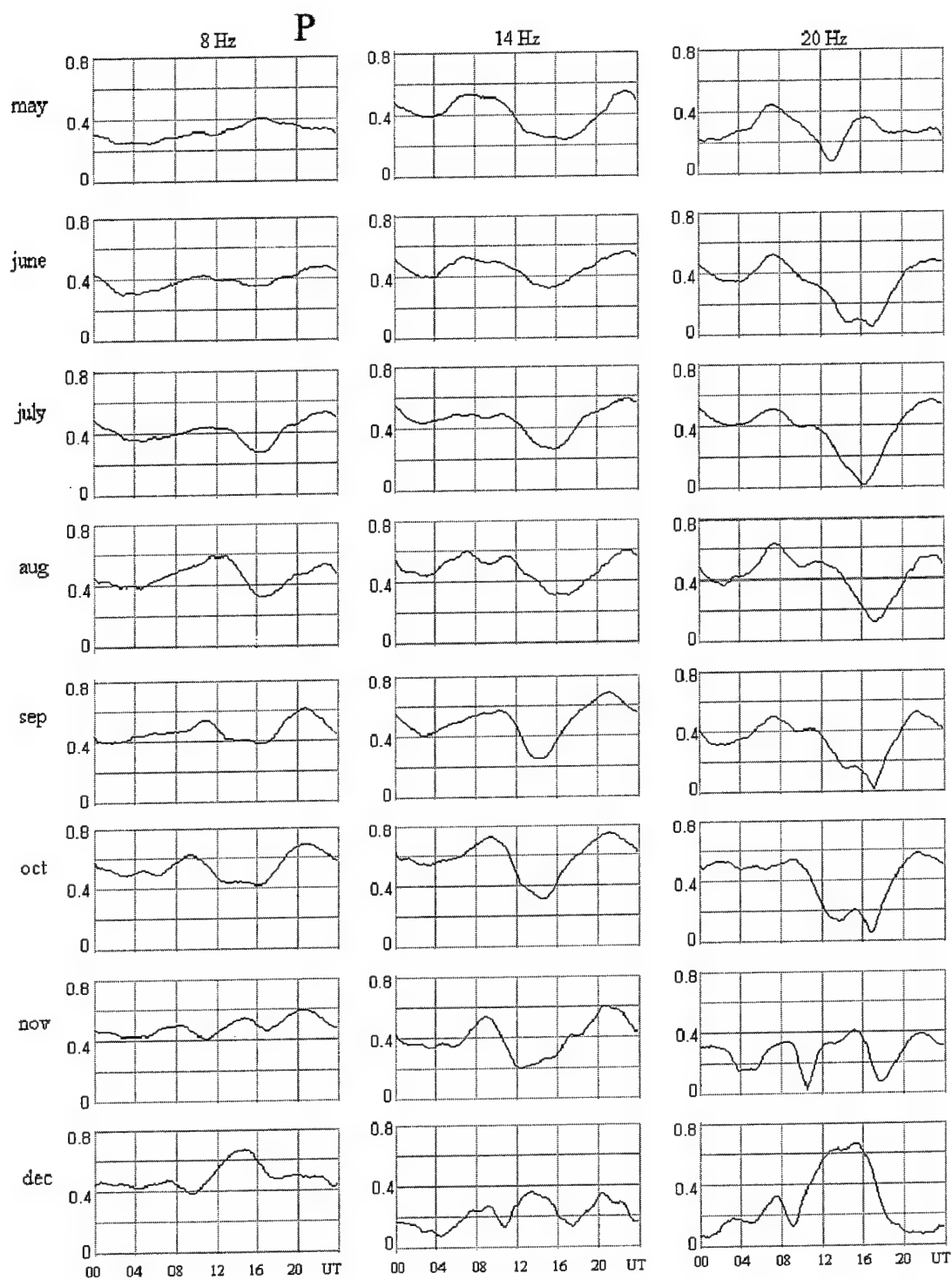


Fig. A 1.9 Month-averaged diurnal variations of the polarization, $P(t)$, for three Schumann resonance modes: March, 2002 to January, 2003

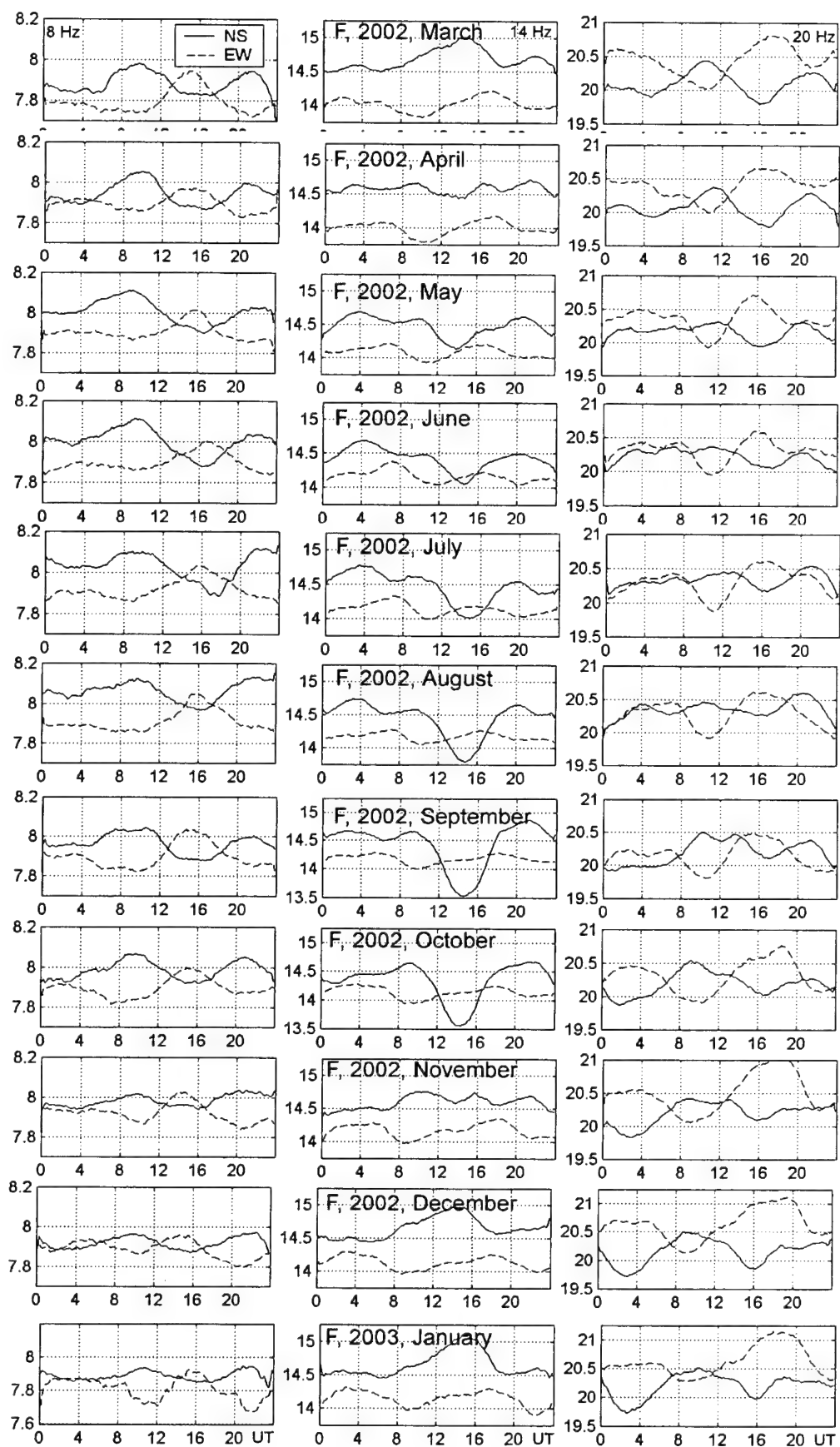


Fig.A 1.10 Month-averaged diurnal variations of the resonance frequency $F(t)$ for three Schumann resonance modes: March, 2002 to January, 2003

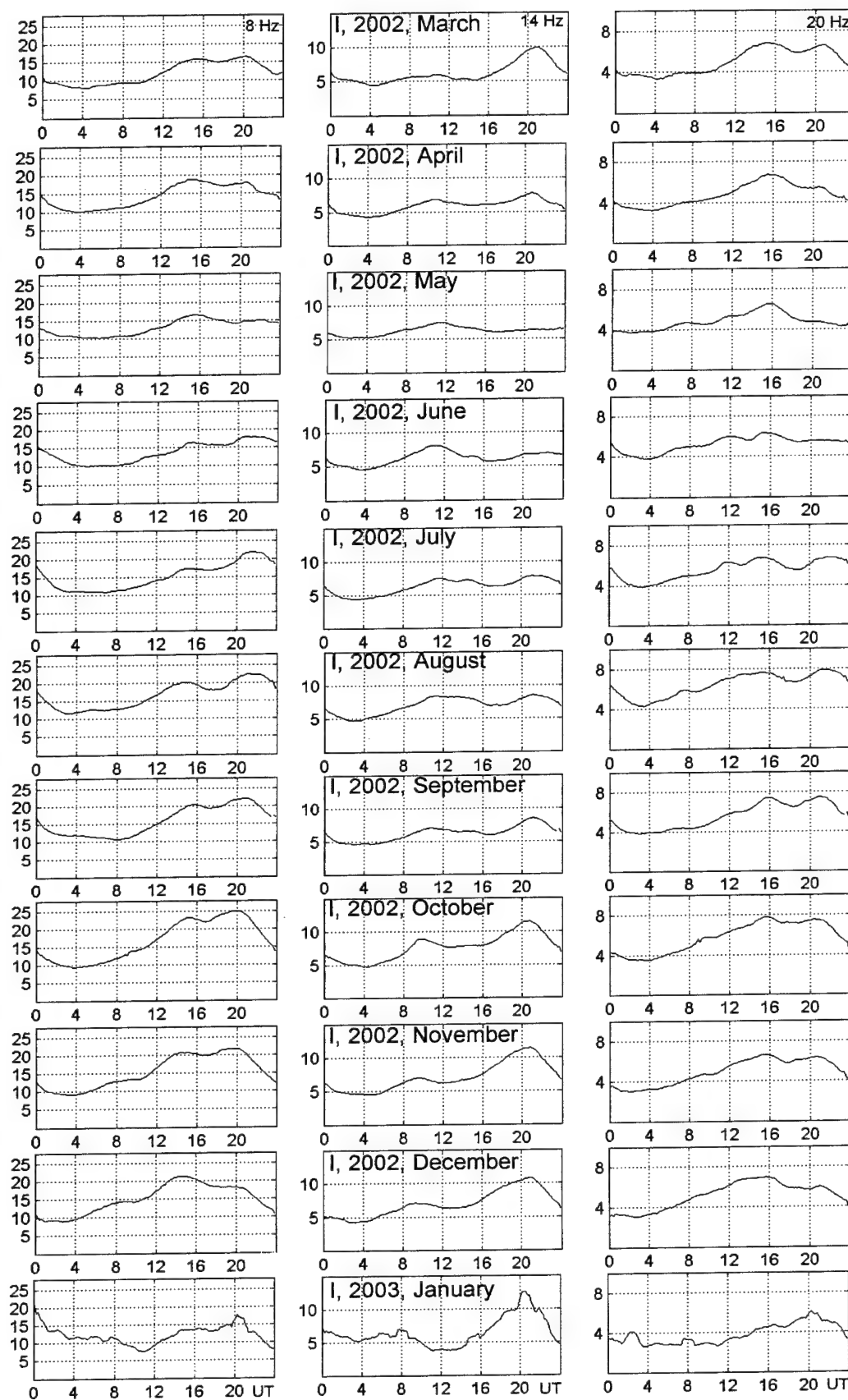


Fig.A 1.11 Month-averaged diurnal variations of intensity, $I(t)$ for three Schumann resonance modes (arbitrary units along the vertical axis): March, 2002 to January, 2003

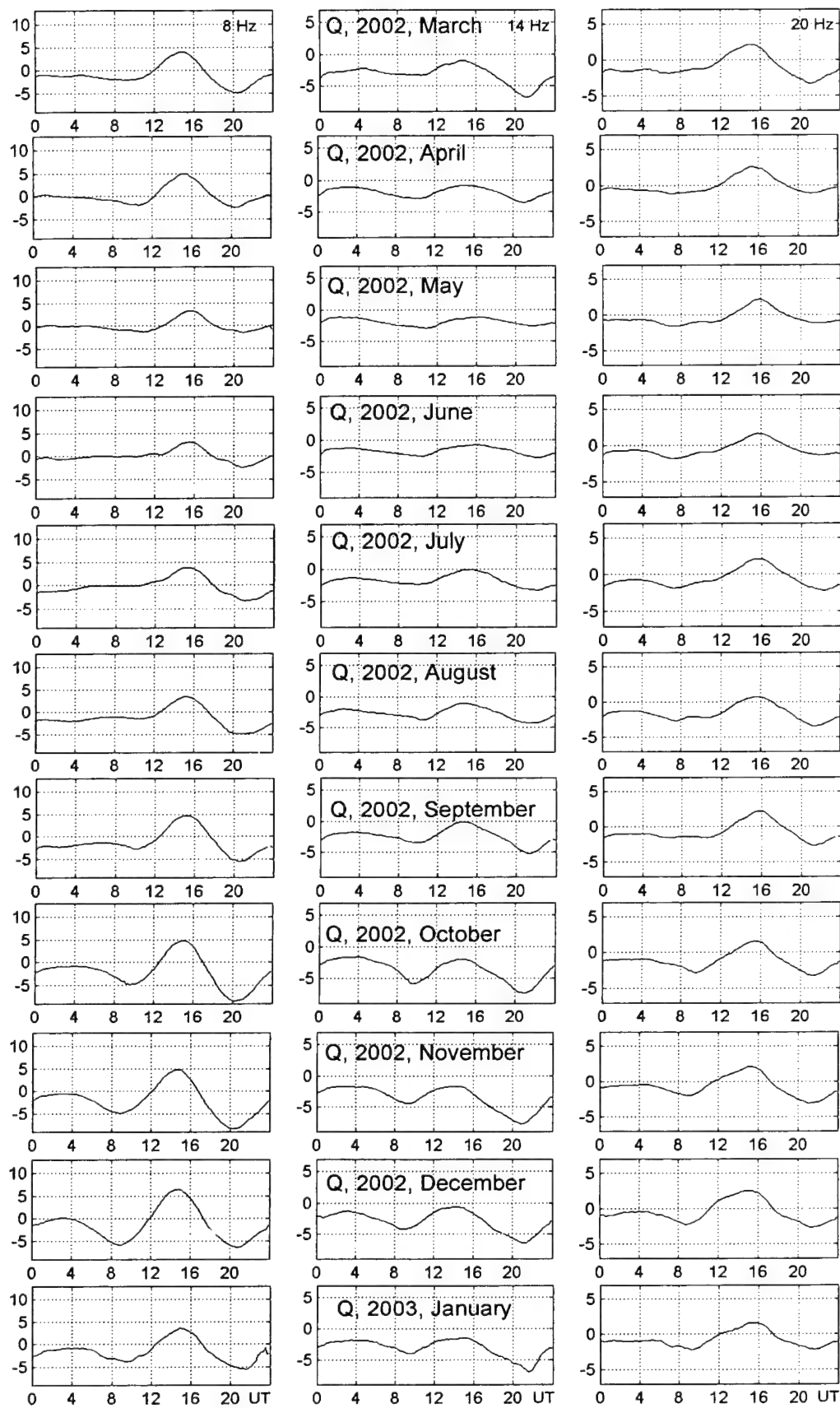


Fig.A 1.12 Month-averaged diurnal variations of the Stokes parameter $Q(t)$ for three Schumann resonance modes (arbitrary units along the vertical axis): March, 2002 to January, 2003

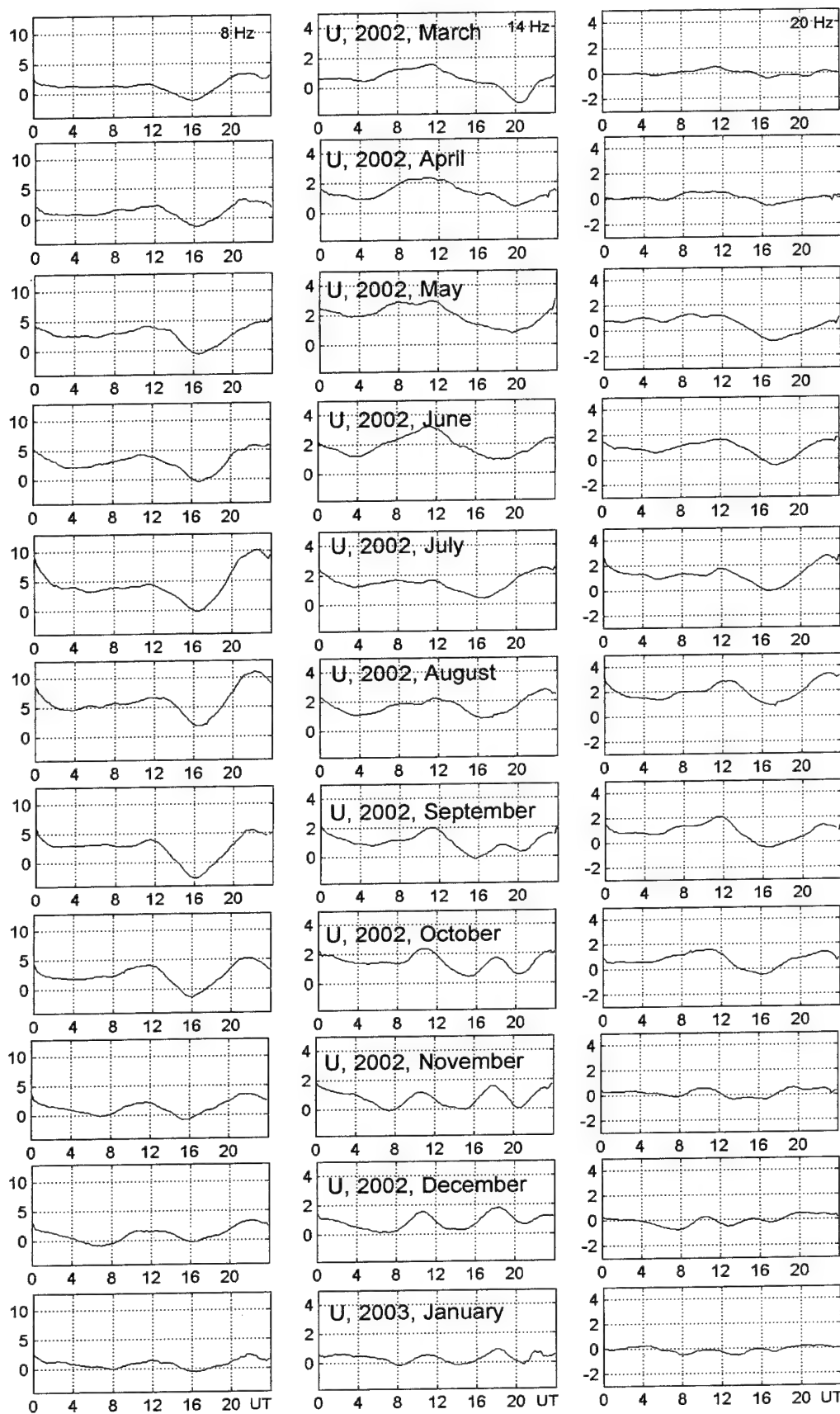


Fig.A 1.13 Month-averaged diurnal variations of the Stokes parameter $U(t)$ for three Schumann resonance modes (arbitrary units along the vertical axis): March, 2002 to January, 2003

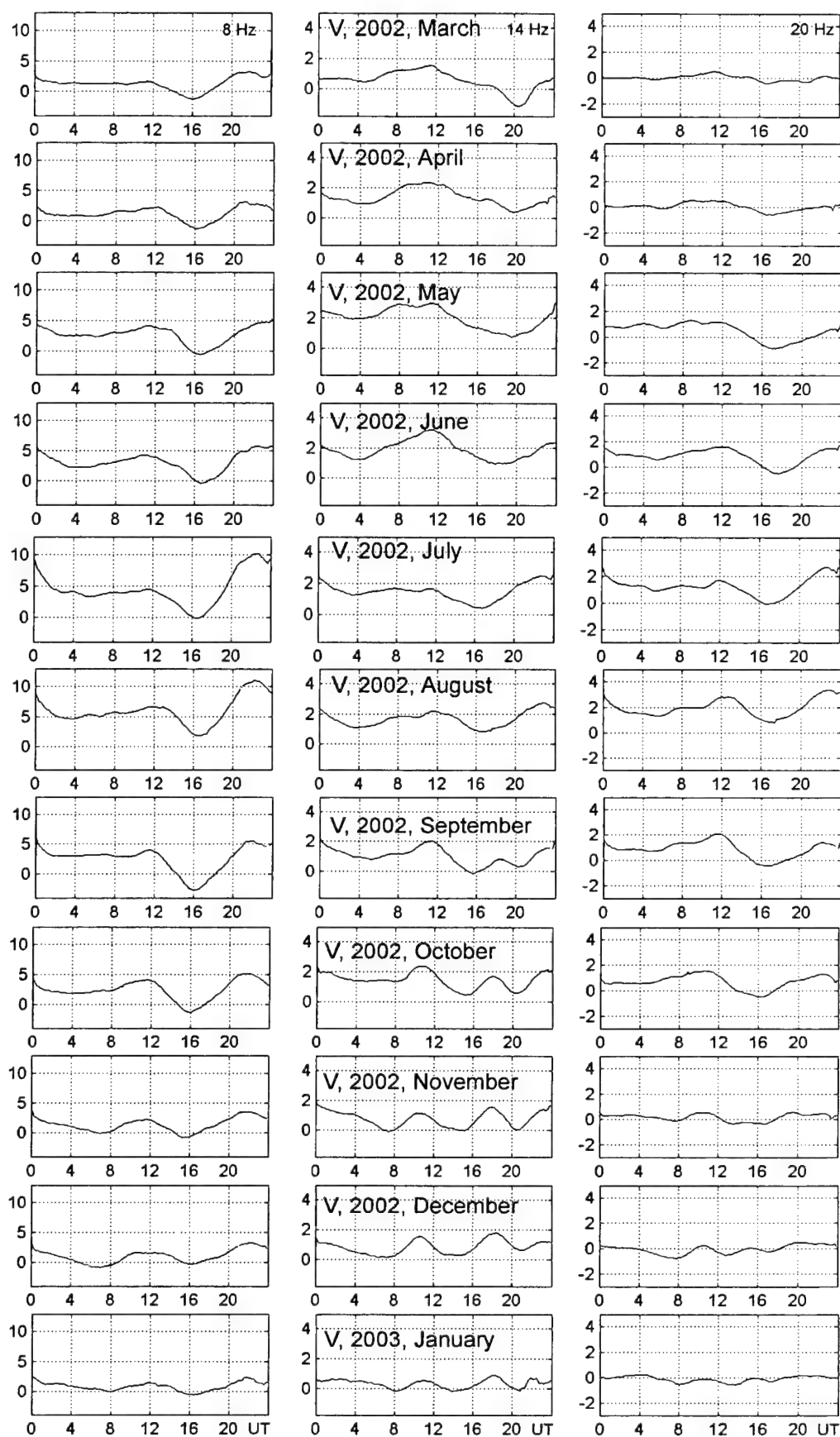


Fig.A 1.14 Month-averaged diurnal variations of the Stokes parameter $V(t)$ for three Schumann resonance modes (arbitrary units along the vertical axis): March, 2002 to January, 2003

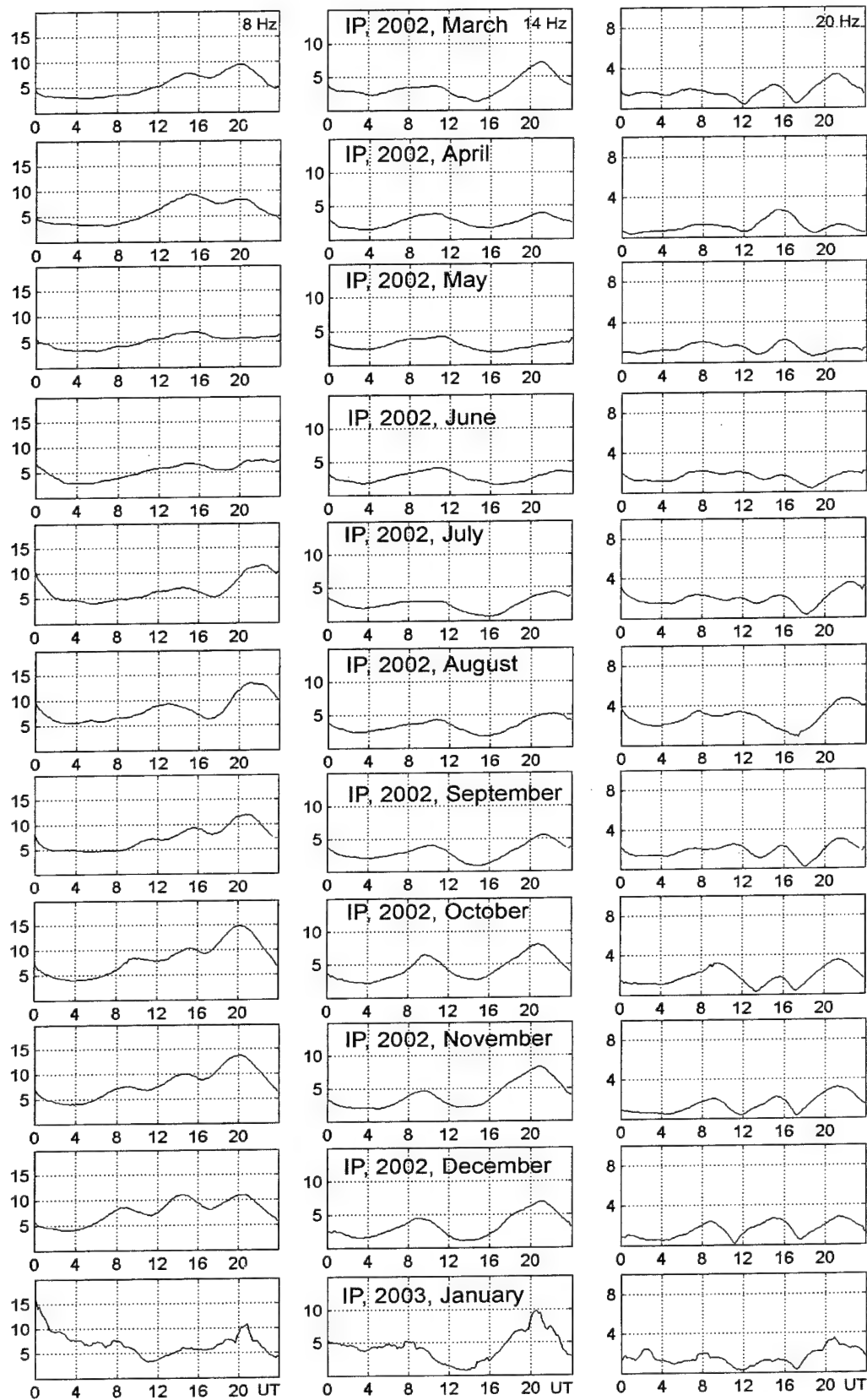


Fig.A 1.15 Month-averaged diurnal variations of polarized component's intensity $I_p(t)$ for three Schumann resonance modes (arbitrary units along the vertical axis): March, 2002 to January, 2003

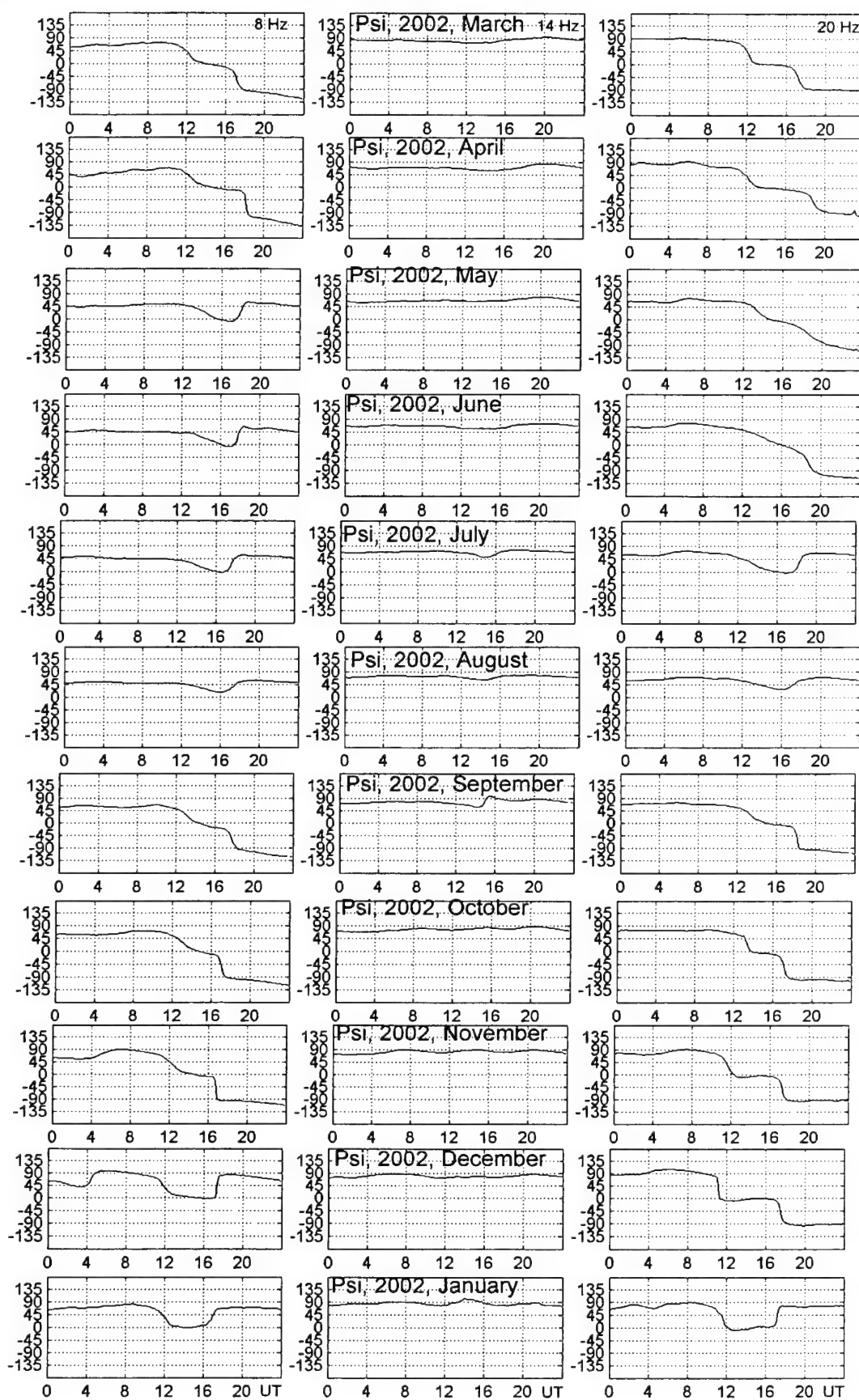


Fig.A 1.16 Month-averaged diurnal variations of the orientation angle $\Psi(t)$ of the polarization ellipse (degrees for three Schumann resonance modes): March, 2002 to January, 2003

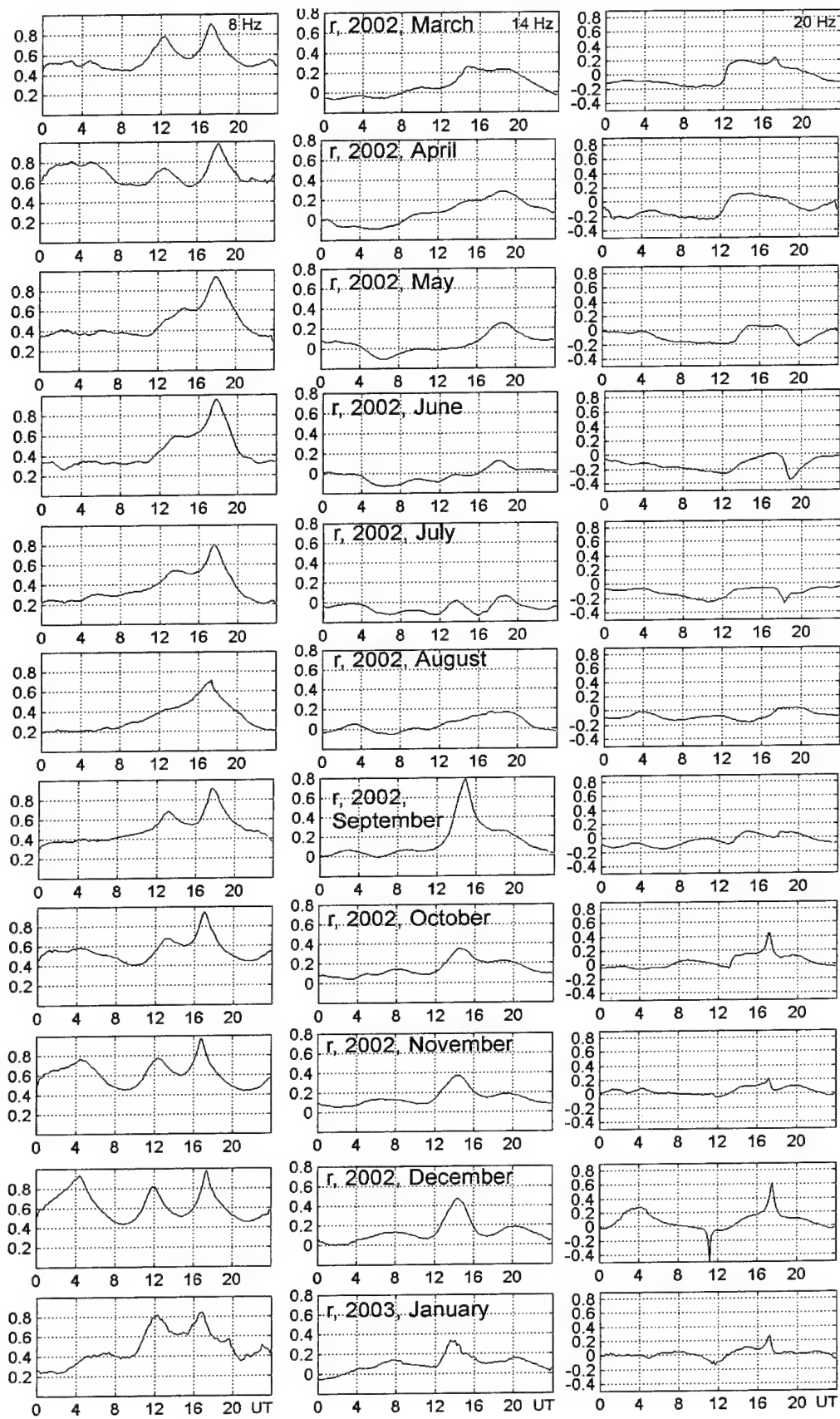


Fig.A 1.17 Month-averaged diurnal variations of the ellipticity ratio $r(t)$ for three Schumann resonance modes: March, 2002 to January,

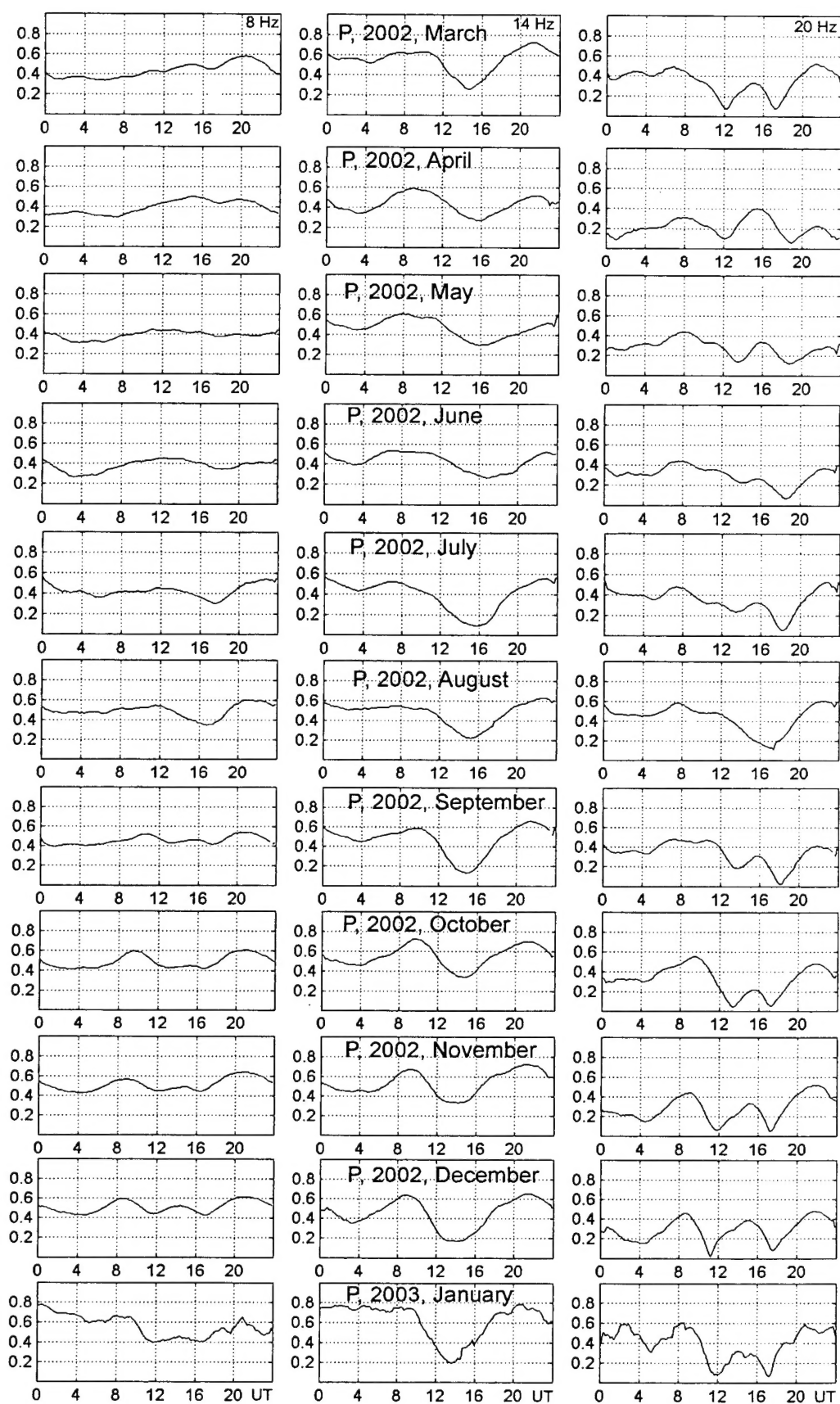


Fig.A 1.18 Month-averaged diurnal variations of the degree of polarization, $P(t)$, for three Schumann resonance modes): March, 2002 to January, 2003

REFERENCES

- Aleksin, V.F. and V.D. Khodusov, 1970; 1971; 1973: В.Ф. Алексин, В. Д. Ходусов. О кинетике магнитогидродинамических волн. I: Укр.физ. журнал, т.15 (1970), 1021-1028; II: Укр.физ.журнал, т.16 (1971), 603-608; III: Укр.физ.журнал, т. 18 (1973), 1707-1715.
- Bass, F.G. and I.M. Fuks, 1973: Wave scattering by the statistically rough surface, Pergamon Press.
- Beley, V.S. et al., 1991: В.С. Белей, В.Г. Галушко, И.М. Фукс, Ю.М. Ямпольский. Восстановление параметров ПИВ в модели идеально отражающей поверхности. Препринт №48, РИ АН УССР – Харьков.
- Bliokh, P.V., A.P. Nickolaenko, and Yu.F. Filippov, 1980: Schumann resonances in the Earth – ionosphere cavity – IEE Waves Series, vol.9. Peter Peregrinus, London.
- Born, M. and E. Wolf, 1967: Principles of optics. Pergamon Press: 4-th edition. Oxford.
- Briunelli, B.E. and A.A. Namgaladze, 1988: Б.Е. Брюнелли, А.А. Намгаладзе. Физика ионосферы. Москва, «Наука».
- Dungey, J.W. 1954: Electrodynamics of the outer atmosphere. Sci. Report 69, Penn. State Univ., University Park.
- Erdelyi, A. (Ed.), 1953: Higher transcendental functions, vol.1. McGraw – Hill Book Co.
- Evans, J.V., 1978: Incoherent scatter contribution to studies of the dynamics of the lower thermosphere. Reviews of Geophysics and Space Physics, vol. 16, pp.195-216
- Fatkullin, M.N. et al., 1981: М.Н. Фаткуллин., Т.И. Зеленова, В.К. Козлов, А.Д. Легенька, Т.Н. Соболева. Эмпирические модели среднеширотной ионосферы. Москва, «Наука».
- Francis, S.H., 1975: Global propagation of atmospheric gravity waves: a review. Journal of Atmospheric and Terrestrial Physics, vol. 37, pp. 1011-1054
- Galperin, Yu.I., and M. Hayakawa, 1996: On the magnetospheric effects of experimental ground explosions observed from AUREOL-3, J. Geomag. Geoelectr., 48, 1241-1263
- Galushko, V.G., 1984: В.Г. Галушко. Определение величины горизонтальных градиентов в ионосфере по измерениям параметров КВ сигнала в окрестностях мертвой зоны. Изв. ВУЗ – Радиофизика, т.27, 1491 – 1496
- Gelberg, M.G., 1987: М.Г. Гельберг. Образование мелкомасштабных неоднородностей внешней высокоширотной ионосферы альфвеновскими волнами. Изв. ВУЗ – Радиофизика, т. 30, 1301-1304
- Gershman, B.N., 1974: Б.Н. Гершман. Динамика ионосферной плазмы. Москва, «Наука».
- Gossard, E.E. and W.H. Hooke, 1975: Waves in the atmosphere. Elsevier, New York.

- Gurevich and Schwarzburg, 1973: А.В. Гуревич, Б.А. Шварцбург. Нелинейная теория распространения радиоволн в ионосфере. Москва, «Наука».
- Hines, C.O., 1968: Some consequences of gravity-wave critical layers in the upper atmosphere. *Journal of Atmospheric and Terrestrial Physics*, vol. 30, pp. 837
- Hines, C.O., 1960: Internal gravity waves at ionospheric heights. *Can. Journ. Phys.*, vol. 38, pp. 1441 - 1481
- Hocke, K. and K. Schlegel, 1996: A review of atmospheric gravity waves and travelling ionospheric disturbances: 1982-1995. *Ann. Geophysicae*, vol.14, pp. 917-940
- Hooke W.H., 1968: Ionospheric irregularities produced by internal atmospheric gravity waves. *Journal of Atmospheric and Terrestrial Physics*, vol. 30, pp.795-823
- Itonaga., M. and T.-I. Kitamura, 1993: Numerical simulations on ionospheric control of polarization of low-latitude geomagnetic pulsations. *Ann. Geophysicae*, vol.11, pp. 1018-1025
- Jankowski, J. and C. Sucksdorf, 1996: Guide for magnetic measurements and observatory practice. Warsaw.
- Kascheev, S.B. et al., 2000: С.Б. Кашеев, Ю.М. Ямпольский, А.В. Зализовский. Зондирование морской поверхности сигналами коротковолновых радиовещательных станций. *Радиофизика и радиоастрономия*, т.6, 79 -88.
- Lizunov, G., 2002: Alfvén wave structures generated in the magnetosphere by seismic wave. In: *Seismo Electromagnetics: Lithosphere-Atmosphere-Ionosphere Coupling*, Ed. by M. Hayakawa and O.A. Molchanov, TERRAPUB, Tokyo, 371-374
- Lyatsky, W.B. and Y.P. Maltsev, 1983: В.Б. Ляцкий, Ю.П. Мальцев. Магнитосферно – ионосферное взаимодействие. Москва, «Наука».
- Mikhailovski, A.V., 1976: А.В. Михайловский. Теория плазменных неустойчивостей. т.2, Москва, «Атомиздат».
- Monin, A.S. and V.P. Krasitsky, 1985: А.С. Монин, В.П. Красицкий. Явления на поверхности океана. Ленинград, Гидрометеиздат.
- Mul, P.M. and J.W. McGowan, 1979: Merged electron-ion beam experiments. III. Temperature dependence of dissociative recombination for atmospheric ions NO^+ , O_2^+ and N_2^+ . *J. Phys. B: Atom. and Mol. Phys.*, vol.12, 1591-1601
- Nickolaenko, A.P. et al., 2002: А.П. Николаенко, Л.М. Рабинович, А.В. Швец, А.Ю. Щекотов. Поляризационные характеристики низкочастотных резонансов. *Изв. ВУЗ – Радиофизика* (submitted).
- Orayevsky, V.N., 1984: В.Н. Ораевский. Параметрические неустойчивости магнитоактивной плазмы. В сб.: *Основы физики плазмы*, 2, Москва, „Энергоатомиздат”
- Parkinson, W.D., 1983: Introduction to geomagnetism. Scottish Academy Press, Edinburgh and London.
- Pilipenko, V.A., 1990: *Journ. Atm. Solar – Terrest. Phys.*, vol. 52, 1193 – 1209

- Pokhotelov, O. A., V.A. Pilipenko, E.N. Fedorov, L. Stenflo, and P.K. Shukla, 1994: Induced electromagnetic turbulence in the ionosphere and the magnetosphere, *Physica Scripta*, vol. 50, pp. 600-605
- Ponomarenko, P.V., Y.M. Yampolski, A.V. Zalizovski, D.L. Hysell, and O.F. Tyrnov, 2000: Interaction between artificial ionospheric irregularities and natural MHD waves. *J. Geophys. Res.*, vol.105, 171-181
- Project P-072, 2002: Annual Progress Report (Year 1). Institute of Radio Astronomy, Kharkov, Ukraine.
- Rice, C.J. and L.R. Sharp, 1977: Neutral atmospheric waves in the thermosphere and tropospheric weather systems, *Geophys. Res. Lett.*, vol.4, pp.315-318
- Rishbeth, H., and O.K. Garriot, 1969: Introduction to ionospheric physics. Academic Press, New York.
- Russel, C.T. and R.L. McPherron, 1973: Semiannual variations of geomagnetic activity. *J. Geophys. Res.*, vol.78, 92 -108
- Saka, O., T-J. Iijima and T. Kitamura, 1980: Ionospheric control of low latitude geomagnetic micropulsations. *Journal of Atmospheric and Terrestrial Physics*, vol. 42, pp. 517-520
- Sinitsin, V.G., M.C. Kelley, Yu.M. Yampolski, D.L. Hysell, A.V. Zalizovski, and P.V. Ponomarenko, 1999: Ionospheric conductivities according to Doppler radar observations of stimulated turbulence, *Journ. Atm. Solar-Terr. Phys.*, vol. 61, 903-912
- Sorokin, V.M. and G.V. Fedorovich, 1982: В.М. Сорокин, Г.В. Федорович. Физика медленных МГД-волн в ионосферной плазме. Москва, «Энергоатомиздат».
- Sutcliffe, P.R. and A.W.V. Poole, 1989: Ionospheric Doppler and electron velocities in the presence of ULF waves. *J. Geophys. Res.*, vol. 94, 13505 - 13514
- Trakhtengertz, V.Y. and A.J. Feldstein, 1982: В.Ю. Трахтенгерц, А.Я. Фельдштейн. В кн.: Межпланетная среда и магнитосфера Земли. Москва, «Наука».
- Williams, P.J.S., 1996: Tides, atmospheric gravity waves and travelling disturbances in the ionosphere. In: *Modern ionospheric science. A collection of articles published on the occasion of the anniversary: "50 years of ionospheric research in Lindau"*, URSI, pp. 136-180
- WMO, 1956: World distribution of thunderstorm days, Part 2: Tables of marine data and world maps. OMM-No 21, T.P.21.
- Yampolski, Y.M., 1989: Ю.М. Ямпольский. "Эхо-рассеяние" КВ сигналов на искусственной ионосферной турбулентности. *Изв. ВУЗ - Радиофизика*, т. 32, 519-521
- Zalizovski, A.V. et al., 2000: А.В. Зализовский, Ю.М. Ямпольский, В.Е. Корепанов, И.Ф. Доценко. *Радиофизика и радиоастрономия*. Том. 5, №2, 2000, с. 118-124
- Zalizovski, A.V. et al., 2001: А.В. Зализовский, В.Г. Синицын, Ю.М. Ямпольский. Поляризация геомагнитных пульсаций Pc3/Pc4 в Северном и Южном полушариях: экспериментальные данные и численное моделирование. *Радиофизика и радиоастрономия*, т.6, 302-309.